

# Theoretical Performance Analysis of a Novel Hemispherical Tissue Equivalent Proportional Counter for Neutron Monitoring and Dosimetry

By

David Broughton

A Thesis Submitted in Partial Fulfillment of the Requirements for the Degree of  
Master of Applied Science in Nuclear Engineering

Faculty of Energy Systems and Nuclear Science Program  
University of Ontario Institute of Technology

February 2016

©David Broughton 2016

## Abstract

Neutron dosimetry in reactor fields is currently conducted using thermal neutron flux monitors. It has been demonstrated that Tissue Equivalent Proportional Counters (TEPCs) have the potential to improve the accuracy of neutron dosimetry in these reactor fields, and Multi-Element Tissue Equivalent Proportional Counters (METEPCs) could reduce the size of instrumentation required to do so. The current METEPC designs are prohibitively complex and are sensitive to motion and audible noise. This work proposes a novel hemispherical element with a wire-less anode ball as a solution. The hemispherical METEPC element was analyzed as a single TEPC to first demonstrate the potential of this new design. Its performance was evaluated relative to current cylindrical and spherical counter designs that have been demonstrated experimentally to perform very well. The performance analysis first used equipotential distributions generated with ANSYS Maxwell (V. 14.0) in order to solve the Townsend equation and calculate radial gas gain distributions for each counter. Through this it was found that the hemispherical counter exhibits completely uniform gas gain for electrons approaching the anode from all directions and its avalanche region occupies only 0.0004% of the entire gas cavity volume, whereas in the cylindrical and spherical counters the avalanche occupies 0.6% and 0.12% of the total gas cavity volume, respectively. Energy deposition simulations were conducted using the Monte Carlo code PHITS (V. 2.24) with both mono-energetic 2.5 MeV neutrons and the neutron spectrum of  $^{252}\text{Cf-D}_2\text{O}$  moderated. In these neutron fields the hemispherical counter appears to be a good alternative to the reference spherical geometry, whereas the cylindrical counter tends to under-respond to  $H^*(10)$  for the lower neutron energies of the  $^{252}\text{Cf-D}_2\text{O}$  moderated field. These theoretical results are promising, and if the recommended follow-up experimental work demonstrates the hemispherical counter works as anticipated it will be ready to be incorporated into an METEPC design.

## Acknowledgements

This work was made possible through the generous financial support of the University Network of Excellence in Nuclear Engineering (UNENE). Beyond this it would not have been possible without the support and encouragement of several individuals who helped to introduce me to microdosimetry and the tools used for detector analysis.

I would like to thank my thesis supervisor Dr. Anthony Waker for his patience, guidance and encouragement throughout this work, it is very much appreciated. He shared his knowledge during discussions and as a professor sparking my curiosity in microdosimetry. I would also like to thank Dr. Gloria Orchard for assistance throughout this work, especially when starting to use the Maxwell software and conducting the error analysis, and to Dr. Fawaz Ali for providing an overview of PHITS, both of you really helped accelerate the learning process. Outside of the studies, the support from friends and family throughout these years has always been appreciated.

# Table of Contents

<i>Abstract</i> .....	ii
<i>Acknowledgements</i> .....	iii
<i>List of Figures</i> .....	vii
<i>List of Tables</i> .....	x
<i>List of Appendices</i> .....	xi
<i>List of Acronyms</i> .....	xii
<b>Chapter 1: Introduction</b> .....	<b>1</b>
1.1 Introduction to Neutron Monitoring.....	1
1.2 An Overview of Dosimetric Quantities.....	2
1.3 Current Practices and Issues in Neutron Dosimetry .....	6
1.4 TEPCs as an Alternative to Moderator Based Counters .....	8
1.5 Research Objectives .....	11
1.6 Thesis Outline .....	13
<b>Chapter 2: Experimental Microdosimetry</b> .....	<b>14</b>
2.1 Introduction.....	14
2.2 Experimental Microdosimetry Concepts .....	15
2.2.1 Basics of Tissue Equivalent Proportional Counters.....	15
2.3 Particle Interactions with Tissue.....	21
2.3.1 Neutron Interactions.....	21
2.3.2 Charged Particle Interactions.....	26
2.3.3 Photon Interactions.....	29
2.4 Microdosimetric Quantities and Distributions.....	31
2.4.1 Lineal Energy .....	31
2.4.2 Microdosimetric Distributions.....	33
2.4.3 Moments of the Microdosimetric Distributions.....	38
2.5 Determining Operational Quantities.....	38
2.6 Error in Microdosimetric and Operational Quantities .....	41

<b>Chapter 3: Detectors in Microdosimetry .....</b>	<b>48</b>
3.1 Introduction.....	48
3.2 Variations of TEPCs .....	48
3.2.1 Rossi Counters and Single Wire TEPCs .....	48
3.2.2 Cylindrical TEPCs.....	50
3.2.3 METEPCs .....	52
3.4 Design Concept for a Wire-less TEPC .....	55
3.4.1 Potential Improvements of TEPC and METEPC Element Designs.....	55
3.4.2 Initial Study of Electric Field Distributions.....	55
3.4.3 Optimization of the Hemisphere Design .....	57
3.5 Geometric Sources of Variance .....	66
<b>Chapter 4: Characterizing Gas Gain.....</b>	<b>70</b>
4.1 Introduction.....	70
4.1.1 ANSYS Maxwell .....	70
4.2 General Gas Multiplication Theory .....	72
4.2.1 Gas Gain in Cylindrical Counters.....	73
4.2.2 Gas Gain in Spherical Counters.....	75
4.2.3 Gas Gain in Hemispherical Counters.....	76
4.3 Results and Discussion.....	78
4.3.1 Cylindrical Counter.....	78
4.3.2 Spherical Counter.....	82
4.3.3 Hemispherical Counter.....	86
4.3.4 Comparing Gas Gain in Different Counters.....	88
<b>Chapter 5: Simulating Microdosimetric Experiments .....</b>	<b>91</b>
5.1 Introduction.....	91
5.1.1 Simulated Experimental Setup .....	93
5.1.2 Analyzed Distributions and Quantities.....	95
5.2 Results and Discussion.....	97
5.2.1 Comparing Microdosimetric Dose Distributions .....	97

5.2.2 Overall Energy Deposition Patterns and Instrument Response .....	101
<b>Chapter 6: Conclusion and Recommendations for Further Work.....</b>	<b>111</b>
Appendix I: Determining Gas Constants for Gas Gain Calculations .....	115
Appendix II: PHITS Input Files .....	117
Appendix III: MATLAB Data Analysis.....	123
Appendix IV: Results of Monte Carlo Energy Deposition Simulations in the Proposed Design for Manufacturing of a Prototype Hemispherical Counter .....	129
References.....	131

## List of Figures

Figure 1.1	Measured neutron fluence rate spectra inside containment at Point Lepreau Generating Station (adapted from [4]) .....	2
Figure 1.2	Illustration of the ICRU 51 [9] described $H^*(10)$ measurement conditions.....	5
Figure 1.3	Flux to Dose Equivalent conversion factors (based on US NRC data [15]).....	7
Figure 1.4	Response functions of two typical-sized moderator-based survey instruments and a TEPC; neutron energies 0.5 eV and 10 keV are indicated to aid further discussion given below (adapted from [1]) .....	9
Figure 1.5	Mean fraction of total fluence and ambient dose equivalent over all measurement locations in Figure 1.1 (adapted from [4]) .....	10
Figure 2.1	Abundance weighted elastic scattering cross sections for H, O, C and N between 0 MeV and 14 MeV [30] .....	24
Figure 2.2	Classification of charged particle tracks within a proportional counter [32] .....	26
Figure 2.3	Stopping power as a function of neutron energy for carbon ion in TE A-150 (data from [37]) .....	28
Figure 2.4	Relative importance of the three major interactions of photons with matter; $z \sim 7$ is indicated to represent tissue (adapted from [41]) .....	30
Figure 2.5	Division of decades into equal sized logarithmic intervals (adapted from [45]) .	33
Figure 2.6	Frequency and dose distributions simulated in PHITS for 2 $\mu\text{m}$ diameter simulated site using $2 \times 10^9$ neutrons.....	37
Figure 2.7	Quality factor as a function of lineal energy, based on ICRP 60 [5] .....	40
Figure 3.1	Schematic of Rossi and Single wire counters, with conductive materials shown in black and insulating materials shown in grey (not to scale) .....	49
Figure 3.2	Far West model LET-SW5, 12.7 cm diameter (adapted from [50]).....	50
Figure 3.3	Illustration of the 0.02 cm diameter by 0.05 cm length anode extension as used in the 0.5 cm by 5 cm cylindrical METEPC element described in [53, 54] .....	51
Figure 3.4	Illustration of the original 296 element METEPC prototype [55] .....	52
Figure 3.5	Illustration of TEPC Instruments, From Left to Right: Standard 12.7 TEPC Design, METEPC, CMETEPC, and QITEPC [51] .....	54

Figure 3.6	2D Electric field equipotential distributions in +ZX plane (a) 0.635 cm by 0.635 cm Right Cylinder with a 0.2 mm diameter anode at 700 V; (b) 12.7 cm diameter sphere with concentric 2 mm diameter ball anode suspended from 70 μm diameter anode at 700 V.....	56
Figure 3.7	Reduced electric field as a function of insulator ring radius.....	58
Figure 3.8	Electric field distributions within 1.27 cm diameter hemisphere using various insulator radii: (a) 6.55 mm (b) 4.9 mm (c) 4.2 mm (d) 3.2 mm (e) 2.2 mm (f) 1.2 mm.....	59
Figure 3.9	Electric field distributions within 2.54 cm diameter hemisphere using various insulator radii: (a) 12.9 mm (b) 9.6 mm (c) 8.2 mm (d) 6.2 mm (e) 4.2 mm (f) 2.2 mm.....	60
Figure 3.10	Illustration of 2.54 cm diameter hemisphere with 0.4 mm diameter anode (red) and 2.2 mm radius insulator (blue).....	61
Figure 3.11	Illustration of proposed hemispherical counter prototype design: (a) 2.13 mm thick A-150 hemisphere walls with 5 mm extension at bottom; (b) 5 mm thick A-150 hemisphere base with three tap holes; (c) insulator with 3 tapped holes which align with those of the hemispheres base and 3 tapped holes to fix the base of the insulator in place; (d) top view of insulator tapped holes.....	66
Figure 3.12	Diagram of the chain of random factors which determine energy deposition in a site [56] .....	67
Figure 4.1	Equipotential lines in 5 cm x 0.5 cm cylindrical counter ranging from 700 V to 50 V, with the 6 labelled lines showing where radial patterns in gas gain were analyzed .....	79
Figure 4.2	Absolute gain as a function of radial distance within the cylindrical counter, Z represents the distance from the center of the anode wire as shown in Figure 4.1 .....	80
Figure 4.3	Experimentally measured gas gain variation along the length of the anode wire [53].....	81
Figure 4.4	Equipotential lines in the 12.7 cm spherical counter ranging from 700 V to 50 V, with the 11 labelled lines showing where radial patterns of gas gain were analyzed .....	83
Figure 4.5	Absolute gain as a function of radial distance within the spherical counter, Z represents the distance from the center of the anode wire as shown in Figure 4.4 .....	84

Figure 4.6	Maximum gas gain along the anode wire relative to the center of the anode wire .....	84
Figure 4.7	Equipotential lines in the 2.54 cm hemispherical counter ranging from 700 V to 50 V, with the labelled lines highlighting the 6 angles of approach where radial patterns of gas gain were analyzed (90°, 67.5°, 45°, 22.5°, 11.25° and 5.625°) ..	86
Figure 4.8	Absolute gain as a function of radial distance within the hemispherical counter, angle represents the angle of approaching electrons as shown in Figure 4.7 ....	87
Figure 4.9	Variation in gas gain along the anode wires of the spherical and cylindrical counters, relative to the gain at the center of the wire .....	89
Figure 5.1	Neutron energy spectrum for a heavy water moderated Californium-252 source, mean neutron energy 0.54 MeV (data from ISO 2000 [16]) .....	91
Figure 5.2	Illustrations of the six source-detector geometries employed for the Monte Carlo simulations in PHITS.....	94
Figure 5.3	Comparison of dose distributions for 2.5 MeV neutron field (representative of D-D neutron generator) simulated in PHITS with $2 \times 10^9$ incident neutrons for: (a) Cylindrical and Spherical TEPCs; (b) Hemispherical and Spherical TEPCs.....	98
Figure 5.4	Comparison of dose distributions for $^{252}\text{Cf}$ -D <sub>2</sub> O moderated neutron field simulated in PHITS with $2 \times 10^9$ incident neutrons for: (a) Cylindrical and Spherical TEPCs; (b) Hemispherical and Spherical TEPCs.....	100
Figure 5.5	Simulated Q Response values relative to the ICRP 60 [5] Q*(10) values of 12.27 and 9.62 for 2.5 MeV and heavy water moderated Californium neutron fields, respectively.....	103
Figure 5.6	Simulated Dose Response values relative to the ICRP 60/74 [5, 10] D*(10) values of $3.39 \times 10^{-11} \text{ Gy} * \text{cm}^2/\text{n}$ and $1.12 \times 10^{-11} \text{ Gy} * \text{cm}^2/\text{n}$ for 2.5 MeV and heavy water moderated Californium neutron fields, respectively .....	104
Figure 5.7	Simulated H*(10) Response values relative to the ICRP 74 [10] H*(10) values of $4.16 \times 10^{-10} \text{ Sv} * \text{cm}^2/\text{n}$ and $1.08 \times 10^{-10} \text{ Sv} * \text{cm}^2/\text{n}$ for 2.5 MeV and heavy water moderated Californium neutron fields, respectively.....	105

## List of Tables

Table 2.1	Composition of tissue equivalent materials by element weight percent [ 27, 29] .....	19
Table 2.2	Molar properties of gases used for propane based TE gas .....	21
Table 2.3	Maximum stopping power and ranges for recoil nuclei in unit density A-150 for 2.5 MeV neutrons (data from [37]).....	36
Table 3.1	Analysis of the effects of insulator radius and counter size on the magnitude of electric and reduced electric fields .....	58
Table 3.2	Parameters of detectors used throughout analysis .....	63
Table 3.3	Mean chord lengths along with respective relative variances for simulation of a 2 $\mu\text{m}$ diameter site (*for the hemisphere the radius is defined as 2 $\mu\text{m}$ to better resemble the other detectors, **the relative variance of a cylinder is dependent upon its elongation, this is for the simulated cylinder where <i>height</i> = 10x <i>diameter</i> ).....	68
Table 3.4	Chord length distributions within spherical, cylindrical and hemispherical counter geometries.....	68
Table 4.1	Summary of the quantities measuring uniformity of gas gain.....	89
Table 5.1	Definitions for terms used throughout results and discussion of PHITS simulations .....	95
Table 5.2	Microdosimetric moments and operational response values from Monte Carlo microdosimetric simulations conducted with PHITS using 2.5 MeV neutrons ..	107
Table 5.3	Microdosimetric moments and operational response values from Monte Carlo microdosimetric simulations conducted with PHITS using $^{252}\text{Cf-D}_2\text{O}$ moderated neutron fields.....	108
Table 5.4	Ranked overall mean detector response values with percent over (+) and under (-) response.....	109
Table A.1	Results of Monte Carlo simulations in PHITS using 2.5 MeV neutron fields for hemispherical counters with (a) uniform 2.13 $\text{mm}$ thick walls; and (b) 2.13 $\text{mm}$ thick hemisphere with a 5 $\text{mm}$ thick cylindrical base .....	129
Table A.2	Results of Monte Carlo simulations in PHITS using $^{252}\text{Cf-D}_2\text{O}$ moderated neutron fields for hemispherical counters with (a) uniform 2.13 $\text{mm}$ thick walls; and (b) 2.13 $\text{mm}$ thick hemisphere with a 5 $\text{mm}$ thick cylindrical base.....	130

## List of Appendices

Appendix I	Determining Gas Constants for Gas Gain Calculations .....	115
Appendix II	PHITS Input Files.....	117
Appendix III	MATLAB Data Analysis .....	123
Appendix IV	Results of Monte Carlo Energy Deposition Simulations in the Proposed Design for Manufacturing of a Prototype Hemispherical Counter .....	129

## List of Acronyms

CANDU	CANadian Deuterium Uranium
CNL	Canadian National Laboratories
CPE	Charged Particle Equilibrium
CMETEPC	Compact Multi Element Tissue Equivalent Proportional Counter
GM	Geiger-Muller
ICRP	International Commission on Radiological Protection
ICRU	International Commission on Radiation Units and Measurements
ISO	International Organization for Standardization
LET	Linear Energy Transfer
MATLAB	MATrix LABoratory
MCNPX	Monte Carlo N-Particle eXtended
METEPC	Multi Element Tissue Equivalent Proportional Counter
PHITS	Particle and Heavy Ion Transport Code System
PHWR	Pressurized Heavy Water Reactor
QITEPC	Quarter Inch-based Tissue Equivalent Proportional Counter System
RBE	Relative Biological Effectiveness
TDRA	Theory of Dual Radiation Action
TE	Tissue Equivalent
TEPC	Tissue Equivalent Proportional Counter

## Chapter 1: Introduction

### 1.1 Introduction to Neutron Monitoring

Neutrons are an inevitable component of the radiation fields encountered in nuclear power plants. While under normal circumstances worker exposures to neutron radiation are minimal, nevertheless occasional repairs and work are required in areas within the reactor building where neutron fields exist and thus neutron monitoring is necessary. As dosimetry records must include all radiation exposures, the ability to conduct accurate dosimetry in neutron fields is important. There is reason to believe that the current portable neutron monitors based on thermal neutron counting do not adequately fulfill this purpose [1]. This is demonstrated by the accepted uncertainty of dose measurements in neutron fields being 50%, whereas photon and beta exposures are expected to be within 30% [2]. It has been recognized that Tissue Equivalent Proportional Counters (TEPCs) have the potential to increase the accuracy of neutron dosimetry in reactor fields [3].

One of the challenges of neutron monitoring and dosimetry is that the neutron fields encountered vary significantly, and cover energies over some nine orders of magnitude. Within the reactor building the primary source of fast neutrons is leakage from the reactor vessel. This produces the largest fluence of high energy neutrons near the vessel, with the spectra tending to shift to lower energies and fluence as distance increases from the vessel. At a given location the local neutron spectrum is also highly dependent on how neutrons scatter off of the immediate surroundings. In Figure 1.1 the neutron fluence rate spectra measured at 6 locations within containment of a CANDU® 600 Pressurized Heavy Water Reactor (PHWR) Power Plant are presented [4]. These measurements demonstrate the wide variation in both fluence rates and neutron energy distributions.

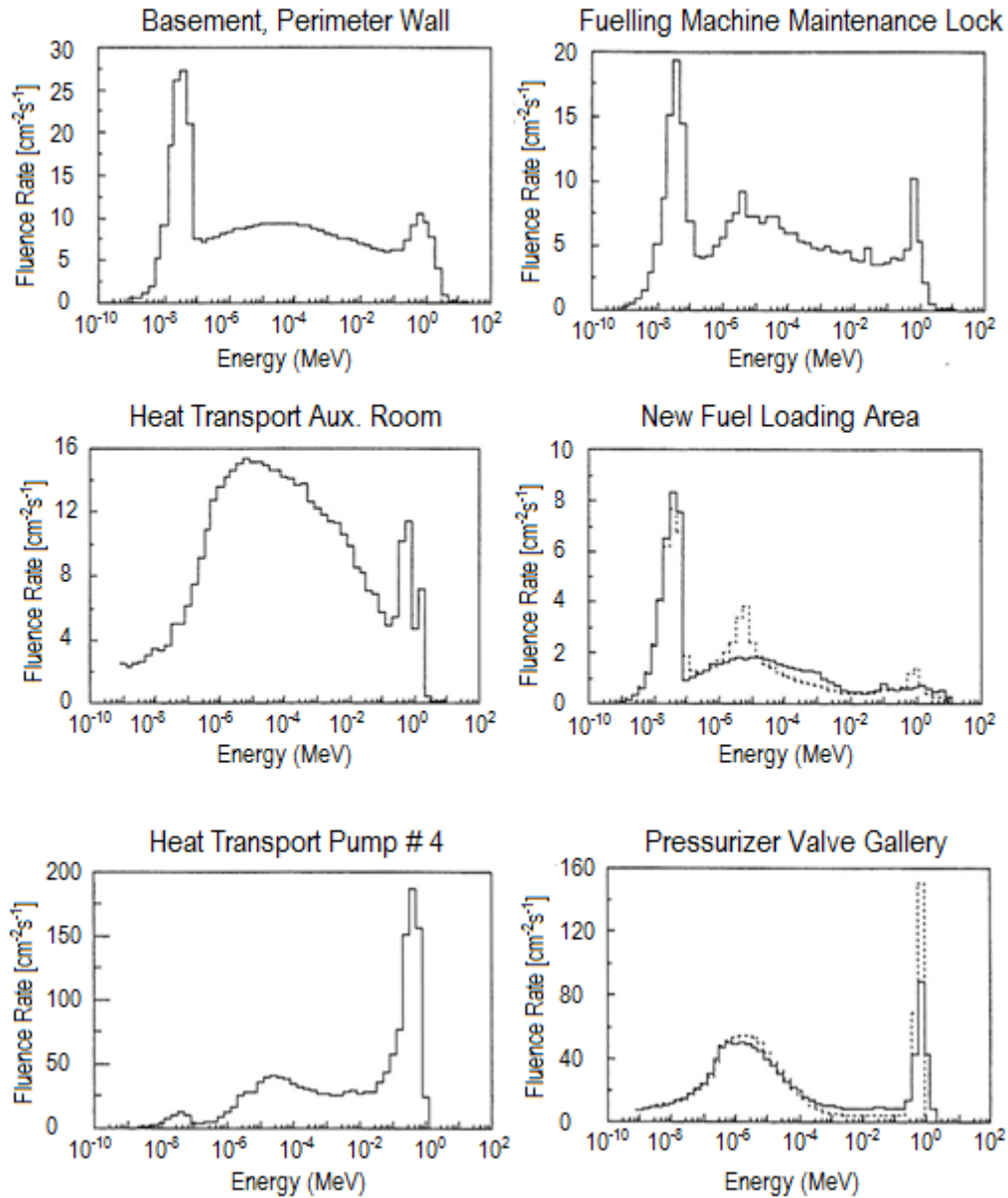


Figure 1.1 – Measured neutron fluence rate spectra inside containment at Point Lepreau Generating Station (adapted from [4])

## 1.2 An Overview of Dosimetric Quantities

The wide variation of neutron fields causes a number of issues with instrumentation for portable neutron monitoring and dosimetry. Before this can be addressed the framework of dosimetric quantities will be reviewed to establish measurement requirements. The most basic

measurable quantity is the *absorbed dose*,  $D$  [ $J/kg = Gy$ ]. This represents the mean energy deposited,  $d\bar{\epsilon}$ , to the unit mass,  $dm$ :

$$D = \frac{d\bar{\epsilon}}{dm} \quad (1.1)$$

The absorbed dose however is not a sufficient quantification of the exposure in neutron fields as the relative stochastic risks from neutron exposures are more complex than simply the total energy deposition. Malignancies and heritable effects depend on both the dose and the ionization density. As the dose limits in radiation protection serve to limit these stochastic risks additional quantities are also used.

The *dose equivalent*,  $H$  [ $Sv$ ], quantifies dose in terms of the relative stochastic risk. This is defined as the product of the absorbed dose and the unit-less quality factor,  $Q(L)$ :

$$H = D * Q(L) \quad (1.2)$$

As the quality factor is a function of Linear Energy Transfer (LET),  $L$  [ $keV/um$ ], which is essentially the stopping power [5], it is able to account for varying degrees of biological damage from variations in ionization density. However, since the dose equivalent characterizes effects at a microscopic point it is considerably different from whole body exposures [1].

The stochastic risks from whole-body exposures are quantified by two different sets of quantities, referred to as the *protection* and *operational* quantities. The regulatory dose limits were established using the International Commission of Radiation Protection (ICRP) 60 [5] **protection quantities** of *equivalent dose*,  $H_T$  [ $Sv$ ], and *effective dose*,  $E$  [ $Sv$ ]. These quantities were designed to be strictly theoretical by incorporating the dose to each individual tissue and were not intended to be directly measurable.

The equivalent dose represents the sum of the products of the mean dose to a given tissue or organ,  $T$ , from radiation type,  $R$ , denoted as  $D_{T,R}$ , and the radiation weighting factor,  $w_R$ , for the radiation,  $R$ , incident on the body:

$$H_T = \sum_R D_{T,R} * w_R \quad (1.3)$$

In the case of mixed field exposures, such as gamma-neutron irradiation, the equivalent dose is the sum of the respective tissue doses and weighting factors for each radiation type. The radiation weighting factors are based on mean quality factor values and vary from 5 to 20 depending on neutron energy [1]. Effective dose is then determined as the sum of the product of the tissue weighting factor and the total equivalent dose in each tissue or organ respectively:

$$E = \sum_T w_T \sum_R D_{T,R} * w_R = \sum_T w_T H_T \quad (1.4)$$

The tissue weighting factor accounts for the variations in radiation sensitivity of different types of tissue. As it accounts for dose to every tissue or organ, radiation quality, and varying sensitivities of different tissue types, it is the effective dose on which dose limits are based. The Canadian dose limit for nuclear energy workers is 100  $mSv$  over five years, with a maximum of 50  $mSv$  in any one year [6]. As the effective dose is not directly measurable dosimetry records are kept in terms of a different quantity.

For practical dosimetry it is the International Commission of Radiation Units and Measurements (ICRU) defined **operational quantities** which are measured. These strive to estimate the effective dose using the energy deposited in a phantom that closely resembles the human torso. This results in the operational quantities being difficult, but theoretically possible to measure, thus allowing for instruments to be calibrated against standard reference values of

the operational quantities [7, 8]. The quantity used for whole body exposure to penetrating radiations such as neutrons and photons is the *ambient dose equivalent*,  $H^*(d)$  [9]. The ambient dose equivalent is defined as the dose equivalent to a point at depth  $d$  [mm] within the 30 cm diameter tissue equivalent ICRU sphere. For external penetrating radiations such as neutrons and photons the depth  $d = 10$  mm within the sphere is used. For determination of the reference values the ICRU sphere is exposed to a radiation source where the field is aligned and expanded so that the entire 30 cm sphere is exposed uniformly, as shown in Figure 1.2.

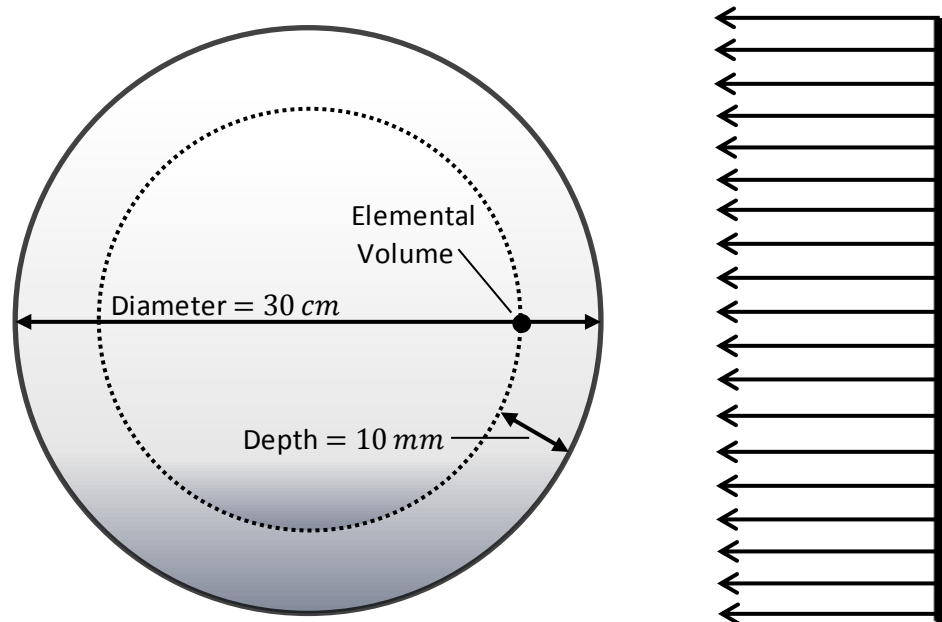


Figure 1.2 – Illustration of the ICRU 51 [9] described  $H^*(10)$  measurement conditions

As this is not a practical measurement, the reference values for monoenergetic neutrons are tabulated in ICRP 74 [10]. The ideal instrument should measure values consistent with the reference  $H^*(10)$  values over all neutron energies, and respond uniformly regardless of any in the neutron field. Up to this point neutron dosimeters, often referred to as rem-monitors, have worked using an engineered energy response that attempts to match the relation between neutron energy and  $H^*(10)$ .

### 1.3 Current Practices and Issues in Neutron Dosimetry

The current instruments capable of directly measuring neutron  $H^*(10)$  are cumbersome and costly [11]. Alternatively, neutrons are moderated so that the thermal neutron fluence [ $n/cm^2/s$ ] can be measured and converted to an approximate  $H^*(10)$ . This is done by surrounding a detector sensitive to thermal neutrons with a thick, heavy, polyethylene moderator. Thermal neutron sensitivity is obtained either by loading a proportional counter gas with  $^{10}\text{B}$  or  $^3\text{He}$ , or a scintillator crystal with  $^6\text{Li}$  [12]. Each of these isotopes readily produces easily detectable charged particles upon interacting with thermal neutrons. The cross sections of these neutron capture reactions are inversely proportional to neutron energy, meaning that the higher the neutron energy the less likely it will be counted.

This produces a response,  $R_\Phi$  [*counts per unit fluence*], which exhibits a strong energy dependence:

$$R_\Phi = \frac{M}{\Phi} \tag{1.5}$$

where  $M$  is the measured counts and  $\Phi$  is the true fluence [13]. This is further complicated by the conversion from neutron fluence to dose equivalent also being energy dependent, and having uncertainty ranging 5-10% for neutrons under 20 MeV [14]. As shown in Figure 1.3 higher energy neutrons contribute significantly more to the  $H^*(10)$  on a per neutron basis, but these neutrons also have smaller interaction cross sections in the gas or crystal.

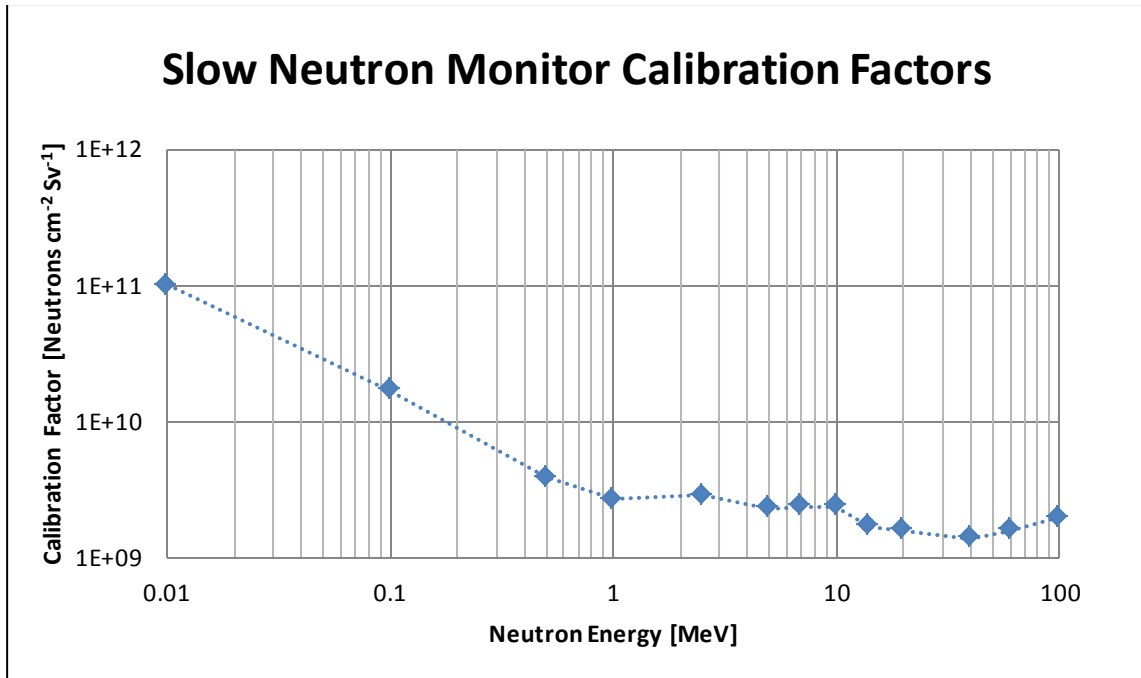


Figure 1.3 – Flux to Dose Equivalent conversion factors (based on US NRC data [15])

Slow neutron monitors obtain the  $H^*(10)$  using the measured counts,  $M$ , the energy dependent response,  $R_\Phi$ , and the energy dependent calibration factor,  $CF_E$  (shown in Figure 1.3):

$$H^*(10) = \frac{M}{R_\Phi} CF_E \quad (1.6)$$

The calibration of a slow neutron monitor requires measurements to be taken at three positions of known neutron fluence in a well-defined field. As the energy of the neutrons in the calibration field are known the appropriate energy response is also known. Since this calibration factor and energy response continues to be used in the reactor building, accurate measurements require a calibration field similar to reactor building fields. There are two challenges with this:

- (1) Neutron fields within the reactor building vary greatly (see Figure 1.1)
- (2) Readily available calibration fields do not resemble these reactor fields

The reference neutron sources for calibration of thermal neutron counters, as described in ISO Standard 8529-1, include  $^{252}\text{Cf}$ ,  $\text{D}_2\text{O}$ -moderated  $^{252}\text{Cf}$ ,  $^{241}\text{Am-B}$ , and  $^{241}\text{Am-Be}$  [16].

Measurements using an instrument calibrated with the relatively high energy neutrons produced by an  $^{241}\text{Am-Be}$  source found the true  $H^*(10)$  within the reactor building was overestimated by a factor of 2.2 [4]<sup>1</sup>. This has led to the conclusion that even with a very precise calibration an improper calibration source strongly affects the accuracy of  $H^*(10)$  measurements [17]. However, when alternative calibration sources were analyzed in terms of the average  $H^*(10)$  per unit fluence they were also found to differ significantly from many of the fields encountered in reactor buildings [4].

#### 1.4 TEPCs as an Alternative to Moderator Based Counters

It may be possible to increase accuracy in neutron dosimetry with the use of TEPCs [3]. TEPCs are lightweight instruments comprised of thin tissue equivalent walls and filled with low density tissue equivalent gas. The nature of these instruments as dual spectrometers of energy deposition and ionization density permits direct  $H$  measurement that can be used as an approximate measure of the  $H^*(10)$ .

Dual spectrometry refers to the microdosimetric measurements of both the specific energy,  $z_i [J/kg = Gy]$ , and the lineal energy,  $y_i [keV/\mu m]$ , for each interaction. As lineal energy very closely approximates LET, they are interchangeable when determining the quality factor. The  $H$  can then be determined as the sum of the product of the dose and the quality factor for each lineal energy value:

$$H = \sum_i z(y_i) * Q(y_i) \cong H^*(10) \quad (1.7)$$

Unfortunately the TEPC  $H^*(10)$  response also has an energy dependent variance similar in magnitude to the moderator-based method, as shown in Figure 1.4. However, when

---

<sup>1</sup> The value of the true  $H^*(10)$  was determined by measuring the neutron fluence spectra and using the appropriate conversion factor for  $H^*(10)$  per unit fluence in each energy bin [4]

considered in the context of the mean energy distribution of the neutron fields of interest, shown in Figure 1.5, the impact of this response becomes much less substantial.

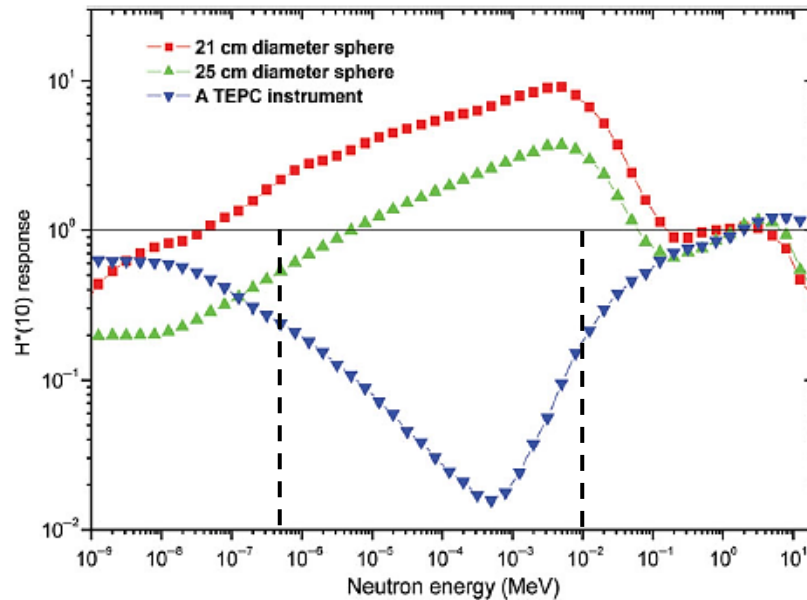


Figure 1.4 – Response functions of two typical-sized moderator-based survey instruments and a TEPC; neutron energies 0.5 eV and 10 keV are indicated to aid further discussion given below (adapted from [1])

Figure 1.5 was determined by taking the mean fractions of the total  $H^*(10)$  and fluence within each energy range at each of the six locations within the reactor building presented in Figure 1.1. This demonstrates that the overall relative fluence and  $H^*(10)$  contributions fluctuate greatly as a function of neutron energy. Both the TEPC and moderated-based method respond well within the energy range 100 keV to 1 MeV ( $10^{-1}$  MeV to  $10^0$  MeV), which deposits an average of 60% of the total neutron  $H^*(10)$ . The TEPC response declines significantly between the range of 0.5 eV to 10 keV ( $5 \times 10^{-6}$  MeV to  $10^{-2}$  MeV), where the over-response of the moderator-based instruments peaks. However, Figure 1.5 shows that although these low energy neutrons account for 49% of the mean total fluence, they only contribute an average of 9% to the total  $H^*(10)$ . The remaining 91% of the  $H^*(10)$  is due to neutrons with energies less than 0.5 eV, or greater than 10 keV (both of these energies are indicated on Figure 1.4). Within

these ranges the qualitative  $H^*(10)$  response deviations appear to be comparable for the TEPC and the moderator-based method. This shows TEPCs appear to have an acceptable  $H^*(10)$  response, especially in the high energy range responsible for the bulk of the  $H^*(10)$  in reactor fields.

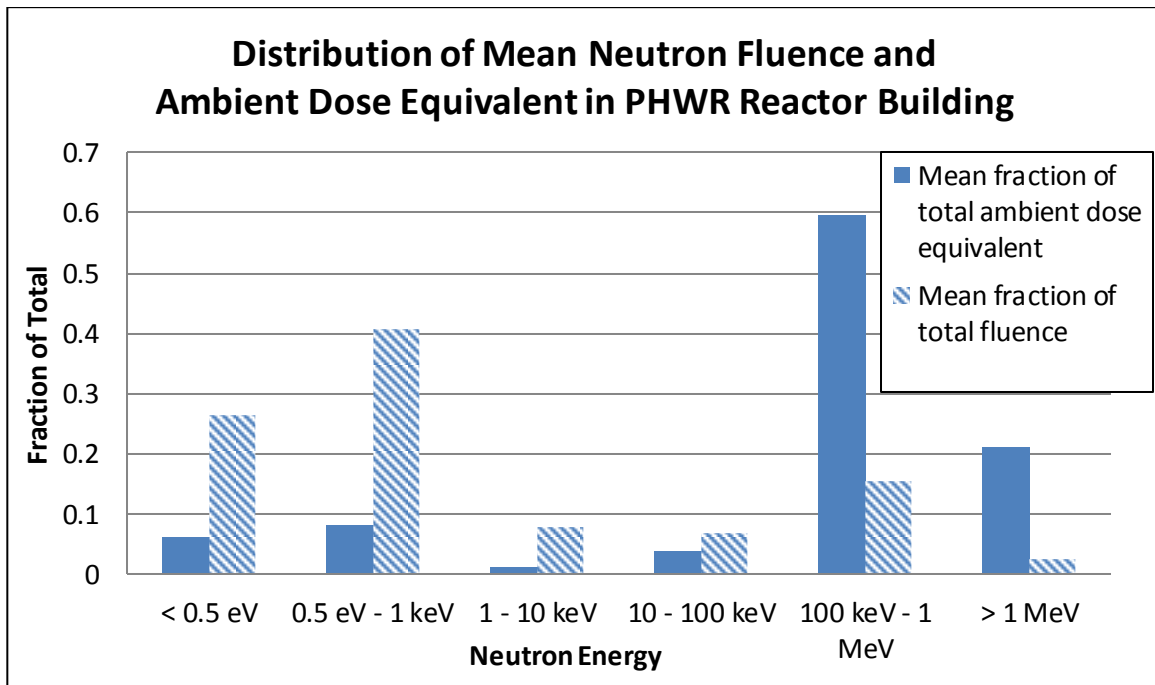


Figure 1.5 – Mean fraction of total fluence and ambient dose equivalent over all measurement locations in Figure 1.1 (adapted from [4])

TEPCs also have the following benefits over the moderator-based counters which make them ideal candidates for portable instruments:

- Lightweight
- Tissue equivalence means that dose to tissue is more directly measured
- Direct  $H^*(10)$  measurement as lineal energy allows determination of the quality factor
- No need for calibration facility with neutron fields; internal alpha source or self-calibration is possible

- Ability to simultaneously measure the  $H^*(10)$  for both neutrons and photons, effectively replacing two instruments by one
- Potential for dramatically decreased detector size with use of Multi Element Tissue Equivalent Proportional Counters (METEPCs)

It is possible to decrease overall detector size while maintaining high sensitivity [*counts/Sv*] by using METEPCs. This works by using many small independent counters that are all connected to a single output, making it possible to match the surface area of a much larger detector in a smaller volume. Such a design is simply not feasible for a moderator based counter as there is no means of miniaturizing the cumbersome moderating material.

Previous METPEC designs have been highly complex, making them difficult to manufacture and cost-prohibitive beyond experimental use. One major issue is the difficult installation of anode wires for up to 296 elements in these METEPCs [18]. The anode wires are also an issue for portable instrumentation as they respond to audible noise and vibrations by producing spurious counts, known as microphonic noise. Electronic microphonic noise arises from the physical movements of the anode wire in the counter and the associated time varying capacitance of the detector. This thesis applied both computational electrostatic analysis and Monte Carlo neutron transport and energy deposition simulations in an attempt to improve on the existing METEPC element design. The specific objectives of this work are outlined in the following section.

## 1.5 Research Objectives

This thesis aims to provide the foundation for future work on an alternative portable instrument for neutron monitoring and dosimetry. The goal is to achieve this by addressing issues identified with current METEPC element designs with an analysis of a new element design.

The proposed solution was reached through an electrostatic investigation of various counter geometries, and consists of a hemispherical element with a concentric ball anode. This provides an alternative solution to the traditional anode wire.

As the proportional counter geometry is novel, performance was analyzed for a single element, allowing for the possibility to scale the design up to an METEPC for future work. Performance was evaluated relative to current counters via a set of comparative analyses that also included a commercial spherical TEPC, and a cylindrical element from a recent METEPC design. Counters were assessed in terms of the uniformity and patterns of both the energy depositions by neutrons and the gas gain. Gas gain is a critical feature of proportional counter operation and determines the amplification of the signal through the multiplication of the electrons generated by charged particle interactions with the counter gas. This multiplication takes place as the electrons are drifted and collected in the region of high electric field close to the anode.

The technical objectives for the new design include:

- A wire-less anode
- Dose equivalent response and microdosimetric distributions comparable to the current gold standard of microdosimetry, the spherical TEPC
- Directionally independent response
- Uniform gas multiplication independent of initial ionization location

The potential practical implications of a wire-less anode design include a greatly simplified construction and reduced or eliminated microphonic noise.

## 1.6 Thesis Outline

This chapter demonstrated that TEPCs are capable of improving the accuracy of neutron monitoring in reactor fields while reducing instrument size. Pragmatic qualities were then defined for a new METEPC element design that would address current issues. The pertinent background in experimental microdosimetry is expanded upon in Chapter 2, including the calculation of the operational quantities and the respective error in microdosimetric measurements. Subsequently, Chapter 3 provides a historical review of the TEPCs used for neutron monitoring, which is used to explain the specific issues encountered with current designs. A potential solution is then proposed with a new hemispherical TEPC design. In Chapters 4 and 5 an account of the performance analysis conducted for the new design alongside two current TEPC designs is given. The gas gain is characterized in Chapter 4 by analyzing the magnitude and dimensions of the electron avalanche throughout each counter cavity and in Chapter 5 the dosimetric qualities of each design are evaluated using neutron monitoring simulations conducted with the Monte Carlo code PHITS. The results discussed in Chapters 4 and 5 are brought together in Chapter 6 where general conclusions are drawn regarding the performance of each of the three detectors and recommendations for future works are given.

## Chapter 2: Experimental Microdosimetry

### 2.1 Introduction

When humans are exposed to ionizing radiation there is a chance biological damage can occur, with cancer generally being of greatest concern. Such damages are the outcome of a complex chain of chemical processes that is not yet fully understood [19]. Despite the incomplete understanding the degree of biological effect has repeatedly been correlated with the ionization density along the tracks of charged particles [20]. Experimental microdosimetry is one of the only means for measuring both ionization density and absorbed dose for each event in real time. In microdosimetry an event is defined as when a charged particle crosses the gas cavity of a detector simulating a real microscopic tissue volume and creates at least one electron-ion pair. The most frequently simulated site sizes are either 1  $\mu\text{m}$  or 2  $\mu\text{m}$  in diameter, which are simulated using TEPCs filled with low density gas.

The applications of microdosimetry started in the field of radiobiology [19]. This involved relating cell survival to microdosimetric quantities by measuring dose and radiation quality. Such experiments are the basis of the Theory of Dual Radiation Action (TDRA), which provides a biological explanation for the relationship between radiation quality and biological response [21]. The field of experimental microdosimetry largely focuses on measurements with TEPCs in radiation fields of interest for radiotherapy and radiation protection. It is the applications in radiation protection which are the focus of this thesis. The radiation protection dose limits serve to limit stochastic risk to acceptable levels. These limits account for relative biological responses by using LET to determine radiation weighting factors. As radiation quality varies most significantly for neutrons, the capacity of directly measuring operational quantities, such as the dose equivalent, makes experimental microdosimetry invaluable.

## 2.2 Experimental Microdosimetry Concepts

### 2.2.1 Basics of Tissue Equivalent Proportional Counters

The main instrument of experimental microdosimetry is the TEPC. TEPCs are homogeneously tissue equivalent on an atomic basis, and consist of a plastic shell filled with low density gas. They are able to measure dose to unit density tissue on the basis of Bragg-Gray cavity theory (Section 2.2.1.1). The use of low density gas enlarges the simulated site in order to greatly increase the number of intercepting particles. This increases the number of interactions by approximately  $10^{10}$  fold the number that would occur in a comparable unit density microscopic tissue site [19]. The energy deposited in the sensitive gas volume during these interactions is determined by measurement of a voltage pulse which has a magnitude proportional to the initial number of ionizations. How this occurs is explained by examining the fundamentals of proportional counter functionality.

Proportional counters have many parallels to other gaseous detectors, specifically Geiger-Muller (GM) counters and ion chambers. Each of these uses a gaseous sensitive medium in which electron-ion pairs are generated by energy deposition and an electric field is used for transport and collection of these charges. These three types of detectors are distinguished by their resulting output. Ion chambers measure the total charge generated in the gas, which is a measure of the total number of electron-ion pairs generated in the gas. This can be converted to the absorbed dose using the reference mean energy deposition per ion pair, referred to as the W value. GM counters simply output the number of energy deposition events either as a cumulative tally or as a count rate per unit time. Proportional counters combine the features of both ion chambers and GM counters by measuring a signal proportional to the charge generated by each individual event. With proper calibration the energy imparted by each event is known.

The different types of output for each detector type stems from the different magnitudes of electric field applied within the gas cavities. Proportional counters are operated at an intermediate high voltage in order to quickly collect electrons, while also consistently amplifying the number of free electrons within the gas. Consistent multiplication is achieved through the spatial variation of the electric field strength, which results in amplification only occurring very close to the anode. This amplification referred to as gas gain can range from a factor of ten up to several thousands. When the avalanche region where nearly all of the gas gain occurs is both uniform and suitably confined in space the pulse magnitude is then directly proportional to the number of initial electrons and thus the energy deposited, regardless of the path taken by a charged particle through the gas cavity.

#### *2.2.1.1 Cavity Theory & Fano's Theorem*

In TEPCs it is desired that the energy deposited within the simulated site be representative of the energy deposited in the walls, which serve as simulated unit density tissue. For this to be true TEPCs must function as cavity chamber dosimeters. This is established theoretically through Bragg-Gray cavity theory and Fano's theorem.

Bragg-Gray cavity theory requires that TEPCs achieve the conditions for Charged Particle Equilibrium (CPE) [22]. When CPE is achieved the charged particle fluence is uniform throughout the walls and cavity. This is said to be true when each charged particle exiting the cavity is compensated for by an indistinguishable charged particle entering the cavity. Indistinguishable meaning having the same mass, charge, and an initial kinetic energy equal to the kinetic energy of the first particle as it left the gas cavity.

The required conditions for achieving CPE have been defined by Ségur et al. [22] as:

1. The atomic composition of the walls and cavity are homogenous
2. The density of the walls and cavity are homogenous
3. There should be negligible attenuation of any indirectly ionizing particles in the medium

The first condition is achieved as TEPCs are homogeneously tissue equivalent; the specifics of their compositions are outlined in Section 2.2.1.2. Although atomically similar, the densities of the walls and the gas are far from homogeneous. The density of the walls ranges from  $10^4$  to  $10^6$  fold the density of the gas. This can affect measurements by shifting the frequency distribution towards slightly higher values. The shift is due to wall effects, which are reported even in experiments using atomically homogenous counters [23]<sup>2</sup>. The wall effect results from the enlarged physical volume of the simulated site relative to the actual site. By increasing the volume, scattering and delta ray events may enter the simulated site where they would not enter the actual tissue site [24]. Wall effects only contribute noticeably in the cases of either very high energy particles (well over 10 MeV) or for very small simulated sites ( $< 1 \mu\text{m}$ ), for all other cases the wall effect is negligible [19].

Fano's theorem provides an alternate justification for the functionality of TEPCs as cavity chamber dosimeters. It implies that despite deviating from the second condition of CPE the concentration of free electrons generated in the gas cavity remains equivalent to that in the wall. Fano's theorem states [25]:

In a medium of given composition exposed to a uniform flux of primary radiation (such as X-rays or neutrons) the flux of secondary radiation is also uniform and *independent of density of the medium* as well as of the density variation from point to point.

---

<sup>2</sup> The experiments using homogenous counters employed ethylene gas and polyethylene walls [23]

This applies to TEPCs as they are homogeneous counters designed with the intent of not altering the primary radiation flux or energy spectrum. TEPC wall thickness is selected to be infinitely thick with respect to the secondary radiation(s). In the case of neutron exposure, the secondary charged particle with the greatest range is a proton with the kinetic energy of the maximum neutron energy. By ensuring that the wall thickness is not much thicker than the maximum proton range both the third condition of CPE and Fano's theorem are satisfied. With the appropriate wall thickness selected, the neutron field is not moderated or altered significantly prior to reaching the cavity. However, challenges fulfilling these conditions can arise when attempting to design a single detector for a wide range of neutron energies as CPE requirements vary with neutron energy.

#### *2.2.1.2 Tissue Equivalent Materials*

The tissue equivalence of TEPCs is based on the atomic composition as this has been observed to be the main factor governing radiation interactions and energy transfer in matter. Effects due to the specific chemical bonds between atoms are believed to be in the range of only 1% of the total energy transferred and are considered negligible as that is insignificant relative to experimental uncertainty [26].

The atomic composition that the tissue equivalent (TE) materials emulate is the ICRU defined muscle tissue [27]. The element weight percent values for both ICRU muscle tissue and the TE materials presented in Table 2.1 demonstrate that this is done with only minor compromises of tissue equivalence, as required for detector functionality. Detector walls are constructed out of the muscle equivalent plastic, A-150 (Exradin, Lisle, IL, USA). There are two standard TE gas mixtures, with the main difference between them being that one is methane based and the other is propane based. The propane based mixture was used exclusively within this thesis as it produces better counting characteristics including higher gas gain when using the

same applied voltage [23, 28]. The reason gain is increased is that being a higher hydrocarbon propane has a lower mean ionization energy than methane. By lowering the mean ionization energy (W value) more electron-ion pairs are created for a given energy deposition, improving counting statistics.

Material	H	C	N	O	F
ICRU Muscle Tissue	10.2	12.3	3.5	72.9	-
Muscle Equivalent Plastic (A-150)	10.1	77.6	3.5	5.2	1.7
Muscle-equivalent gas (propane based)	10.3	56.9	3.5	29.3	-

Table 2.1 – Composition of tissue equivalent materials by element weight percent [27, 29]

Comparing the relative atomic composition of ICRU muscle tissue to the TE materials it can be seen that in both of the TE materials carbon substitutes for most of the oxygen present in ICRU muscle tissue. A-150 requires a high carbon content to produce electrical conductivity, a basic requirement for cathode functionality. The high electronegativity of gaseous oxygen leads to it readily bonding with free electrons. At the high oxygen concentrations present in tissue this would result in a much lower gas gain. With carbon being electropositive, its use in place of oxygen promotes an increase in gas gain [20]. Fortunately, carbon and oxygen are fairly similar atoms that undergo similar radiation interactions with comparable probabilities (see Sections 2.3.1 and 2.3.3). This means that despite the large differences in carbon and oxygen content between TE materials and ICRU muscle tissue the types and probabilities of interactions remain relatively unchanged.

### 2.2.1.3 Scaling Microscopic Sites

TEPCs are able to simulate microscopic tissue sites within the macroscopic gas cavities by using very low pressure TE gas. By virtue of the detectors tissue equivalence the mass stopping

power,  $\left(\frac{dE}{dx} * \frac{1}{\rho}\right)_i$ , is equal in the gas and in ICRU muscle tissue:

$$\left(\frac{dE}{dx} * \frac{1}{\rho}\right)_{gas} = \left(\frac{dE}{dx} * \frac{1}{\rho}\right)_{tissue} \quad (2.1)$$

The appropriate pressure for simulating a site is determined such that the product of the density,  $\rho_i$ , and site diameter,  $\Delta X_i$ , is equal for the simulated and actual tissue sites:

$$\rho_{gas} * \Delta X_{gas} = \rho_{tissue} * \Delta X_{tissue} \quad (2.2)$$

For clarification,  $\Delta X_{gas}$  represents the physical diameter of the gas cavity, the density of tissue is  $1 \text{ g} * \text{cm}^{-3}$ , and  $\Delta X_{tissue}$  is the diameter of the simulated site. As the simulated and actual tissue sites have the same effective diameter [ $\text{g} * \text{cm}^{-2}$ ] and mass stopping power, radiation interactions deposit equivalent amounts of energy,  $E_i$ :

$$E_{gas} = E_{tissue} \quad (2.3)$$

This is fully illustrated as:

$$\left(\frac{dE}{dx} * \frac{1}{\rho}\right)_{gas} * \rho_{gas} * \Delta X_{gas} = \left(\frac{dE}{dx} * \frac{1}{\rho}\right)_{tissue} * \rho_{tissue} * \Delta X_{tissue} \quad (2.4)$$

The gas density for simulating a specific site size is then determined from the ratio of the tissue to gas diameters:

$$\rho_{gas} = \rho_{tissue} \left(\frac{\Delta X_{tissue}}{\Delta X_{gas}}\right) \quad (2.5)$$

Which is then converted from density [ $\text{g}/\text{cm}^3$ ] to pressure [ $\text{torr}$ ] using the ideal gas law:

$$p = \rho_{gas} \left(\frac{RT}{M_{gas}}\right) \quad (2.6)$$

where the gas constant  $R = 62365 \text{ cm}^3 * \text{torr} * \text{K}^{-1} * \text{mol}^{-1}$ , the temperature  $T = 293.15 \text{ K}$ , and  $M_{gas}$  represents the molar mass of the propane-based TE gas. The molar mass of propane

based TE gas is calculated using the partial pressure of each of the gas components as the mole fraction, along with the respective molar mass values for each gas, as shown in Table 2.2.

Gas	Propane	Carbon Dioxide	Nitrogen
Mole Fraction [%]	55	39.6	5.4
Molar Mass [ <i>g/mol</i> ]	44.0956	44.0095	28.0134

Table 2.2 – Molar properties of gases used for propane based TE gas

The effective molar mass for the gas mixture is the sum of the products of the molar mass,  $M$ , and mole fraction,  $n_f$ , values for each of the gas components listed in Table 2.2:

$$M_{gas} = \sum M_i * n_{f_i} = 43.19307 \text{ g} * \text{mol}^{-1} \quad (2.7)$$

The gas pressure required for simulating a 2  $\mu\text{m}$  diameter site with a 12.7  $\text{cm}$  diameter spherical TEPC can then be determined using Equations 2.5 and 2.6 as:

$$\rho_{gas} = (1 \text{ g} * \text{cm}^{-3}) \left( \frac{2 * 10^{-4} \text{ cm}}{12.7 \text{ cm}} \right) = 1.575 * 10^{-5} \text{ g} * \text{cm}^{-3}$$

$$p = (1.575 * 10^{-5} \text{ g} * \text{cm}^{-3}) \left( \frac{62365 \text{ cm}^3 * \text{torr} * \text{K}^{-1} * \text{mol}^{-1} 293.15 \text{ K}}{43.19307 \text{ g} * \text{mol}^{-1}} \right)$$

$$p = 6.6657 \text{ torr}$$

## 2.3 Particle Interactions with Tissue

### 2.3.1 Neutron Interactions

Neutrons are uncharged subatomic particles with essentially the same mass as a proton. As they are unaffected by electromagnetic forces, neutron interactions result from the strong force when they come in very close proximity to an atomic nucleus. The probability of neutron interaction is quantified by the total cross section,  $\sigma_{Total}$  [*barns*], which is the sum of the cross sections for all possible reactions:

$$\sigma_{Total} = \sigma_{Elastic\ scatter} + \sigma_{Inelastic\ scatter} + \sigma_{Capture} + \sigma_{Fission} + \sigma_{Spallation} \dots$$

As neutron cross sections are highly energy dependent they will be discussed using the following kinetic energy classifications:

*Thermal neutrons:  $\leq 0.025\ eV$*

*Intermediate neutrons:  $0.025\ eV - 10\ keV$*

*Low energy fast neutrons:  $10\ keV - 10\ MeV$*

*Fast neutrons:  $10\ MeV - 20\ MeV$*

*Relativistic neutrons:  $> 20\ MeV$*

Since relativistic neutrons are not encountered in the reactor fields relevant to this work, neutron interactions in tissue will only be discussed up to 20 MeV.

Thermal neutron interactions are dominated by capture reactions. These reactions involve a neutron entering the nucleus, which stabilizes via emission of either a photon or a heavy charged particle. The cross sections of all capture reactions are inversely proportional to neutron energy:

$$\sigma_{Neutron\ Capture} \propto \frac{1}{E_{Kinetic}} \quad (2.8)$$

In tissue the types of capture reactions include:  $(n, \gamma)$ ,  $(n, p)$ , and  $(n, \alpha)$ . Though each of these types of capture can occur, the only important reactions are  ${}^1_1H(n, \gamma){}^2_1H$  ( $E_\gamma = 2.224\ MeV$ ) and  ${}^{14}_7N(n, p){}^{14}_6C$  ( $Q = +0.62\ MeV$ ), as these account for just under 88% and 12% of the abundance weighted neutron capture cross section, respectively [30]. The 0.62 MeV released during nitrogen capture is shared between the proton (0.58 MeV) and the recoiling carbon nucleus

(0.04 MeV) [31]. As neutron energy increases the cross sections for neutron capture reactions decline.

Intermediate and low energy fast neutrons predominately undergo elastic scattering. Elastic means that the kinetic energy of the incident neutron is distributed between the scattered neutron and recoil nucleus, without exciting the nucleus in the process. All of the electron(s) of the recoil nuclei are stripped immediately following the interaction, converting the atomic nucleus into a heavy charged particle. The relative probability of elastic scattering occurring is dependent on the atom.

Hydrogen has by far the largest elastic scattering cross section; making recoil protons the most frequently produced heavy charged particles in tissue. It is also unique in that it is the only atom to which a neutron can transfer its entire energy. The maximum fraction of the incident neutrons energy that can be transferred to heavier nuclei is restricted due to interaction kinematics. The maximum fraction of the incident neutrons kinetic energy that can be transferred to carbon, nitrogen, and oxygen atoms is 28.4%, 24.9%, and 22.2%, respectively. The elastic scattering cross sections for these heavier nuclei are so much smaller than for hydrogen, that even when weighted by relative abundance in tissue, as shown in Figure 2.1, they still remain well under the hydrogen cross section.

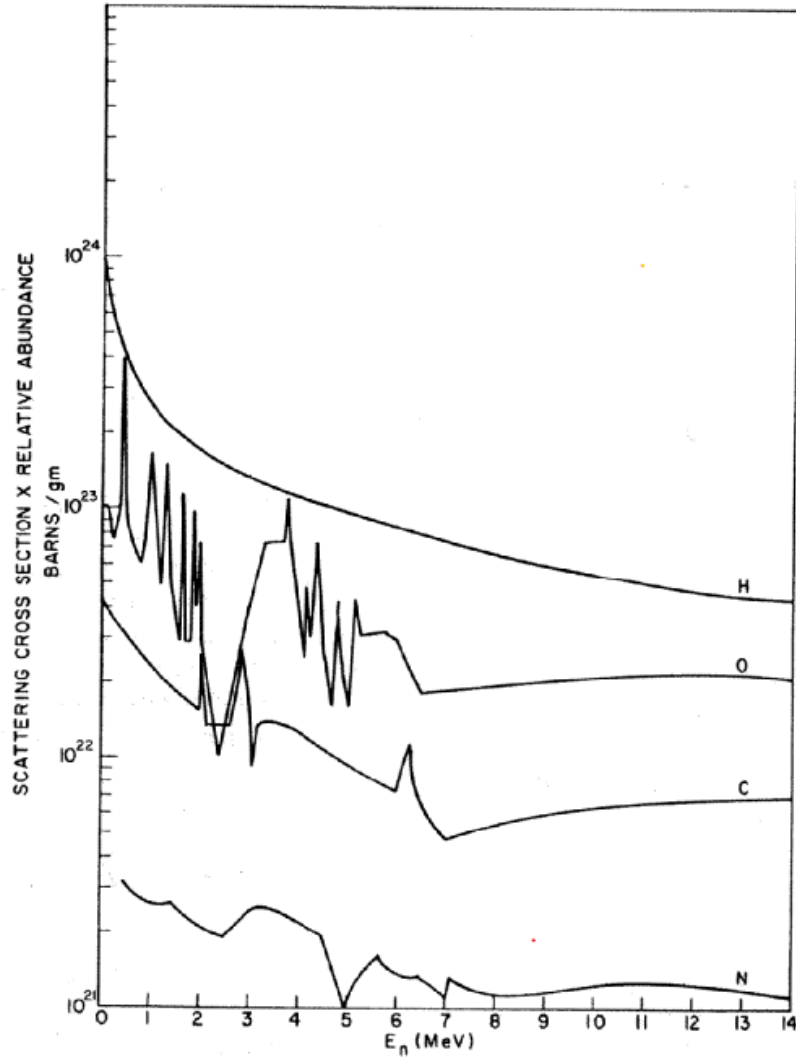


Figure 2.1 – Abundance weighted elastic scattering cross sections for H, O, C and N between 0 MeV and 14 MeV [30]

Low energy fast neutrons begin to exceed the minimum energy thresholds of inelastic scattering reactions. Despite exceeding thresholds all of the inelastic scatter cross sections remain at nearly zero in tissue for neutrons below 10 MeV [23]. At neutron energies greater than 10 MeV both elastic and inelastic scattering occurs in tissue, with inelastic scattering increasing as a function of neutron energy up to 15 MeV [30]. Inelastic scattering requires a portion of the incident neutrons kinetic energy goes to the excitation of the scattered nucleus. The result of this is that the recoil nucleus immediately de-excites via particle emission as well as shedding its electron(s) and recoiling as a heavy charged particle. At energies greater than 10

MeV the reactions for oxygen and carbon atoms are slightly different, leading to a minor compromise of tissue equivalence in this energy range. The differences between these reactions include the alpha producing inelastic scattering interactions  $^{16}\text{O}(n, \alpha)^{13}\text{C}$ , and  $^{12}\text{C}(n, \alpha)^9\text{Be}$  which have Q values of -2.21 MeV and -5.70 MeV, respectively [30]. The different Q values produce alpha particles of different energies and the reaction cross sections are also of different magnitudes. However, this is not a major drawback as elastic scattering is by far the dominant source of energy deposition even for neutrons with energies upwards of 20 MeV.

### *2.3.1.1 Classification of Recoil Interactions*

When interacting with tissue, a recoil nucleus is the most likely outcome for neutrons ranging from 10 keV to upwards of 20 MeV. Comparing relative probabilities of the various points of origin and termination for these secondary charged particles gives insight into particle tracks and energy deposition patterns. This also justifies the ionization density measurements conducted with TEPCs. The classification of recoil nuclei is based on points of origin and termination, as illustrated in Figure 2.2, with the four classes defined by Caswell [32] as:

1. Insider: both starts and ends within the gas cavity depositing its full energy
2. Starter: originates within the gas cavity, but does not deposit its full energy before exiting the cavity
3. Stopper: originates in the wall depositing some of its energy prior to entering the cavity, where it deposits the remainder of its energy
4. Crosser: originates in the wall and depositing a portion of its energy prior to the cavity, in the cavity and ends after crossing the cavity re-entering the wall

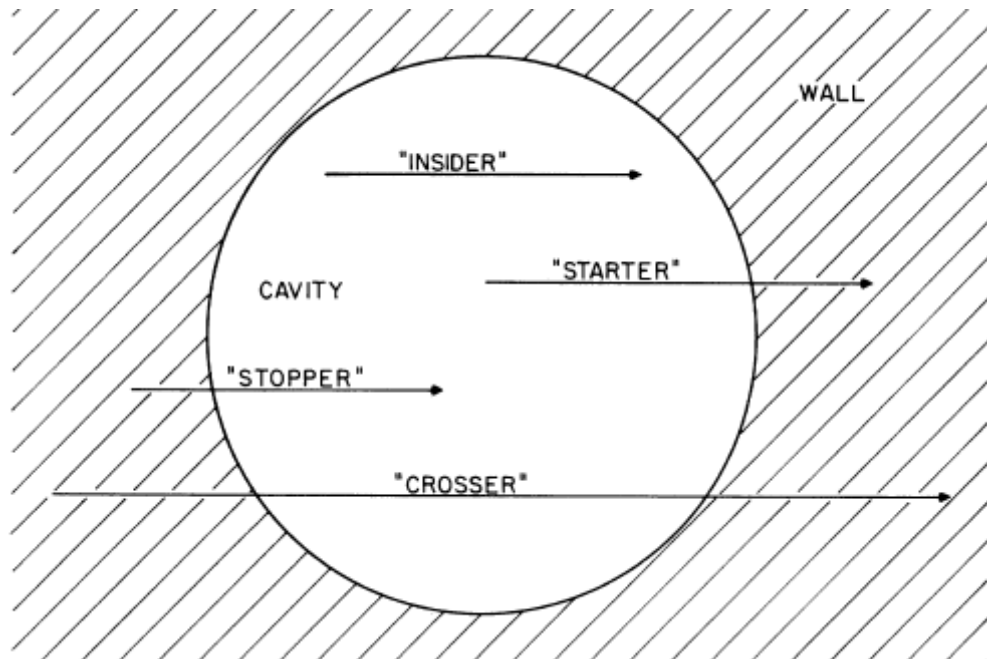


Figure 2.2 – Classification of charged particle tracks within a proportional counter [32]

Insiders are either low energy protons or heavy recoil nuclei with extremely short ranges. As these particles do not cross the entire cavity their ionization densities are underestimated. This is not a major issue since low pressure conditions within the gas cavity makes such interactions improbable. With the atomic density in the walls being several orders of magnitude higher than in the gas most recoil nuclei will originate in the wall, have sufficient energy to cross the microscopic simulated site diameter and then end their track in the wall. This makes crossers generally the greatest source of energy deposition.

### 2.3.2 Charged Particle Interactions

The charged particles that result from neutron interactions with tissue range from recoil carbon nuclei to electrons. This is a broad spectrum of both mass and charge, resulting in diverse patterns of energy deposition. As the patterns of energy deposition can be generalized into those of the various heavy charged particle and those of electrons they are discussed separately. Both of these types of charged particles deposit 99% of their kinetic energy in tissue via Coulomb interactions [11] with the electron cloud [33].

When heavy charged particles interact with the electron cloud they apply a force to the atomic electron. This force is proportional to the ions charge,  $z$ , and inversely proportional to the square of the distance between the ion and the electron,  $r$  [34]:

$$F_{Coulomb} \propto \frac{z}{r^2} \quad (2.9)$$

When sufficient force is applied the atomic electron is either brought to an excited state or the atom is ionized. The mean energy lost by the ion over many of these interactions is the stopping power. This is modelled analytically by the Bethe stopping power formula for heavy charged particles [35, 36]:

$$-\frac{dE}{dx} = \frac{4\pi k_0^2 z^2 e^4 n}{mc^2 \beta^2} \left[ \ln \frac{2mc^2 \beta^2}{I(1 - \beta^2)} - \beta^2 \right] \quad (2.10)$$

where Coulombs constant  $k_0 = 8.988 \times 10^9 \text{ N} \cdot \text{m}^2 \text{C}^{-2}$ , the electrons charge  $e = 1.602 \times 10^{-19} \text{ C}$ ,  $n$  is the electron density,  $I$  is the materials mean excitation energy,  $mc^2$  is the rest energy of the target electron, and  $\beta = v/c$  which is the velocity of the ion relative to the speed of light. The stopping power for heavy charged particles is proportional to the square of the ions charge and inversely proportional to its velocity:

$$-\frac{dE}{dx} \propto \frac{(ze)^2}{v^2} \quad (2.11)$$

As heavy charged particles slow down they eventually begin picking up atomic electrons, reducing their effective charge [19]. This decrease in charge occurs simultaneous with the decrease in velocity, producing the characteristic stopping power curve. An example of this is shown in Figure 2.3, with the Bragg peak occurring around 3.75 MeV where the carbon ion exhibits its maximum stopping power.

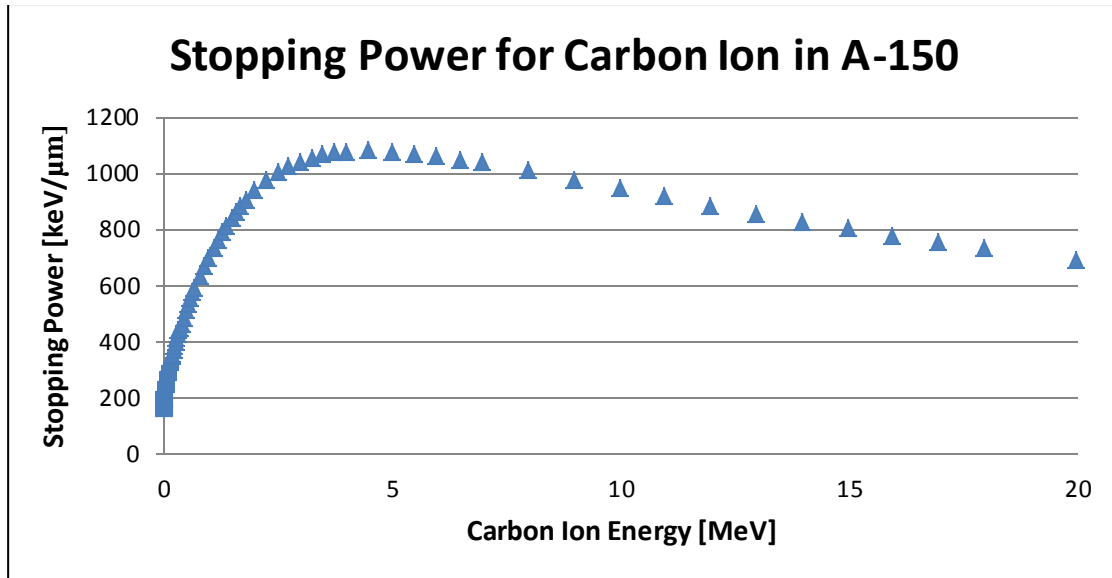


Figure 2.3 – Stopping power as a function of neutron energy for carbon ion in TE A-150 (data from [37])

The decrease in stopping power at energies below the Bragg peak is due to the decrease in effective charge as the charged particle accumulates electrons. Barkas' [38] model for determining effective charge,  $z^*$ , shows how it is reduced as velocity decreases:

$$z^* = z[1 - e^{-125\beta z^{-\frac{2}{3}}}] \quad (2.12)$$

The fixed charge of electrons results in much more consistent ionization densities along their tracks and also means that they do not exhibit a Bragg peak. As free electrons are identical to the atomic electrons which they are interacting with they require a distinctive model from the much more massive heavy charged particles. The collisional stopping power for electrons is calculated using the first Born approximation of the Bethe formula [39]:

$$\left(-\frac{dE}{dx}\right)_{col} = \frac{2\pi k_0^2 e^4 n}{mv^2} \left[ \ln\left(\frac{mv^2 T}{2I^2(1-\beta^2)}\right) - (2\sqrt{1-\beta^2} - 1 + \beta^2) \ln 2 \right. \\ \left. + 1 - \beta^2 + \frac{1}{8} \left(2 - 2\sqrt{1-\beta^2} - \beta^2\right) \right] \quad (2.13)$$

where  $T = \frac{1}{2} m_0 v^2$ , representing the kinetic energy of the incident electron and all other symbols are as defined for Equation 2.10. As electrons have a consistent charge their collisional stopping power is simply inversely proportional to kinetic energy:

$$\left(-\frac{dE}{dx}\right)_{col} \propto \frac{1}{T} \quad (2.14)$$

The rates of energy deposition for individual heavy charged particles and electrons vary from the mean stopping powers defined by Equations 2.10 and 2.13. These variations are due to energy straggling, the Fano factor and range straggling. Energy straggling refers to fluctuations in both the number and the outcomes of individual interactions, resulting from variations in energy loss during interactions. The Fano factor characterizes the variation in the total number of ion pairs produced by a given energy deposition. Together these variabilities broaden distributions and produce range straggling, which is variation from the mean particle range. These variations are exhibited during all charged particle interactions and contribute to the stochastic nature of the quantities measured in experimental microdosimetry.

### 2.3.3 Photon Interactions

Photons always accompany neutron fields, whether resulting from neutron interactions in hydrogenous materials such as tissue or concrete, or from interactions occurring within nuclear reactors or neutron generators [40]. As such neutron dosimetry must always be accompanied by photon dosimetry. Photons are massless indirectly ionizing particles that interact through direct collisions. Depending on photon energy these collisions either occur with the orbital electrons or the atomic nucleus. The probabilities of different photon interactions are mainly factors of photon energy and the medium's effective atomic number,  $Z_{eff}$ , which is approximately seven for tissue.

The three main photon interactions are the photoelectric effect, Compton scattering, and pair production. Relative probabilities as a function of photon energy for each of these interactions are summarized in Figure 2.4.

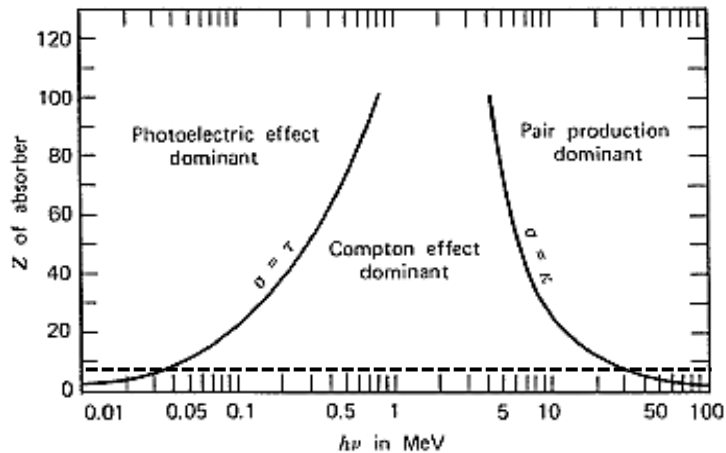


Figure 2.4–Relative importance of the three major interactions of photons with matter;  $z \sim 7$  is indicated to represent tissue (adapted from [41])

Figure 2.4 shows that in tissue the Compton Effect is the main interaction for photons energies ranging 0.03 MeV to 30 MeV. It can be presumed that nearly all of the 2.224 MeV gamma rays produced via neutron capture in hydrogen will almost exclusively undergo Compton scattering. During Compton scatter a photon transfers a portion of its energy to an orbital electron, resulting in a scattered photon, scattered electron and ionized atom. The kinetic energy of the free electron is equal to the energy  $h\nu$  lost by the photon minus the atoms electron binding energy.

Similarly, the photoelectric effect produces a free electron, but it involves the photon transferring its entire energy to an inner orbital electron. During pair production the photon interacts with the nucleus and in its place an electron and positron are produced, with the positron subsequently undergoing annihilation with an electron producing two 0.511 MeV photons. In summary, it is most probable that the photons found in a reactor workplace environment will either be 2.2 MeV capture gamma rays from thermal neutron interactions or

high energy gammas from  $^{59}\text{Co}$  activation to  $^{60}\text{Co}$ . In both cases Compton scattering is the most likely photon energy transfer process in tissue.

## 2.4 Microdosimetric Quantities and Distributions

### 2.4.1 Lineal Energy

Using the conditions for scaling microdosimetric sites defined in Section 2.2.1.3, the energy imparted per unit mass is equivalent in the site simulated within the TEPC and in an actual microscopic volume of tissue. This is referred to as the specific energy,  $z$  [ $Gy$ ], as within the simulated microscopic volume the imparted energy is stochastic, unlike the mean quantity of absorbed dose. In experimental microdosimetry a quantity with equal importance to the energy imparted per unit mass is the energy imparted per unit distance, referred to as the lineal energy,  $y$  [ $keV/\mu m$ ]. Lineal energy is similar, but fundamentally different to the concept of LET which is representative of the mean stopping power [34]. Lineal energy is represented using a stochastic probability distribution which characterizes the variations in stopping power as measured for individual events.

Another notable difference is that lineal energy is confined to the energy absorbed within a simulated volume of specified size and geometry. Neither of the two variants of LET is confined to a comparably defined site. The unrestricted LET,  $LET_{\infty}$ , is equivalent to the stopping power as it includes all energy deposited regardless of the distance from the main charged particle track. The restricted LET,  $(-dE/dx)_{\Delta}$ , better approximates the local energy absorption measured for lineal energy, but remains a different quantity. Restricted LET confines energy absorption to a radial distance from the main track that is defined by the range of an electron with the kinetic energy  $\Delta$  [34]. Despite these notable differences lineal energy serves as a good measure of LET, suggesting that the bulk of the energy deposition is local and is not due to delta

rays which stray from the main track. The use of lineal energy as an LET approximate is especially important for determining the dose equivalent, as discussed in Section 2.5.

The most challenging part of measuring the lineal energy is the knowledge of a particles track length through the simulated site. During microdosimetric measurements it is not actually possible to know this, but for microscopic simulated sites the mean track length crossing the gas cavity is a reasonable approximate of the true path length. This mean length crossing the cavity is referred to as the mean chord length,  $\bar{l}$  [ $\mu\text{m}$ ], and is defined as the average length of a straight line randomly intercepting the microscopic simulated site. It is a geometric quantity that can be determined for any convex spheroid by Cauchy's theorem [42]:

$$\bar{l} [\mu\text{m}] = \frac{4V}{S} \quad (2.15)$$

where  $V$  is the volume and  $S$  is the surface area of the simulated tissue site. Cauchy's definition of the mean chord length assumes  $\mu$ -randomness when determining the probability distribution of possible chords through the site. This serves as a good approximation with neutron scattering being very nearly isotropic [43] and  $\mu$ -randomness referring to an isotropic uniform distribution of chord lengths.

This can then be used to calculate lineal energy as the quotient of the energy imparted in a single event,  $\varepsilon_1$  and the mean chord length,  $\bar{l}$ :

$$y [\text{keV}/\mu\text{m}] = \frac{\varepsilon_1}{\bar{l}} \quad (2.16)$$

The following section describes the presentation and interpretation of lineal energy probability distributions.

## 2.4.2 Microdosimetric Distributions

Microdosimetric distributions are generally presented as probability distributions with lineal energy used as the abscissa. A log-linear scale is most appropriate for this as lineal energy values range over four orders of magnitude and generally display the greatest amount of variation within the few decades. The ordinate of the probability distribution varies depending on whether it is the relative event frequency,  $f(y)$ , or relative dose contribution,  $yd(y)$ , that is being presented as a function of lineal energy.

### Redistribution of Lineal Energy Bins

In order to make the area under the curve representative of either the relative event frequency or dose contribution each decade is divided into 50 equal logarithmic intervals, using the analysis presented in Appendix B of ICRU Report 36 [44]. Over the lineal energy range  $0.1 \text{ keV}/\mu\text{m}$  to  $1000 \text{ keV}/\mu\text{m}$  this would be applied as follows:

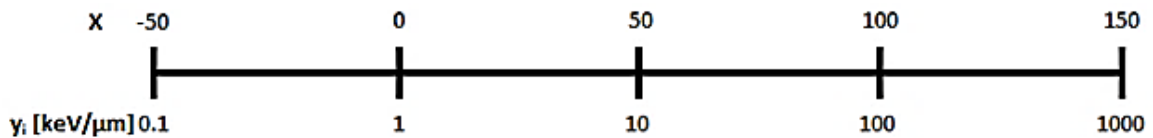


Figure 2.5 – Division of decades into equal sized logarithmic intervals (adapted from [45])

Using the scale in Figure 2.5 the value of bin  $X$  corresponds to lineal energy  $y_i$  is determined as:

$$y_i = 10^{\frac{X}{50}} \quad (2.17)$$

The lineal energy range corresponding to the width of each lineal energy bin,  $d(\ln(y))$ , can then be determined from:

$$\frac{d(\ln(y))}{dy} = \frac{1}{y} \quad (2.18)$$

Where,

$$dy = (y + dy) - y \quad (2.19)$$

which can be offset in order to determine the lineal energy range  $y_{i-\frac{1}{2}}$  to  $y_{i+\frac{1}{2}}$  as:

$$dy = \left[ \left( y_i + \frac{1}{2} \right) - \left( y_i - \frac{1}{2} \right) \right] = 10^{\frac{X+\frac{1}{2}}{50}} - 10^{\frac{X-\frac{1}{2}}{50}}$$

$$dy = 10^{\frac{X}{50}} [10^{\frac{1}{100}} - 10^{-\frac{1}{100}}] \quad (2.20)$$

When the results from Equations 2.17 and 2.20 are substituted into Equation 2.18 this results in:

$$d(\ln(y)) = \frac{10^{\frac{X}{50}} \left[ 10^{\frac{1}{100}} - 10^{-\frac{1}{100}} \right]}{10^{\frac{X}{50}}} = 10^{\frac{1}{100}} - 10^{-\frac{1}{100}}$$

$$d(\ln(y)) = 0.04605 \quad (2.21)$$

When applied to the scale shown in Figure 2.5 the lineal energy bin  $X = -50$  corresponds to the lineal energy range  $0.1 \text{ keV}/\mu\text{m}$  to  $0.14605 \text{ keV}/\mu\text{m}$ , with the following bin  $X = -49$  corresponding to the lineal energy range  $0.14605 \text{ keV}/\mu\text{m}$  up to  $0.1921 \text{ keV}/\mu\text{m}$  and so forth. This lineal energy bin distribution is used for the two main microdosimetric probability distributions.

### Probability Distributions

The most fundamental microdosimetric distribution is the frequency distribution,  $f(y)$ . The frequency distribution is normalized to properly represent the relative event frequency in each lineal energy bin of width  $d(\ln(y))$ . This normalization is achieved by solving the following equation so that the product of the relative event frequency and the logarithmic lineal energy bin width are equal to one:

$$\sum_i f(y_i)d(\ln(y)) = 1 \quad (2.22)$$

Following the sample distribution of lineal energy bins given in Figure 2.5, the normalized value of the frequency distribution in a given logarithmic lineal energy bin,  $f(y_i)_N$ , is determined using:

$$f(y_i)_N = \frac{f(y_i)}{[\sum_{i=-50}^{150} f(y_i)]d(\ln y)} \quad (2.23)$$

However, the frequency distribution tends to make qualitative analysis difficult by obscuring details within the distribution. These details are more easily discernable using the dose distribution, denoted  $d(y) = yf(y)$ . The dose distribution is determined by first normalizing  $d(y)$ :

$$\int_0^{\infty} d(y)dy = 1$$

Which can be expressed on the logarithmic scale using Equation 2.18 as:

$$\int_0^{\infty} yd(y)d(\ln y) = 1 \quad (2.24)$$

The value of  $y_i d(y_i)$  can then be determined as the product of the normalized  $y_i f(y_i)$  distribution and  $y_i$ . These values are now weighted based on the relative dose contribution for events in each lineal energy bin, with the  $yd(y)$  value for a given lineal energy bin,  $y_i$  determined as:

$$y_i d(y_i) = \frac{y_i f(y_i)}{[\sum_{i=-50}^{150} y_i f(y_i)]d(\ln y)} \quad (2.25)$$

## Interpreting Microdosimetric Distributions

Two of the main features of interest in the lineal energy probability distributions are the recoil particle edges. The term 'edge' refers to the maximum lineal energy for a given type of recoil nuclei. In a sphere the proton edge results from a proton having a path-length equal to the counter diameter, with the proton's track ending just as it completes crossing the site. This produces the maximum possible energy deposition by a proton in the given simulated site. Since the factors, such as stopping power, involved in producing this maximum imparted energy are relatively constant between detectors simulating a fixed diameter, the 'edge' position remains relatively consistent at approximately  $100 \text{ keV}/\mu\text{m}$  for a  $2 \mu\text{m}$  diameter simulated site. The stopping powers of the heavy recoil nuclei produced in tissue overlap, producing a single peak for heavy recoil nuclei with an edge at approximately  $500 \text{ keV}/\mu\text{m}$ . This is demonstrated with Table 2.3 which shows the maximum stopping power and ranges for the maximum energy heavy recoil nuclei in a 2.5 MeV neutron field. These maximum recoil nuclei energies were determined by applying the elastic scattering kinematics energy distributions discussed in Section 2.3.1.

Recoil Nuclei	Maximum Energy [MeV]	$(dE/dx)_{\text{total}}$ [keV/ $\mu\text{m}$ ]	Projected Range [ $\mu\text{m}$ ]
C	0.71	515	1.97
N	0.6225	531	1.65
O	0.555	480	1.52

Table 2.3 – Maximum stopping power and ranges for recoil nuclei in unit density A-150 for 2.5 MeV neutrons (data from [37])

As the heavy recoil nuclei depositing the greatest amounts of energy have ranges shorter than the  $2 \mu\text{m}$  counter diameter they deposit their entire energy within the counter. This causes

larger variations between the lineal energies for the heavy recoil edge between counters and neutron energies.

The ability to more easily discern features by using the dose distribution is demonstrated with Figure 2.6. This directly compares the dose and frequency distributions determined using the same simulated exposure data. The ‘edges’ produced by recoil nuclei are labelled in Figure 2.6 to demonstrate that while they appear washed out in the frequency distribution, they are easily discernable in the dose distribution.

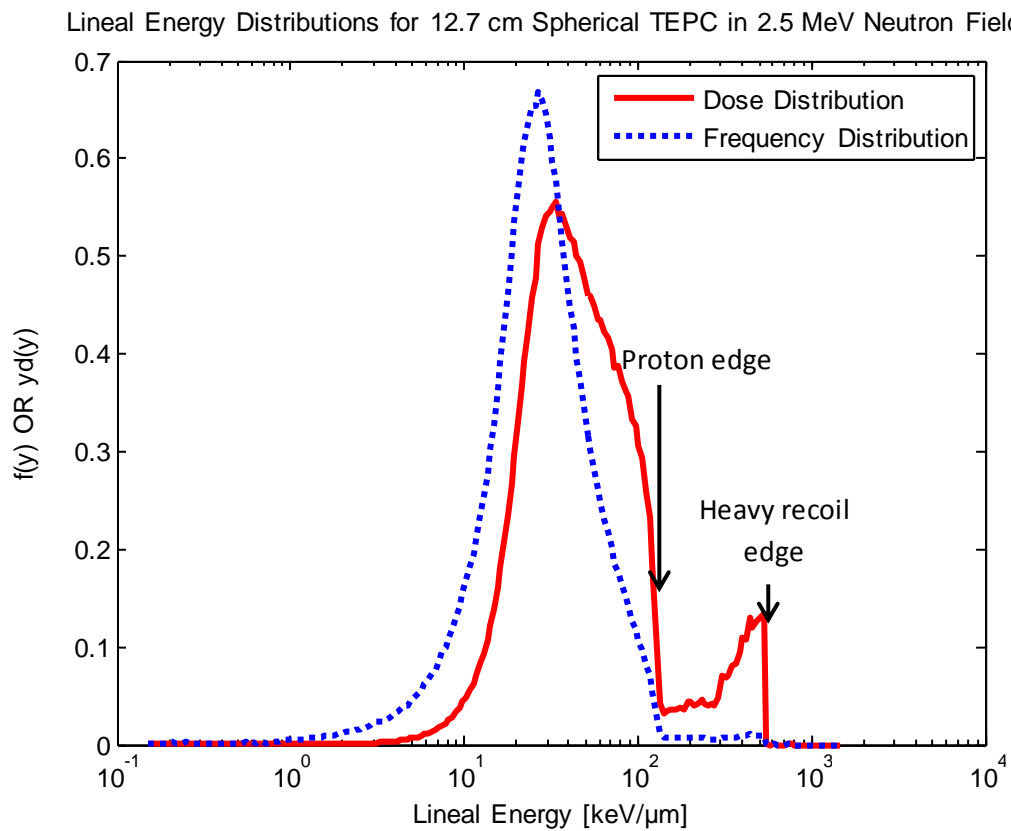


Figure 2.6 – Frequency and dose distributions simulated in PHITS for 2  $\mu$ m diameter simulated site using  $2 \times 10^9$  neutrons

The dose distribution also accentuates the fairly significant dose contributions from the relatively few events that occur at the high lineal energies approaching the heavy recoil edge.

### 2.4.3 Moments of the Microdosimetric Distributions

While the distributions contain all measurement information, the mean quality of radiation fields can be characterized by the first and second microdosimetric moments. These moments are the frequency mean and dose mean lineal energies, respectively.

The frequency mean lineal energy is not the most frequently occurring lineal energy, but the overall average lineal energy that events occur at, determined as:

$$\bar{y}_F = \frac{\sum_{i=0}^{\infty} y_i * f(y_i)}{\sum_{i=0}^{\infty} f(y_i)} \quad (2.26)$$

where  $f(y_i)$  is the probability of an event occurring with lineal energy  $y_i$ .

The dose mean lineal energy determines the mean of the  $d(y)$  distribution, which contains the relative dose contribution of each lineal energy bin, calculated as:

$$\bar{y}_D = \frac{\sum_{i=0}^{\infty} y_i * d(y_i)}{\sum_{i=0}^{\infty} d(y_i)} \quad (2.27)$$

In addition to characterizing the quality of radiation fields, these moments are useful as response metrics for evaluating detector performance.

## 2.5 Determining Operational Quantities

While microdosimetric distributions and moments are suitable for monitoring the quality of radiation fields, ultimately it is the operational quantities that are required for radiation protection applications. The operational quantity specific to neutron and gamma radiation is the ambient dose equivalent,  $H^*(10)$ . Definitions and the method currently used for determining  $H^*(10)$  in reactor neutron fields have been reviewed in Sections 1.2-1.3. This section serves to present the method for obtaining the operational quantities from experimental microdosimetric measurements.

The stochastic microdosimetric quantity of specific energy must first be converted to the mean radiation protection quantity of absorbed dose. Specific energy is the quotient of the energy imparted in the gas by any number of events,  $\varepsilon$  and the mass of gas,  $m$ :

$$z = \frac{\varepsilon}{m} \quad (2.28)$$

By increasing the number of events the variation between specific energy measurements decreases. Eventually the variations are small enough to be considered negligible, at which point it is the absorbed dose that is measured.

$$D = \bar{z} \quad (2.29)$$

The absorbed dose is calculated from a microdosimetric measurement as:

$$D = \frac{\varepsilon_{total}}{m_{gas}} = \bar{l} * \frac{\sum_{i=0}^{\infty} y_i * f(y_i)}{\rho_{gas} * V_{gas}} \quad (2.30)$$

where  $\varepsilon_{total}$  is the total energy imparted, and  $m_{gas}$ ,  $\rho_{gas}$ , and  $V_{gas}$  are representative of the mass, density and volume of the gas respectively.

With the absorbed dose determined, the applicable radiation quality factor must then be calculated. For this, the mean quality factor,  $\bar{Q}$ , is used and its evaluation is based on the  $d(y)$  distribution and the ICRP 60 [5] definition of the quality factor as a function of LET. With lineal used as an LET approximate this calculation is expressed as:

$$\bar{Q} = \frac{\sum Q(y_i)d(y_i)}{\sum d(y_i)} \quad (2.31)$$

where  $Q(y_i)$  is the quality factor applicable to lineal energy  $y_i$ , as determined using the following piecewise function from ICRP 60 [5], which is also shown in Figure 2.7.

$$Q(y) = \begin{cases} 1 & y < 10 \frac{\text{keV}}{\mu\text{m}} \\ 0.32y - 2.2 & 10 \frac{\text{keV}}{\mu\text{m}} < y < 100 \frac{\text{keV}}{\mu\text{m}} \\ \frac{300}{\sqrt{y}} & y > 100 \frac{\text{keV}}{\mu\text{m}} \end{cases}$$

The quality factor varies as a function of lineal energy or LET due to the variations in Relative Biological Effectiveness (RBE) resulting from variations in ionization density. The lineal energy with the highest RBE, that is the most damaging, is  $100 \text{ keV}/\mu\text{m}$ . At this lineal energy the mean distance between ionizations corresponds with the spacing between the two DNA strands, making it the most effective at producing double strand breaks. Double strand breaks are significantly more difficult to repair than single strand breaks since the opposite DNA strand cannot be used as a template, making errors much more likely to occur during DNA repair. Double strand break production is less probable for lower lineal energies, and when deposited at higher lineal energies the relative damage to DNA per unit dose is decreased.

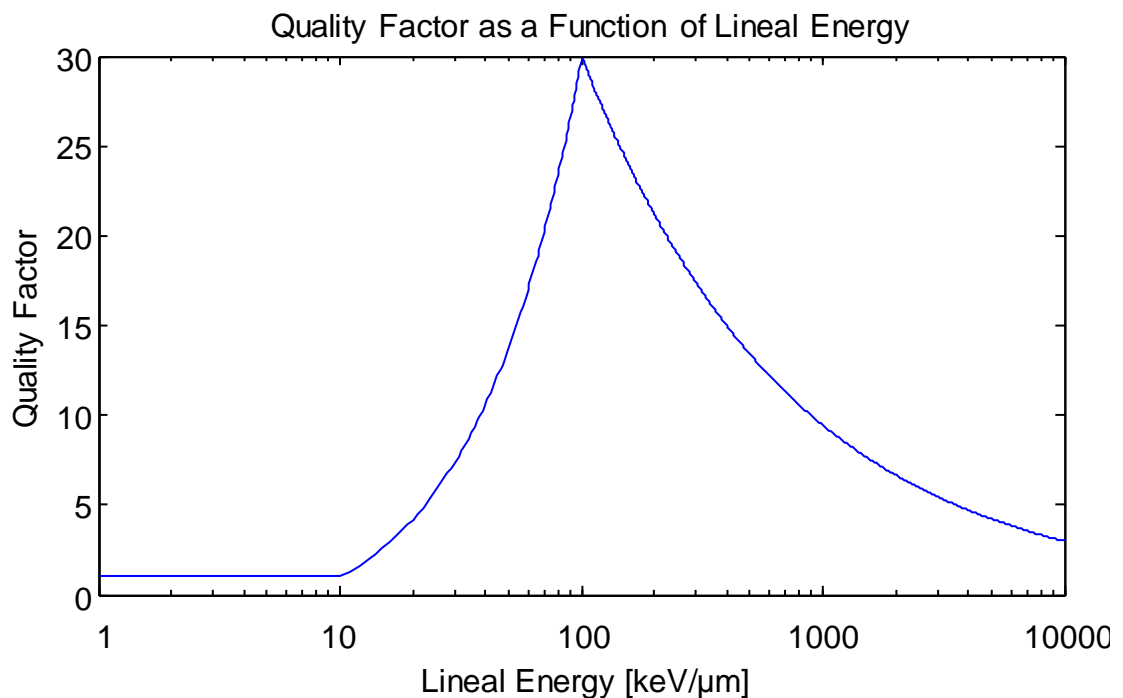


Figure 2.7 – Quality factor as a function of lineal energy, based on ICRP 60 [5]

The dose equivalent,  $H$ , can then be determined as the product of the total absorbed dose and the mean quality factor during this exposure:

$$H = D \bar{Q} \quad (2.32)$$

This measurement of dose equivalent is used as an approximate measure of the ambient dose equivalent,  $H^*(10)$ :

$$H \cong H^*(10) \quad (2.33)$$

The microdosimetric and operational quantities are not precisely the same as TEPCs and the 30 cm diameter ICRU sphere have different dimensions, but since TEPCs function as a Bragg-Gray cavity chambers and have the same elemental composition they serve as good surrogates. In order to evaluate instrument response in well-defined neutron or photon fields the measured or simulated  $H$  values can be compared to the index  $H^*(10)$  values presented in ICRP 74 [10].

## 2.6 Error in Microdosimetric and Operational Quantities

When calculating the standard deviation values for the microdosimetric and operational quantities the counting statistics associated with experimental microdosimetric measurements and simulations must be taken into account. This requires the application of error propagation as presented by Knoll [41] since all of the derived microdosimetric quantities involve summations of count frequency, thus requiring error analysis beyond the error in the number of counts:

$$\sigma(f(y_i)) = \sqrt{f(y_i)} \quad (2.34)$$

where  $\sigma$  is the standard deviation and  $f(y_i)$  may represent either counts or the normalized count frequency in the lineal energy bin  $y_i$ .

## Frequency Mean Lineal Energy

The  $\bar{y}_F$  (Equation 2.26) is the quotient of two summations which both include counts,  $\sum y_i f(y_i)$  and  $\sum f(y_i)$ . In order to determine the overall standard deviation, the standard deviations for both the numerator and denominator of  $\bar{y}_F$  must first be determined. Using the error analysis rule for sums of counts [41] along with Equation 2.34 the standard deviation in the denominator is:

$$\begin{aligned}\sigma\left(\sum_{i=1}^N f(y_i)\right) &= \sqrt{[\sigma(f(y_1))]^2 + [\sigma(f(y_2))]^2 \cdots [\sigma(f(y_N))]^2} \\ &= \sqrt{[\sqrt{f(y_1)}]^2 + [\sqrt{f(y_2)}]^2 \cdots [\sqrt{f(y_N)}]^2} \\ &= \sqrt{f(y_1) + f(y_2) \cdots f(y_N)}\end{aligned}$$

This can then be written in the form of a summation:

$$\sigma\left(\sum_{i=1}^N f(y_i)\right) = \sqrt{\sum_{i=1}^N f(y_i)} \quad (2.35)$$

The summation in the numerator of  $\bar{y}_F$  is similar, with an additional constant term,  $y_i$ . Given there is no error associated with the constant,  $y_i$ , the error in the number of counts multiplied by a constant is:

$$\sigma(y_i f(y_i)) = y_i \sigma(f(y_i)) = y_i \sqrt{f(y_i)} \quad (2.36)$$

This can be applied to determine the standard deviation for the numerator of  $\bar{y}_F$  as follows:

$$\begin{aligned}\sigma\left(\sum_{i=1}^N y_i f(y_i)\right) &= \sqrt{[\sigma(y_1 f(y_1))]^2 + [\sigma(y_2 f(y_2))]^2 \cdots [\sigma(y_N f(y_N))]^2} \\ &= \sqrt{[y_1 \sqrt{f(y_1)}]^2 + [y_2 \sqrt{f(y_2)}]^2 \cdots [y_N \sqrt{f(y_N)}]^2}\end{aligned} \quad (2.37)$$

This can then be expressed in the form of a summation:

$$\sigma\left(\sum_{i=1}^N y_i f(y_i)\right) = \sqrt{\sum_{i=1}^N y_i^2 f(y_i)} \quad (2.38)$$

The overall standard deviation for  $\bar{y}_F$  is then determined using the rule for division of counts

[41]:

$$\begin{aligned} \left(\frac{\sigma(\bar{y}_F)}{\bar{y}_F}\right)^2 &= \left(\frac{\sigma(\sum y_i f(y_i))}{\sum y_i f(y_i)}\right)^2 + \left(\frac{\sigma(\sum f(y_i))}{\sum f(y_i)}\right)^2 \\ \sigma(\bar{y}_F) &= \bar{y}_F \sqrt{\left(\frac{\sigma(\sum y_i f(y_i))}{\sum y_i f(y_i)}\right)^2 + \left(\frac{\sigma(\sum f(y_i))}{\sum f(y_i)}\right)^2} \end{aligned} \quad (2.39)$$

Where the results from Equations 2.35 and 2.38 are substituted into Equation 2.39 resulting in:

$$\begin{aligned} \sigma(\bar{y}_F) &= \bar{y}_F \sqrt{\left(\frac{\sqrt{\sum y_i^2 f(y_i)}}{\sum y_i f(y_i)}\right)^2 + \left(\frac{\sqrt{\sum f(y_i)}}{\sum f(y_i)}\right)^2} \\ \sigma(\bar{y}_F) &= \bar{y}_F \sqrt{\frac{\sum y_i^2 f(y_i)}{[\sum y_i f(y_i)]^2} + \frac{\sum f(y_i)}{[\sum f(y_i)]^2}} \\ \sigma(\bar{y}_F) &= \bar{y}_F \sqrt{\frac{\sum y_i^2 f(y_i)}{[\sum y_i f(y_i)]^2} + \frac{1}{\sum f(y_i)}} \end{aligned} \quad (2.40)$$

### Dose Mean Lineal Energy

The  $\bar{y}_D$  (Equation 2.27) is defined as the quotient of  $\sum y_i^2 f(y_i)$  and  $\sum y_i f(y_i)$ , where the standard deviation defined in Equation 2.38 can be applied again for the denominator.

Similar to the derivation of Equation 2.38 it is assumed that there is no error is associated with

the constant term,  $y_i^2$ , when determining the standard deviation for the numerator of  $\bar{y}_D$ .

Following steps similar to those presented in Equation 2.37 the error for the numerator is determined as:

$$\begin{aligned}\sigma\left(\sum_{i=1}^N y_i d(y_i)\right) &= \sigma\left(\sum_{i=1}^N y_i^2 f(y_i)\right) \\ &= \sqrt{\sum_{i=1}^N y_i^4 f(y_i)}\end{aligned}\quad (2.41)$$

With quotient rule for the  $\bar{y}_D$  resulting in:

$$\left(\frac{\sigma(\bar{y}_D)}{\bar{y}_D}\right)^2 = \left(\frac{\sigma(\sum y_i^2 f(y_i))}{\sum y_i^2 f(y_i)}\right)^2 + \left(\frac{\sigma(\sum y_i f(y_i))}{\sum y_i f(y_i)}\right)^2$$

This can be solved with the substitution of the results from Equations 2.38 and 2.41:

$$\begin{aligned}\sigma(\bar{y}_D) &= \bar{y}_D \sqrt{\left(\frac{\sqrt{\sum y_i^4 f(y_i)}}{\sum y_i^2 f(y_i)}\right)^2 + \left(\frac{\sqrt{\sum y_i^2 f(y_i)}}{\sum y_i f(y_i)}\right)^2} \\ \sigma(\bar{y}_D) &= \bar{y}_D \sqrt{\frac{\sum y_i^4 f(y_i)}{[\sum y_i^2 f(y_i)]^2} + \frac{\sum y_i^2 f(y_i)}{[\sum y_i f(y_i)]^2}}\end{aligned}\quad (2.42)$$

### Dose per Unit Fluence

The dose per unit fluence is calculated as:

$$\frac{D}{\varphi} = \left(\frac{1.60218 \times 10^{-16} \frac{J}{KeV}}{m_{gas} \varphi}\right) \sum_{i=1}^N y_i f(y_i)\quad (2.43)$$

The associated standard deviation of  $D/\varphi$  is then determined by applying the result from Equation 2.38, which is not affected by the constant terms outside of the summation:

$$\sigma\left(\frac{D}{\phi}\right) = \left(\frac{1.60218 \times 10^{-16} \frac{J}{KeV}}{m_{gas}\phi}\right) \sqrt{\sum_{i=1}^N y_i^2 f(y_i)} \quad (2.44)$$

### Mean Quality Factor

As the mean quality factor,  $\bar{Q}$  (defined by Equation 2.31) is the quotient of two summations,  $\sum Q(y_i)y_i f(y_i)$  and  $\sum y_i f(y_i)$ , which both include counts. As such the associated standard deviation of  $\bar{Q}$  requires the quotient rule:

$$\left(\frac{\sigma(\bar{Q})}{\bar{Q}}\right)^2 = \left(\frac{\sigma(\sum Q(y_i)y_i f(y_i))}{\sum Q(y_i)y_i f(y_i)}\right)^2 + \left(\frac{\sigma(\sum y_i f(y_i))}{\sum y_i f(y_i)}\right)^2 \quad (2.45)$$

Where the terms  $Q(y_i)y_i$  are constant, allowing the application of the error analysis similar to Equation 2.38, making the numerator of the first term of Equation 2.45 equal to:

$$\begin{aligned} \sigma\left(\sum_{i=1}^N Q(y_i)y_i f(y_i)\right) &= \sqrt{\sum_{i=1}^N (Q(y_i)y_i \sigma(f(y_i)))^2} \\ &= \sqrt{\sum_{i=1}^N Q(y_i)^2 y_i^2 f(y_i)} \end{aligned} \quad (2.46)$$

Using Equation 2.46 along with Equation 2.38 the standard deviation of  $\bar{Q}$  is found to be:

$$\begin{aligned} \sigma(\bar{Q}) &= \bar{Q} \sqrt{\left(\frac{\sqrt{\sum Q(y_i)^2 y_i^2 f(y_i)}}{\sum Q(y_i)y_i f(y_i)}\right)^2 + \left(\frac{\sqrt{\sum y_i^2 f(y_i)}}{\sum y_i f(y_i)}\right)^2} \\ \sigma(\bar{Q}) &= \bar{Q} \sqrt{\frac{\sum Q(y_i)^2 y_i^2 f(y_i)}{[\sum Q(y_i)y_i f(y_i)]^2} + \frac{\sum y_i^2 f(y_i)}{[\sum y_i f(y_i)]^2}} \end{aligned} \quad (2.48)$$

### Dose Equivalent per Unit Fluence

As the dose equivalent per unit fluence is the product of  $D/\varphi$  and  $\bar{Q}$  its standard deviation is determined using the product rule [41], which includes the error in both of these quantities as stated Equations 2.44 and 2.48, respectively:

$$\sigma\left(\frac{H}{\varphi}\right) = \frac{H}{\varphi} \sqrt{\left(\frac{\sigma(\bar{Q})}{\bar{Q}}\right)^2 + \left(\frac{\sigma\left(\frac{D}{\varphi}\right)}{\frac{D}{\varphi}}\right)^2} \quad (2.49)$$

### Sensitivity

An additional quantity which will be evaluated in Chapter 5 is the sensitivity,  $s$  which is defined as the total counts,  $c = \sum_{i=1}^N f(y_i)$ , per unit dose equivalent [*counts/Sv*]:

$$s = \frac{c}{H} \quad (2.50)$$

Similar to Equation 2.34 the standard deviation of the total number of counts is simply:

$$\sigma(c) = \sqrt{c} \quad (2.51)$$

This standard deviation in the sensitivity is then found by applying the quotient rule [41] for division of counts:

$$\begin{aligned} \sigma(s) &= s \sqrt{\left(\frac{\sigma(c)}{c}\right)^2 + \left(\frac{\sigma(H)}{H}\right)^2} \\ \sigma(s) &= s \sqrt{\frac{c}{c^2} + \frac{\sigma(H)^2}{H^2}} \end{aligned} \quad (2.52)$$

Where there is no error associated with the fluence, making  $\sigma(H)$  equal to the product of  $\sigma\left(\frac{H}{\varphi}\right)$ , as shown in Equation 2.49, and the fluence,  $\varphi$ .

## Chapter 3: Detectors in Microdosimetry

### 3.1 Introduction

Various types of TEPCs have been designed to address the needs specific to a variety of radiation fields and applications. The primary factors in determining on the appropriate detector are the radiation type and energy spectrum as this makes it possible to conclude whether the conditions for CPE are fulfilled. Following this, practical factors including the detectors sensitivity, size, weight, and robustness may be considered. The main TEPC variations include single element walled and wall-less counters, as well as multi-element counters. As it is only the single and multi-element walled counters that are appropriate for neutron dosimetry, this discussion omits the wall-less counters used for charged particle dosimetry. Following a review of both traditional and conceptual walled TEPC and METEPC designs, the design process and specifications for a novel hemispherical METEPC element will be presented. The chapter will then be concluded with an analysis of the effects of detector geometry on measurements.

### 3.2 Variations of TEPCs

#### 3.2.1 Rossi Counters and Single Wire TEPCs

The commercially available TEPCs consist of a plastic TE spherical shell filled with TE gas. The spherical geometry is used largely for its near isotropic performance, which is only marginally compromised by the small cylindrical region of gas gain contiguous with the central anode wire [46]. The means used for defining this region of gas gain is what distinguishes the Rossi and Single Wire counters.

Shown on the left of Figure 3.1 is the Rossi counter, the original TEPC design from the 1950s, which uses a helix positioned concentric to the anode wire to physically define the avalanche region [47]. This works by applying 20% of the anode potential to the helix, creating a

strong electric field and restricting all gas gain to the cylindrical volume defined by the helix [48]. The electric field outside the helix is only strong enough to cause electrons to drift towards the anode. Although this works well, the process of manually winding a wire into a helix and installing it with precision into the detector takes a great deal of time and expertise.

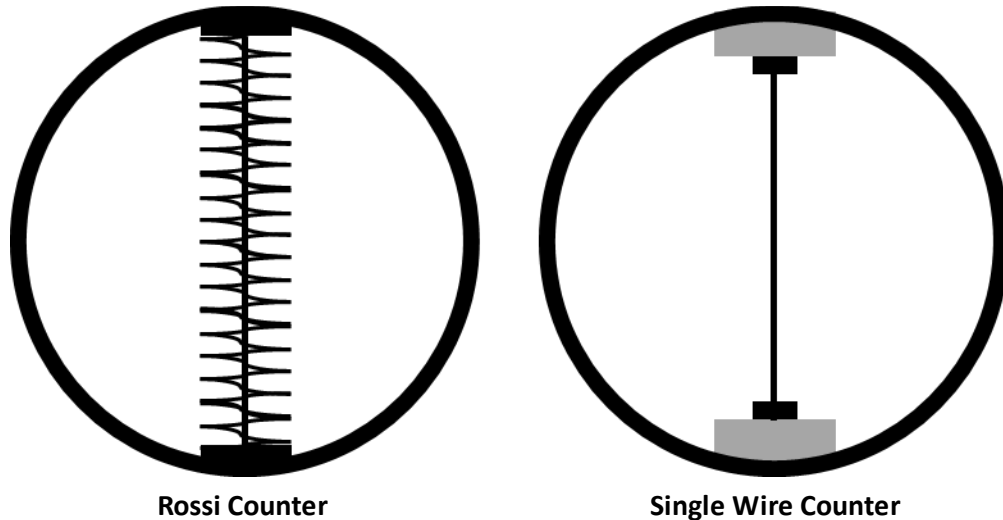


Figure 3.1 – Schematic of Rossi and Single wire counters, with conductive materials shown in black and insulating materials shown in grey (not to scale)

These challenges during the manufacturing of Rossi counters likely motivated the simplified design of the Single Wire counter shown on the right of Figure 3.1. The Single Wire counter uses field shaping electrodes at each end of the anode wire in order to make the electric field strength uniform where it would otherwise increase. This produces a relatively uniform electric field distribution over the entire anode wire and has benefits beyond simplifying detector assembly. The use of fixed electrodes in place of the helix slightly reduces microphonic noise caused by vibrations of either the helix or anode wire. These vibrations can occur when the detector is moved, from acoustic sounds, or even something as subtle as walking past a detector.

The simulations conducted in this work used the commercial single wire spherical TEPC model LET-SW5 (Far West, Goleta, CA) illustrated in Figure 3.2 as the reference TEPC. This TEPC

is based upon the experimentally optimized proportional counter design of P.W. Benjamin and associates [49].

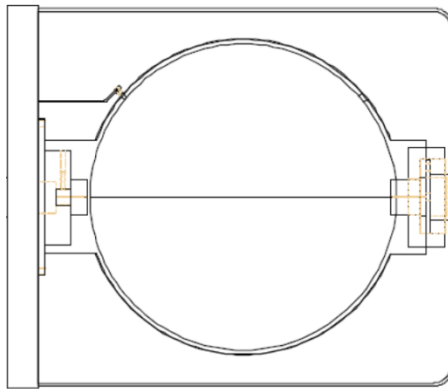


Figure 3.2 – Far West model LET-SW5, 12.7 cm diameter (adapted from [50])

### 3.2.2 Cylindrical TEPCs

The cylinder is the least complex of the current TEPC designs. This is largely due to the fact that machining a cylindrical shell is straightforward relative to the formation of a sphere, which generally requires moulding. The downside of the cylindrical design is the non-isotropic response that stems from the detectors directionally dependent physical cross section.

Simulations using planar neutron fields have reported that the detector-source orientation affects detector sensitivity and the patterns of energy deposition [51]. Although directional dependence can be minimized with the use of a right circular cylinder where the diameter and height are equal, this generally results in more severe end effects when compared to elongated cylinders.

End effects are caused by the decreased distance between the anode and cathode near the ends of the wire producing stronger electric fields and increasing the local gas gain. In areas away from the ends of the wire the symmetry of the concentric cylindrical anode and cathode creates an ideal electric field distribution. This means that the greater the elongation of a cylinder, where elongation is the quotient of height and diameter, the larger this region of symmetry is and the less end effects disturb gas gain. However, since directional dependence

also increases with elongation, attempts are made to shape the electric field distribution and reduce end effects.

One method of field shaping is by using field tubes to surround and shield the ends of the anode. This is done by having the outer radius of the field tube maintain the potential that would exist at that radius if the cylinder were infinitely long [52]. This works well at producing a uniform electric field, but as it is recommended that field tubes extend from each end with a length equal to the radius of the cylinder [52]; they reduce the effective sensitive volume as electrons collected by a field tube do not contribute to the measured signal. Alternatively, anode extensions similar to those used in spherical counters can achieve near electric field uniformity by enlarging the effective anode diameter at each end of the wire. As the electric field distribution and uniformity are dependent on the specific detector geometry, the appropriate dimensions of radius and length for anode extension must be optimized for the specific detector in order for them to effectively produce a uniform electric field. An example of an experimentally validated anode extension design where the anode extension remains electrically connected to the anode wire is shown in Figure 3.3 [53].

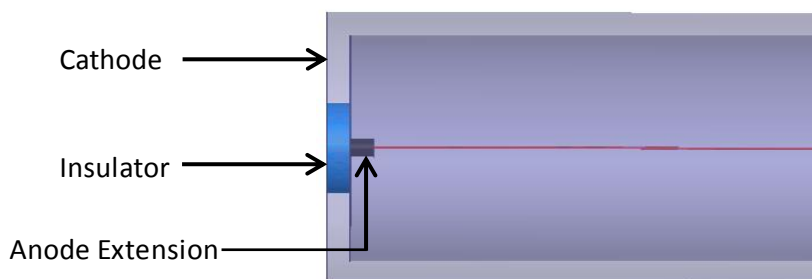


Figure 3.3 – Illustration of the 0.02 *cm* diameter by 0.05 *cm* length anode extension as used in the 0.5 *cm* by 5 *cm* cylindrical METEPC element described in [53, 54]

This example is from a cylindrical METEPC element which is included in the comparative performance analysis as discussed in Section 3.4.3.1.

### 3.2.3 METEPCs

METEPCs originated from an effort to decrease the detector size required for achieving adequate sensitivity in the low intensity neutron fields encountered in radiation protection [18]. This works as the sensitivity of a counter is proportional to the cavities surface area and the mass of gas [51, 53]. METEPCs sum the signals produced by a cluster of small independent counters, increasing both the surface area and mass of gas per unit volume relative to a single element counter of comparable sensitivity [51].

Harald Rossi first proposed and tested the concept of an METEPC in the 1980s by constructing the counter shown in Figure 3.4. This counter incorporates 296 cylindrical elements, each with dimensions of 0.3175 *cm* height by 0.3175 *cm* diameter and has no field shaping electrodes [18]. This initial design was oversimplified and exhibited strong end effects that resulted in poor energy resolution. This was vastly improved with the addition of TE disks in the end walls of each cylinder, serving the same purpose as field tubes [55]. Similar to field tubes this reduced the effective sensitive volume, but it did dramatically increase the energy resolution [55]. However, this modification increased the complexity of an already intricate counter. Manufacturing this METEPC required 1295 various sized holes to be drilled, hundreds of electrical connections to be established for each anode wire and TE disk, all while maintaining careful alignment of the entire structure to establish electric field uniformity [55]. This design successfully demonstrated the METEPC concept, but the complexity limited its use.

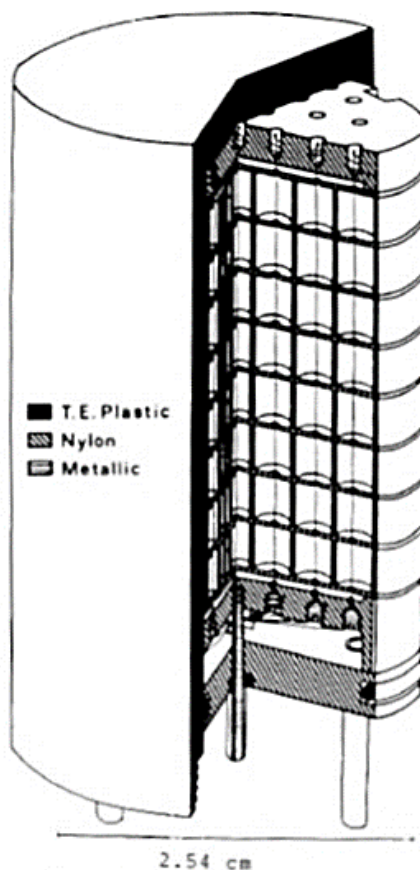


Figure 3.4 – Illustration of the original 296 element METEPC prototype [55]

As it was later established that the sensitivity [*counts/Sv*] of a 12.7 *cm* diameter single element detector was adequate for radiation protection applications [3], later METEPC designs have used this as a benchmark [51, 54]. The 61 element METEPC constructed by Waker and Aslam matched this sensitivity with a counter that is only 11% of the volume of the reference spherical TEPC [53]. The elements of this METEPC were elongated cylinders, with dimensions of 0.5 *cm* diameter and 5 *cm* length, shown to the right of the reference spherical TEPC in Figure 3.5. Each element employs anode extensions as shown in Figure 3.3 to minimize end effects without compromising sensitivity [54]. Although measurements taken in isotropic fields do agree favorably with the reference spherical TEPC [54], simulations show that in planar neutron fields the elongated cylinders exhibit directional dependence [51].

Recent work on the design of next generation METEPCs presented by Ali [51] included energy deposition simulations using a variety of neutron fields incident on the reference spherical TEPC, the METEPC of Waker and Aslam [53, 54], and two novel METEPC designs which are all shown in Figure 3.5. The novel conceptual designs by Ali [51] are the CMETEPC and QITEPC, which contain 113 cylindrical and 392 spherical elements, respectively.

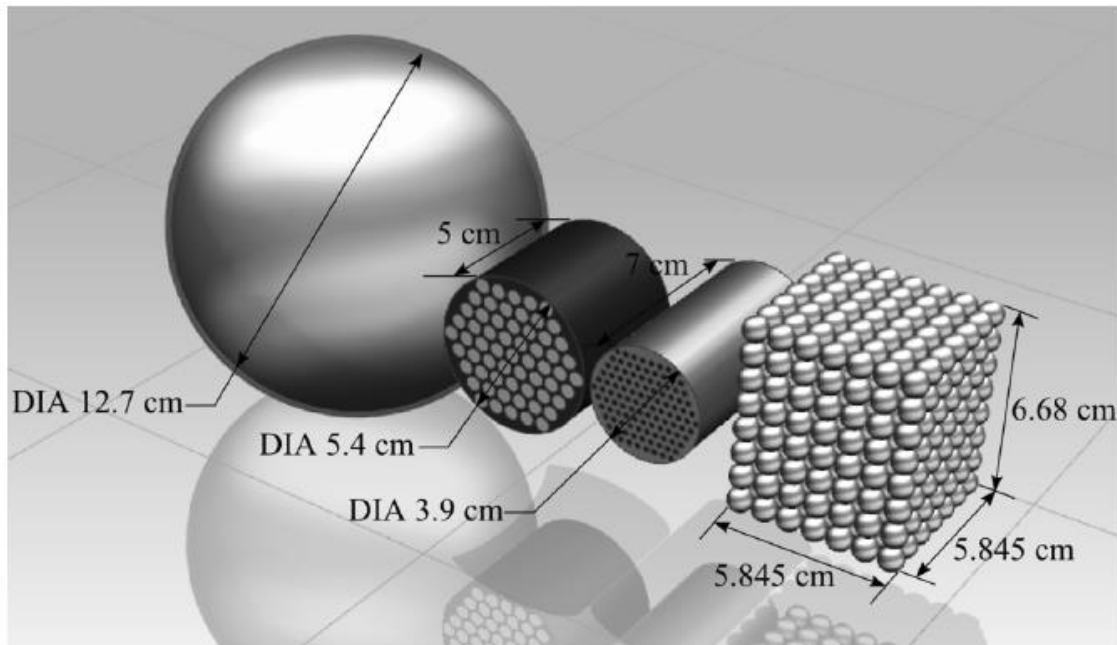


Figure 3.5 – Illustration of TEPC Instruments, From Left to Right: Standard 12.7 TEPC Design, METEPC, CMETEPC, and QITEPC [51]

The cylindrical elements of the CMETEPC designed by Ali have dimensions of  $0.2\text{ cm}$  diameter and  $7\text{ cm}$  length, and the spherical elements of his QITEPC are each  $0.635\text{ cm}$  in diameter. The total volumes for the CMETEPC and QITEPC are only 7% and 19% of the volume of the  $12.7\text{ cm}$  diameter spherical TEPC. Similar to the cylindrical METEPC of Waker and Aslam, simulations show directional dependence for the CMETEPC, whereas the QITEPC displays isotropic performance. The electrostatics of these conceptual METEPC designs were not evaluated; however, considering the construction of the METEPC by Rossi the logistics involved in

fabricating such intricate counters is not trivial. This is one of the reasons an alternative type of METEPC element is currently being pursued.

### **3.4 Design Concept for a Wire-less TEPC**

#### **3.4.1 Potential Improvements of TEPC and METEPC Element Designs**

While it has been established that many of the past and present TEPC and METEPC designs do work, they remain complex and leave some practical qualities to be desired. The following lists some specific issues which could be improved upon:

- Wired proportional counters are sensitive to microphonic noise
- Current detector geometries exhibit varying degrees of the end effect due to electric field non-uniformities occurring at the ends of the anode wire
- METEPC construction remains impractical, in large part due to there being no simple procedure for anode wire installation

It is hypothesized that a non-wired counter using an alternative geometry may be a solution to at least some of these issues. The thought process behind this idea and the development of the new design will now be presented.

#### **3.4.2 Initial Study of Electric Field Distributions**

The counter design using a wire-less anode developed from a progressive series of electric field analyses in ANSYS Maxwell V.14.0, which iteratively solves the Maxwell equation in two dimensions for the input geometry and potentials from the user. More specific details regarding functionality of the ANSYS Maxwell software are provided in Section 4.1.

The initial set of electrostatic analyses in Maxwell was qualitatively analyzed for electric field uniformity, with the areas immediately surrounding the anode being the most important.

The initial designs which were simulated used cathode walls similar to those of existing TEPCs with alternative types of anodes. Two examples taken from these initial designs, shown in Figure 3.6 (a) and (b), are a right cylinder with a cylindrical anode up to the center of the cavity and a sphere with a concentric ball on a wire.

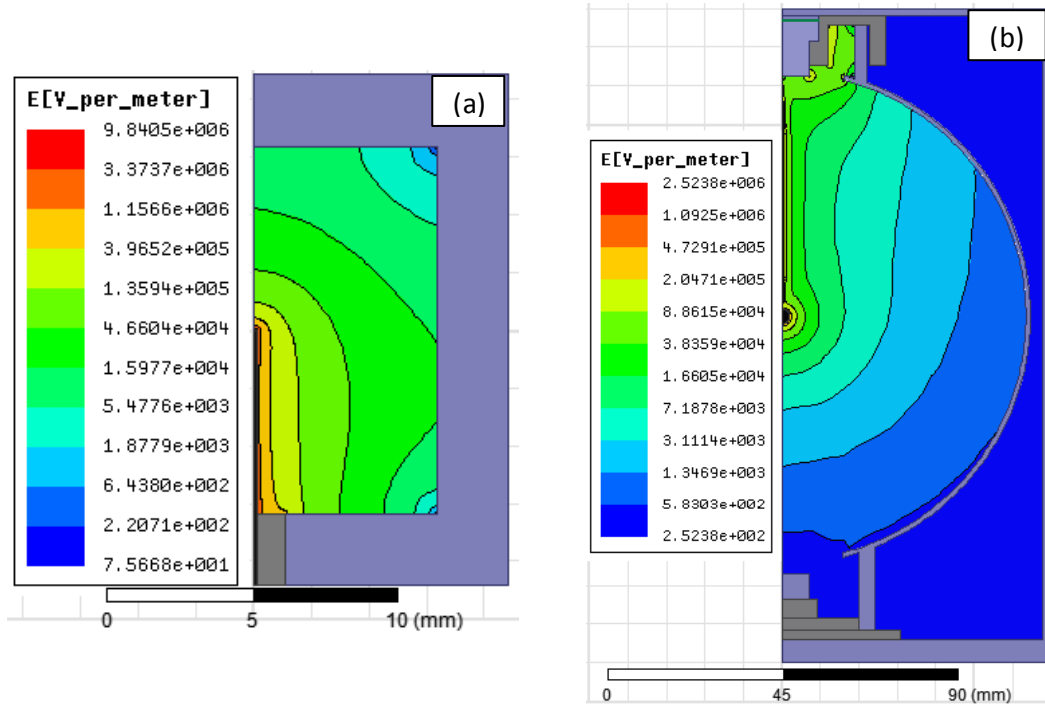


Figure 3.6 – 2D Electric field equipotential distributions in +ZX plane  
 (a) 0.635 *cm* by 0.635 *cm* Right Cylinder with a 0.2 *mm* diameter anode at 700 V;  
 (b) 12.7 *cm* diameter sphere with concentric 2 *mm* diameter ball anode suspended from 70  $\mu$ m diameter anode at 700 V

Both of these counters exhibit electric field non-uniformities in the area immediately surrounding the anode which would be expected to produce non-uniform gas gain. However the lower hemisphere of the spherical counter in Figure 3.6(b) appears to have an ideal electric field distribution as there is no interference from the anode wire. It was hypothesized that by limiting the gas cavity to the lower hemisphere of this design electric field uniformity could be achieved throughout the entire gas cavity.

### 3.4.3 Optimization of the Hemisphere Design

Following the decision to pursue the hemispherical design the proportions of the various components were determined. A 0.4 *mm* diameter anode ball was chosen as it was the smallest commercially available electrically conductive ball brazed onto a metal stem (available from Baltec™, LA, California), and anode size is inversely proportional to electric field strength. An investigation was then required to determine the appropriate cathode and insulator proportions for this anode. Throughout the analysis of the hemisphere high voltages of 750 V and 0 V were used for the anode and cathode, respectively. This was for consistency with currently used TEPC equipment; however, in practice the anode voltage would be adjusted to fine-tune the gain.

The appropriate cathode diameter was determined following a series of analyses for hemispheres ranging from 1.27 *cm* to 12.7 *cm*. Throughout these analyses the radius of the insulator ring surrounding the anode (example shown in Figure 3.10) was scaled to maintain a consistent ratio of insulator radius to cathode diameter. As the cathode size was found to be inversely proportional to electric field strength the potential hemisphere diameters were limited to 1.27 *cm* or 2.54 *cm* which produced the highest magnitude electric field. A series of six radial insulator radii were then simulated and analyzed for both of the cathode diameters, and results of these analyses are presented in Figures 3.7, 3.8, and 3.9 and are summarized in Table 3.1.

Throughout the analyses the gas pressure was determined for a simulated site of 2  $\mu\text{m}$ . For the hemispheres it was the radius which was defined as 2  $\mu\text{m}$ , whereas for the sphere the diameter was defined as 2  $\mu\text{m}$ . This made the mean chord lengths of the hemisphere and sphere more closely resemble one another as they are equal to  $\frac{8}{9} * \text{radius}$  and  $\frac{2}{3} * \text{diameter}$ , respectively.

Detector type and diameter (anode diameter)	Insulator radius [mm]	Max electric field [V/m]	Pressure [torr] for simulating $r = 2 \mu m$	Reduced electric field [V/m * torr]
<b>Hemisphere</b> <b>1.27 cm</b> (0.4 mm)	6.55	$2.72 * 10^6$	133.42	$2.04 * 10^4$
	4.9	$3.31 * 10^6$	133.42	$2.48 * 10^4$
	4.2	$3.91 * 10^6$	133.42	$2.93 * 10^4$
	3.2	$4.08 * 10^6$	133.42	$3.06 * 10^4$
	2.2	$4.60 * 10^6$	133.42	$3.45 * 10^4$
	1.2	$6.51 * 10^6$	133.42	$4.88 * 10^4$
<b>Hemisphere</b> <b>2.54 cm</b> (0.4 mm)	12.9	$2.68 * 10^6$	66.71	$4.02 * 10^4$
	9.6	$2.78 * 10^6$	66.71	$4.17 * 10^4$
	8.2	$3.18 * 10^6$	66.71	$4.77 * 10^4$
	6.2	$4.17 * 10^6$	66.71	$6.26 * 10^4$
	4.2	$4.00 * 10^6$	66.71	$6.00 * 10^4$
	2.2	$5.19 * 10^6$	66.71	$7.78 * 10^4$
<b>Sphere</b> <b>12.7 cm</b> (70 $\mu m$ )	-	$2.72 * 10^6$	6.67 (for $d = 2 \mu m$ )	$4.03 * 10^5$

Table 3.1 – Analysis of the effects of insulator radius and counter size on the magnitude of electric and reduced electric fields

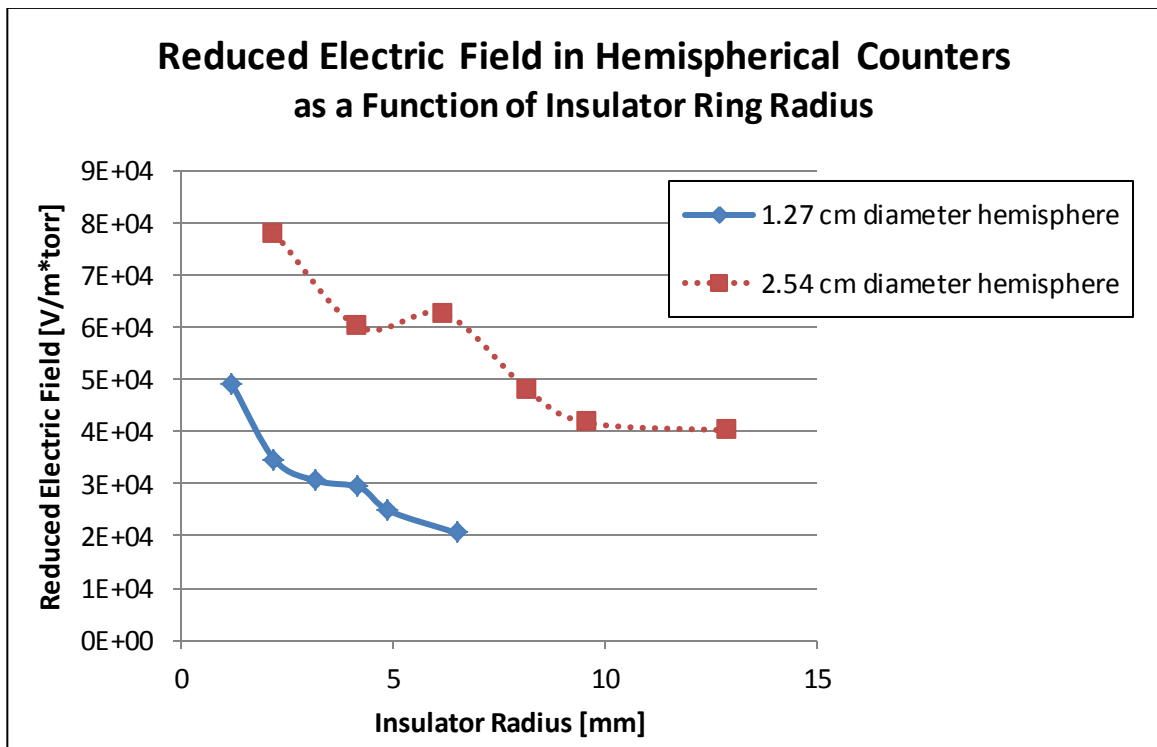


Figure 3.7 – Reduced electric field as a function of insulator ring radius

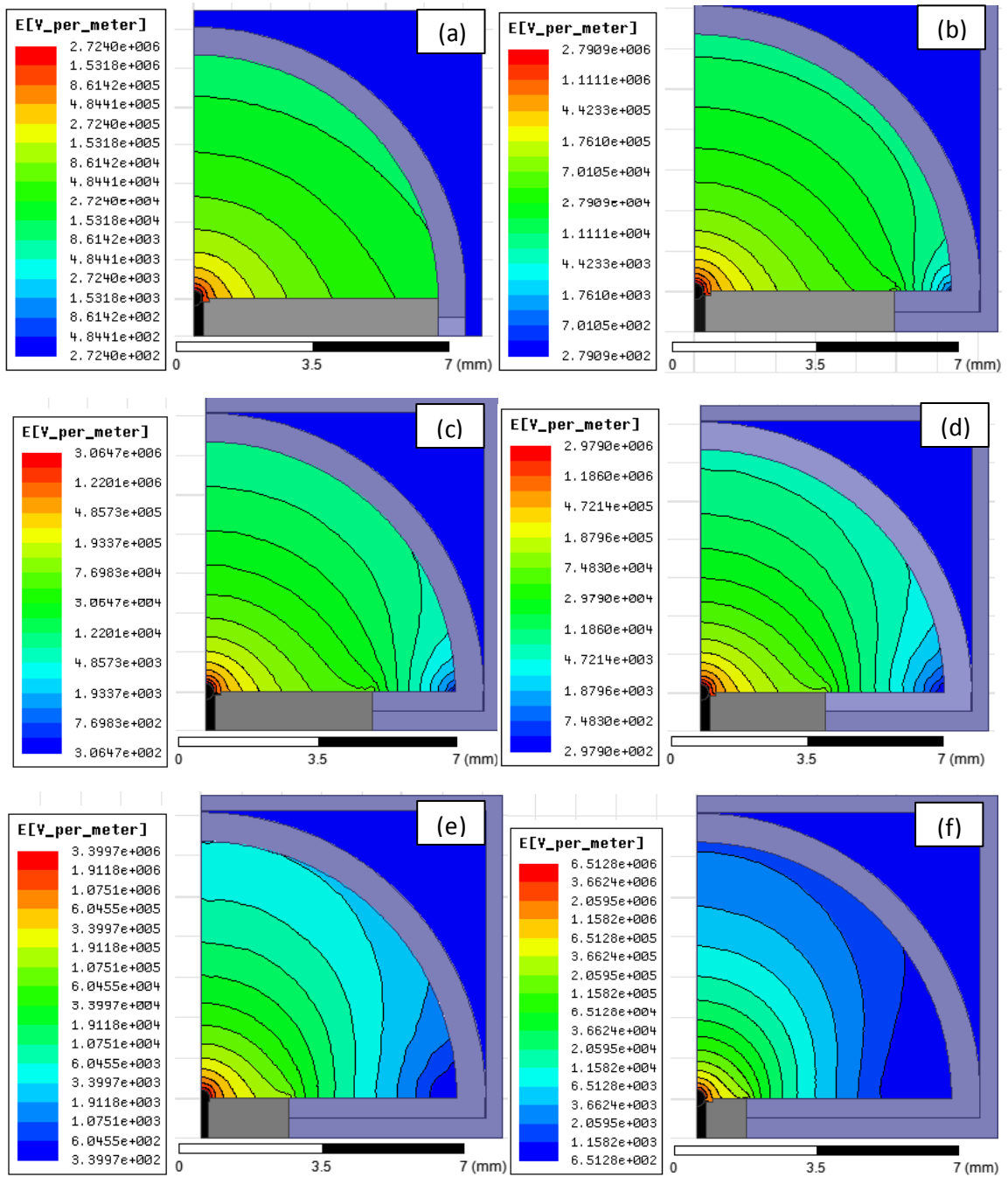


Figure 3.8 – Electric field distributions within 1.27 cm diameter hemisphere using various insulator radii: (a) 6.55 mm (b) 4.9 mm (c) 4.2 mm (d) 3.2 mm (e) 2.2 mm (f) 1.2 mm

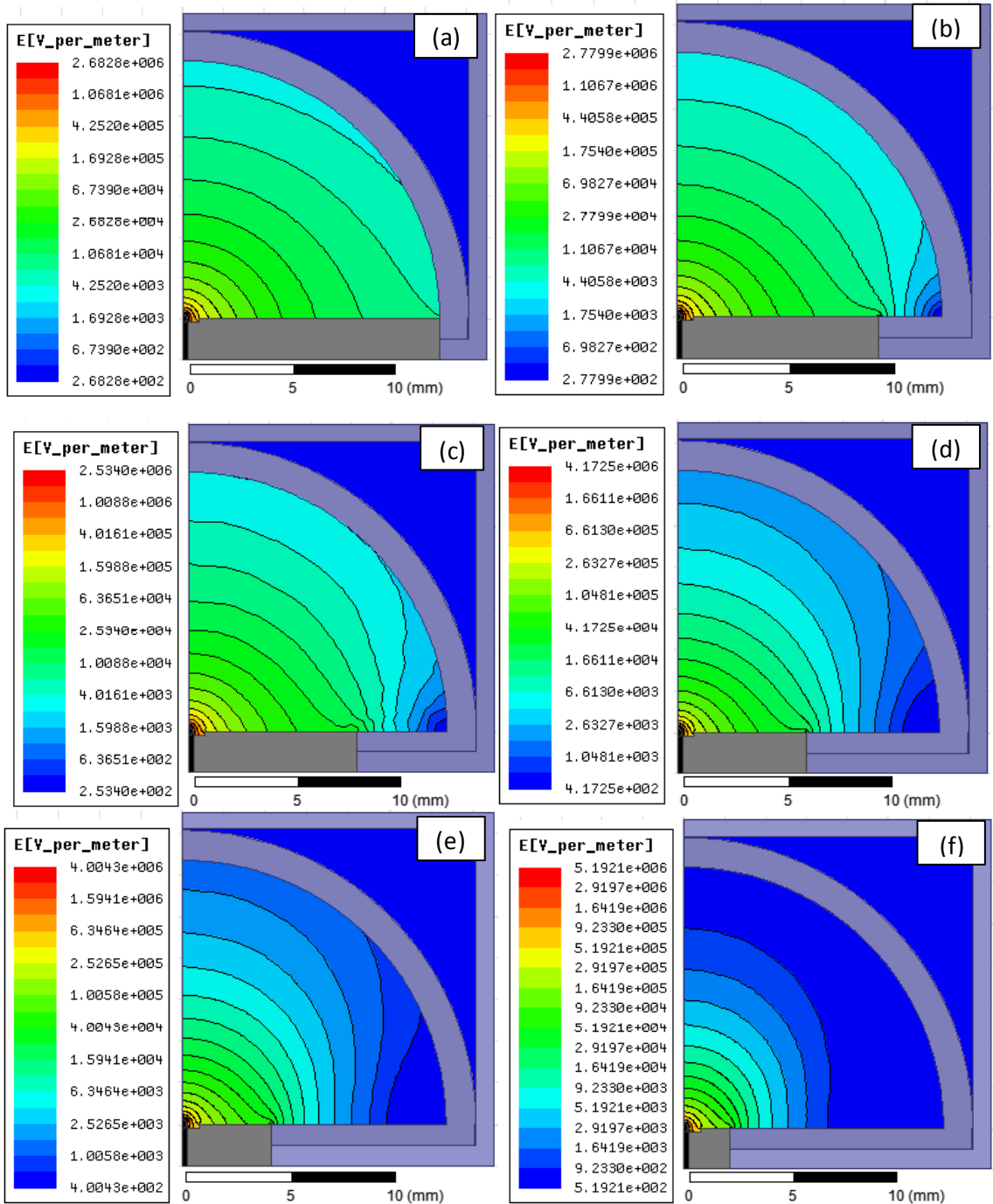


Figure 3.9 – Electric field distributions within 2.54 cm diameter hemisphere using various insulator radii: (a) 12.9 mm (b) 9.6 mm (c) 8.2 mm (d) 6.2 mm (e) 4.2 mm (f) 2.2 mm

Comparing the electric field distributions in hemispheres using various insulator radii it was found that the electric field strength and to a lesser degree the uniformity of the electric field distribution both are inversely proportional to insulator radius. Another factor that also

needs to be considered is the exposed insulator surface area. The larger this surface area is the more likely it is to collect ions over time, whose charge will cause irregular changes in the electric field. When balancing these conflicting factors the ideal insulator has the smallest surface area possible without significantly disturbing electric field uniformity. This condition is satisfied by the models with insulator radii of  $2.2\text{ mm}$  and  $4.2\text{ mm}$  for the  $1.27\text{ cm}$  and  $2.54\text{ cm}$  diameter hemispheres, respectively.

The final choice between these two hemisphere sizes was made based on maximizing the reduced electric field, which is the quotient of the electric field at the anodes surface and the gas pressure. As these factors directly affect electron interactions this is relevant for determining the magnitude of gas multiplication. Since the  $2.54\text{ cm}$  counter requires half the gas pressure of the smaller counter, this offsets the minor decrease in the electric field strength seen in Table 3.1. For this reason, the  $2.54\text{ cm}$  diameter hemisphere with a  $2.2\text{ mm}$  radius insulator ring illustrated in Figure 3.10 was selected.

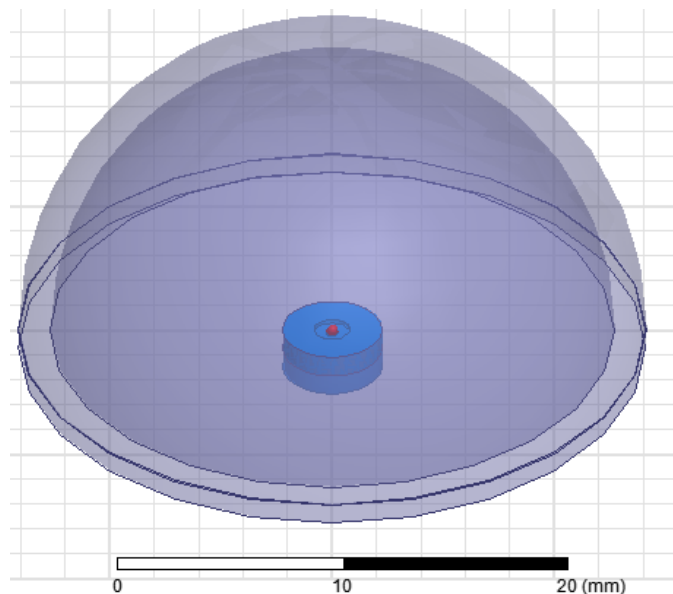


Figure 3.10 – Illustration of  $2.54\text{ cm}$  diameter hemisphere with  $0.4\text{ mm}$  diameter anode (red) and  $2.2\text{ mm}$  radius insulator (blue)

As the reduced electric field affects gas gain, it would be ideal if the magnitude of the reduced electric field for the hemispherical counter matched that of the reference spherical detector to ensure equivalent electron multiplication. The two values differ by a factor of ten, which directly corresponds to the difference in gas pressure between the counters. This is not believed to be significant as the magnitude of the reduced electric field for the hemispherical counter is still nearly twice that of the cylindrical counter illustrated in Figure 3.3. The reduced electric field of this cylindrical counter is only  $385 \text{ V torr}^{-1} \text{ cm}^{-1}$  (see Appendix I for calculation) and it has been demonstrated experimentally that the cylindrical counter performs very well in terms of electron multiplication [53, 54].

#### *3.4.3.1 Specifications of Counter Designs for Analysis*

With the conceptual hemispherical TEPC design defined, a simulated performance analysis was required to evaluate its performance relative to current TEPC designs. This analysis included the reference spherical TEPC as well as a cylindrical METEPC element, as illustrated in Figures 3.2, 3.3 and 3.5. The specifics regarding each of these detectors including the gas pressures and applied high voltages used throughout the analysis are outlined in Table 3.2. In order to compare the relative dosimetric performance of a sphere with the same diameter as the hemisphere the reference spherical TEPC was also scaled down in size to match that of the hemisphere.

TEPC geometry	Spherical	Spherical	Hemispherical	Cylindrical
Dimensions [cm] ( $d$ = diameter, $h$ = height)	$d = 12.7$	$d = 2.54$	$d = 2.54$	$d = 0.5$ $h = 5$
Anode type/diameter [ $\mu\text{m}$ ]	Wire/70	-	Ball/4000	Wire/50
Wall thickness [cm]	0.213	0.213	0.213	0.213
Simulated diameter [ $\mu\text{m}$ ]	2	2	4	2
Mean chord length [ $\mu\text{m}$ ]	1.33	1.33	1.78	1.91
Gas Pressure [torr]	6.67	33.35	66.7	167
Anode Potential [V]	700	-	750	750
Cathode Potential [V]	0	-	0	0
Mass of Gas [mg]	16.9	0.676	0.676	0.393
Cavity Volume [ $\text{cm}^3$ ]	1072.5	68.64	34.32	0.98
Gas Density [ $10^{-5} \text{g}/\text{cm}^3$ ]	1.58	0.985	1.97	40.1
Surface Area [ $\text{cm}^2$ ]	506.7	20.27	15.2	17.28

Table 3.2 – Parameters of detectors used throughout analysis

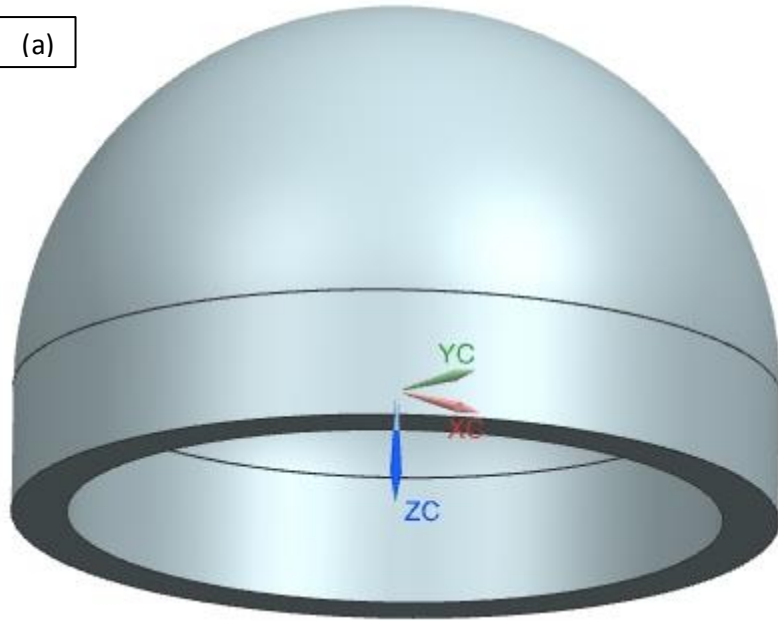
The results for analysing the each of these counters for the three performance aspects of neutron transport, energy deposition, and gas gain [22] will be presented in Chapters 4 and 5.

### ***3.4.3.2 Recommendations for Manufacturing the Conceptual Hemispherical Counter***

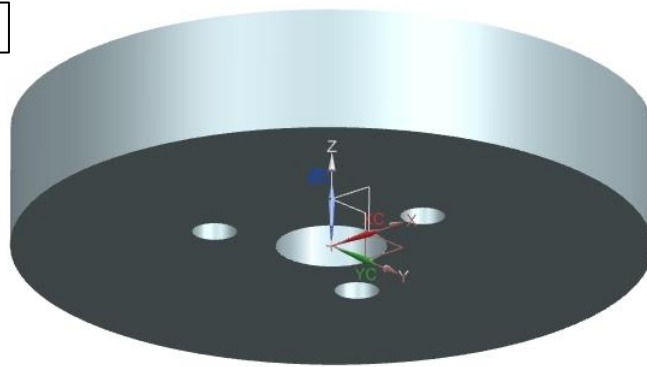
Although the hemisphere design illustrated in Figure 3.10 is the primary focus of the performance analysis, some consideration was also given to the construction of an actual hemispherical TEPC. This section includes a description of a proposed design for the cathode shell and an insulator support piece. In order to make construction of the counter more easily manageable it is suggested that the thickness of the cylindrical base portion of the cathode of the hemispherical counter be increased from 2.13 mm to 5 mm. This modification allows for the cylindrical base of the counter to be more easily fixed in place with screws. This would include three screws upwards through the bottom of the insulator into the cylindrical base (attaching the pieces shown in Figure 3.11 (b) and (c)), as well as three screw attaching the bottom portion

of the hemispherical shell to the cylindrical base (attaching the pieces shown in Figure 3.11 (a) and (b)). It is suggested that the tapping drill holes in the A-150 base, shown in Figure 3.11 (b), are size 50 (0.07") and the clearance drill size 43 (0.089") is used for the insulator, shown in Figure 3.11 (c) and (d). The appropriate screw size for these holes would be 2, with 56 threads per inch. This conceptual design is illustrated in Figure 3.11 (a) to (d) which includes both the hemispherical shell and the insulator piece which would be used to mount the hemisphere within the gas containment shell.

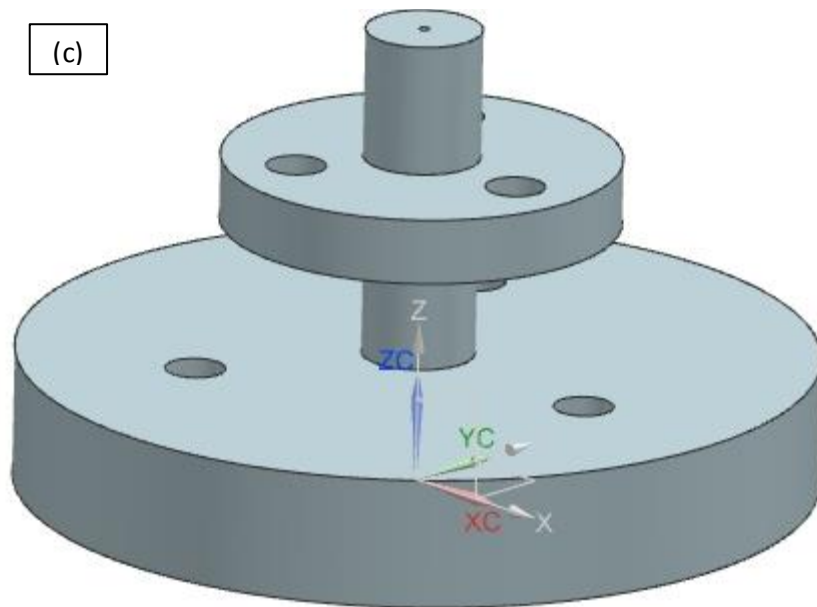
(a)



(b)



(c)



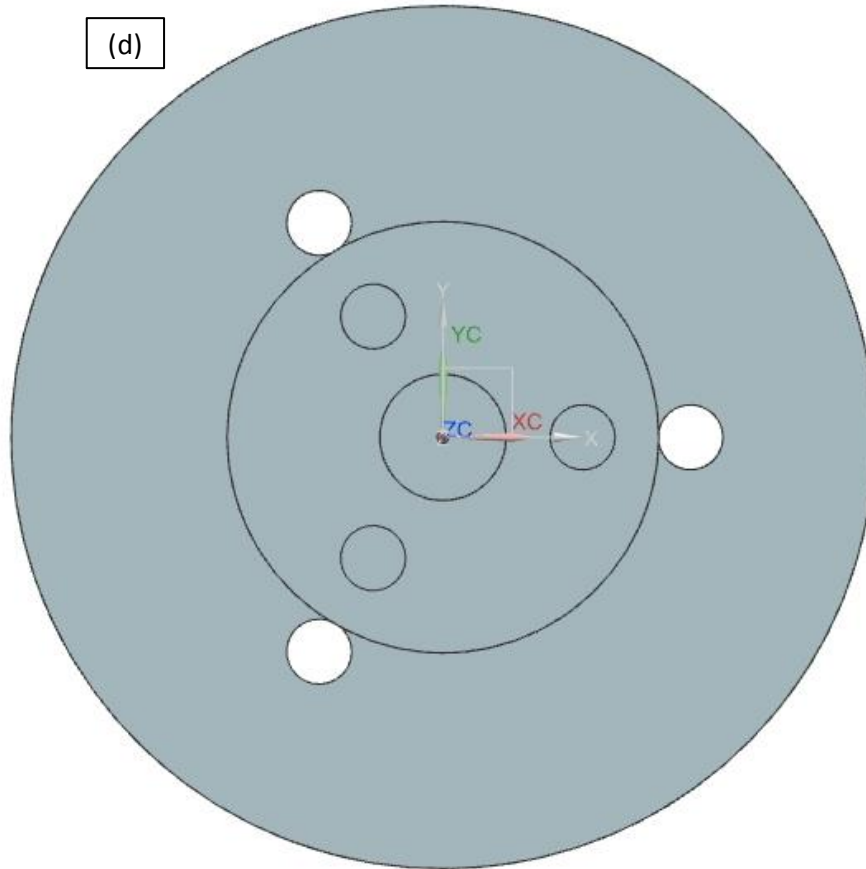


Figure 3.11 – Illustration of proposed hemispherical counter prototype design:  
 (a) 2.13 *mm* thick A-150 hemisphere walls with 5 *mm* extension at bottom; (b) 5 *mm* thick A-150 hemisphere base with three tap holes; (c) insulator with 3 tapped holes which align with those of the hemispheres base and 3 tapped holes to fix the base of the insulator in place;  
 (d) top view of insulator tapped holes

### 3.5 Geometric Sources of Variance

Prior to the evaluating detector performance, the theoretical aspects of the effects of geometry on measurement variance will be reviewed. The geometric effects are discussed in the context of the other random factors causing variations of the measured energy deposition within a proportional counter. As shown in Figure 3.12 these factors are interrelated with one another. The random factors are divided in four main categories, and are nearly all independent of detector geometry.

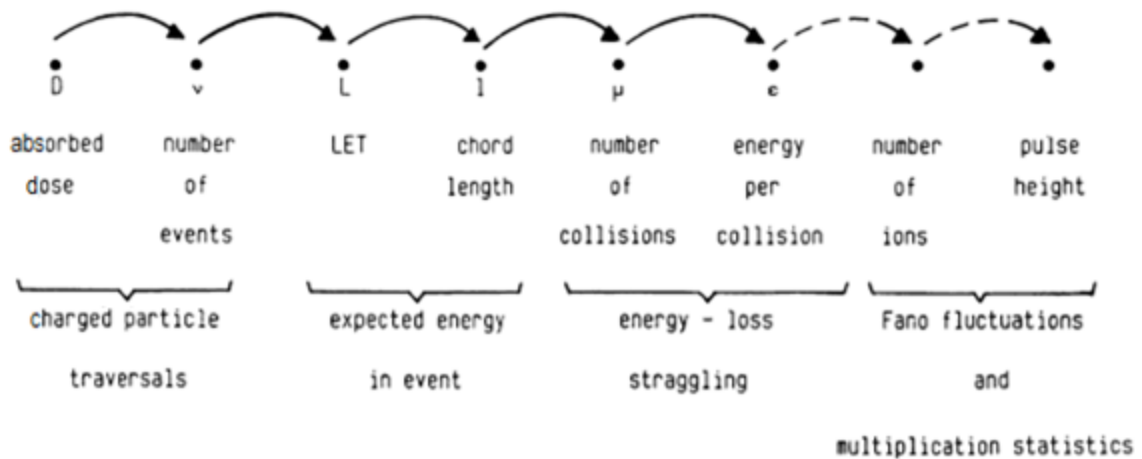


Figure 3.12 – Diagram of the chain of random factors which determine energy deposition in a site [56]

The absorbed dose and number of events are dependent upon the exposure length and dose rate. The LET depends upon the charged particles initial energy and whether the given charged particle has an LET distribution. LET averages out the dominant source of variation in microdosimetry, energy straggling, which is the variation in energy loss per collision. Ionization is dependent on whether or not sufficient energy is deposited to ionize an atom, and this directly affects the fluctuation in the number of ions produced. The measured pulse height results from the outcome of all other sources of variation along with the additional variance due to the multiplication statistics during the electron avalanche.

Chord length is the only one of these random factors with a relative variance that directly depends on detector geometry. Microdosimetric calculations use the mean chord length as an approximate of the true path length, which is reasonably accurate as the majority of heavy charged particle cross the gas cavity in a straight line. In Table 3.3 the mean chord length is presented along with the geometry dependent relative variance for each of the analyzed detector geometries. The relative variance of the mean chord length, as presented in Table 3.3, is then representative of the relative variance of particle track length through the gas cavity of each counter. This gives an indication the accuracy of the mean chord length for each geometry.

Geometry	Mean Chord Length, $\bar{l}$ , 2 $\mu\text{m}$ site		Relative Variance of modelled counters [57]	
Sphere	$\frac{2d}{3}$ , $d = \text{diameter}$	$\bar{l} = 1.33 \mu\text{m}$	12.5%	0.167 $\mu\text{m}$
Cylinder (elongation 10)	$\frac{d * h}{\left(\frac{d}{2}\right) + h}$ $d = \text{diameter}, h = \text{height}$	$\bar{l} = 1.91 \mu\text{m}$	60%**	1.146 $\mu\text{m}$
Hemisphere	$\frac{8r}{9}$ , $r = \text{radius}$	$\bar{l} = 1.78 \mu\text{m} *$	26.6%	0.474 $\mu\text{m}$

Table 3.3 – Mean chord lengths along with respective relative variances for simulation of a 2  $\mu\text{m}$  diameter site (\*for the hemisphere the radius is defined as 2  $\mu\text{m}$  to better resemble the other detectors, \*\*the relative variance of a cylinder is dependent upon its elongation, this is for the simulated cylinder where  $\text{height} = 10 \times \text{diameter}$ )

The variance values presented in Table 3.3 were reported by Bradley [57], who conducted an analysis based on the chord length probability distributions presented in Table 3.4.

Geometry	Chord Length Distribution, $f(l)$
Sphere [22]	$\frac{2l}{d^2}, 0 < l \leq d, d = \text{diameter}$
Cylinder	The distribution for a cylinder is extensive, and varies depending on elongation; see [59, 60, 61, 62]
Hemisphere [58]	$\frac{2l}{3\pi^2} H(r-l) + \frac{1}{\pi r} c_1 + \frac{2r}{3\pi l^2} \left( c_1 + \frac{2r}{l} \left( \cos^{-1}\left(\frac{l}{2r}\right) - \frac{\pi}{2} H(r-l) \right) \right)$ $c_1 = \sqrt{1 - \frac{l^2}{4\pi r^2}}$ $r = \text{radius}, H = \text{step function}$

Table 3.4 – Chord length distributions within spherical, cylindrical and hemispherical counter geometries

The isotropic geometry of the sphere gives it the lowest possible chord length variance of all geometries. The relative variance of the hemisphere is comparable to that of a right cylinder which has a relative chord length variance of 25% [57]. This demonstrates that although

the hemisphere has a relative variance slightly more than twice that of a sphere, its relative chord length variance is comparable to or less than even the ideal cylinder. Along with the electrostatics analysis of Section 3.4.3 this shows that the hemisphere has potential as a TEPC.

## Chapter 4: Characterizing Gas Gain

### 4.1 Introduction

The process of electron multiplication in a proportional counter is commonly referred to as gas gain and can be analyzed using the following methods: the Monte Carlo method which involves tracking individual electrons and their interactions, or the semi-empirical method which uses the mean probability of an interaction occurring per unit path-length to determine the mean gain. Although less precise, the semi-empirical method is reported to be accurate within 10% [28], which has been deemed sufficiently accurate for characterizing gain parameters within TEPCs [46]. Previous applications of the semi-empirical method solely employed the analytical electric field equations, which model radiation detectors using unrealistic perfectly symmetric geometries. This study combines a computational electrostatic analysis of each detector with the semi-empirical method in an attempt to increase accuracy by using the true local potential values in place of simplified analytical values when calculating the electric field. The additional benefit of this method is that it allows the gain to be determined as a function of radial distance for electrons approaching the anode from throughout the gas cavity.

#### 4.1.1 ANSYS Maxwell

The electrostatics for each of the proportional counters were numerically analyzed using the commercial software ANSYS Maxwell V.14.0. This requires input of each detector's geometry, material properties (including bulk conductivity and relative permittivity), and defining the electric potentials of the electrodes. Using this user input data Maxwell numerically solves the following two dimensional differential Maxwell equation [63]:

$$\nabla \cdot (D) = -\rho$$

$$\nabla \cdot (\varepsilon_r \varepsilon_0 \phi(z, y)) = -\rho \quad (4.1)$$

where the electric flux density,  $D$ , is calculated as the product of the materials permittivity,  $\varepsilon = \varepsilon_r \varepsilon_0$ , and the scalar applied potential at a defined position,  $\phi(z, y)$  [64]. The gradient,  $\nabla = (\frac{\partial}{\partial z}, \frac{\partial}{\partial y})$ , of this flux density between the mesh of finite elements within the model is then used to determine the charge density,  $\rho$ , around the position  $(z, y)$ . This can then be used to determine the electric field distribution. The specific method used for this step is not disclosed; however the following relation may be used for calculating the electric field:

$$E = -\nabla \cdot \phi \quad (4.2)$$

As charge density can also be used for calculating the electric field it is quite possible that this is not the relationship employed by Maxwell's electrostatic solver.

In order to evaluate the numerical solution quickly the two dimensional model is separated into a finite mesh of nodes. The nodes are positioned such that their concentration is proportional to the rate of potential change, which is higher closer to the anode in the region where electron multiplication is concentrated. Following each evaluation of the electrostatic solution the mesh is iteratively refined and the solution is re-evaluated either until the user input level of accuracy is met or maximum number of iterations is reached [63]. Throughout this study the values selected were 0.01% and 50 iterations, respectively. Once the analysis is completed the scalar and vector values for the potential and electric field are defined at each node within the model. The use of this data will be clarified following a brief overview of gas gain theory.

## 4.2 General Gas Multiplication Theory

Gas gain,  $G$ , is defined as the ratio of the number of electrons collected at the anode,  $N_{final}$ , to the number of primary electrons,  $N_r$ , generated by an energy deposition event in the gas cavity:

$$G = \frac{N_{final}}{N_r} \quad (4.3)$$

The number of electrons generated during multiplication is the difference between the number of primary and collected electrons:

$$dN = N_{final} - N_r \quad (4.4)$$

This can be determined as the product of the number of primary electrons, the Townsend first ionization coefficient,  $\alpha(r)$ , which is the mean number of ion pairs generated per unit path length, and the path length,  $dr$ :

$$dN = N_r \alpha(r) dr \quad (4.5)$$

When rearranged and integrated this can be applied to calculate the gas gain over the distance,  $d$ :

$$\int_{N_o}^{N_{final}} \frac{dN}{N_r} = \int_0^d \alpha(r) dr$$

$$[\ln N_r]_{N_o}^{N_{final}} = \alpha [r]_0^d$$

$$\ln N_{final} - \ln N_o = \alpha d$$

$$\ln(G) = \ln\left(\frac{N_{final}}{N_o}\right) = \alpha d \quad (4.6)$$

For a proportional counter the total gas gain is determined using the integration limits of  $a$  and  $b$ , representing the anode and the inner cathode radii, respectively:

$$\ln(G) = \int_a^b \alpha(r) dr \quad (4.7)$$

The Townsend coefficient is dependent upon several factors, all of which are constant within a given detector simulating a given site size; with only the electric field,  $E(r)$ , varying radially [48]:

$$\alpha(r) = pA * \exp\left(-\frac{Bp}{E(r)}\right) \quad (4.8)$$

The constant factors are the gas pressure,  $p$ , and the gas dependent constants  $A$  and  $B$ , which represent the reciprocal of the electron mean free path at unit pressure,  $1/\lambda_1$ , and the ratio of the effective ionization potential to the mean free path at unit pressure,  $V_i/\lambda_1$ , respectively [28].

Although universally referred to as constants, the values of  $A$  and  $B$  vary with a slight dependence on the reduced electric field. The values of  $A$  and  $B$  used in this study were experimentally determined [28] in reduced electric fields comparable to those within the detectors analyzed in this study. Due to the different magnitudes of the reduced electric fields in each of the detectors a different set of gas constants was required for each of the three counters; see Appendix I for details on how these gas constants were determined.

#### 4.2.1 Gas Gain in Cylindrical Counters

The analytical electric field model used to determine the Townsend coefficient for cylindrical counters is:

$$E(r) = \frac{V_{a \rightarrow b}}{r \ln\left(\frac{b}{a}\right)}; \quad a \leq r \leq b \quad (4.9)$$

Where  $V_{a \rightarrow b}$  represents the electric potential difference between the anode and cathode radii:

$$V_{a \rightarrow b} = V_a - V_b \quad (4.10)$$

This is a simplified analytical model as the anode and cathode are approximated as two concentric cylindrical electrodes of infinite length, disregarding end effects [19]. By using this equation for electric field (4.9) to determine the Townsend coefficient (4.8) and then putting this into the general gas gain equation (4.7) a practical equation for calculating gas gain is obtained:

$$\ln(G) = \int_a^b pA * \exp\left(-\frac{Bpr \ln\left(\frac{b}{a}\right)}{V_{a \rightarrow b}}\right) dr \quad (4.11)$$

$$\ln(G) = \frac{A}{B} \frac{V_{a \rightarrow b}}{\ln\left(\frac{b}{a}\right)} \left( \exp\left(-\frac{Bpa * \ln\left(\frac{b}{a}\right)}{V_{a \rightarrow b}}\right) - \exp\left(-\frac{Bpb * \ln\left(\frac{b}{a}\right)}{V_{a \rightarrow b}}\right) \right) \quad (4.12)$$

This is the form of the Campion gas gain equation, which is useful for determining the magnitude of the total gas gain in a counter [48]. To calculate the gas gain occurring between the anode and a defined radius within the cavity, the upper limit of the Campion equation can be replaced by the variable,  $r$ , where  $a \leq r \leq b$ , resulting in:

$$\ln(G) = \frac{A}{B} \frac{V_{a \rightarrow b}}{\ln\left(\frac{b}{a}\right)} \left( \exp\left(-\frac{Bpa * \ln\left(\frac{b}{a}\right)}{V_{a \rightarrow b}}\right) - \exp\left(-\frac{Bpr * \ln\left(\frac{b}{a}\right)}{V_{a \rightarrow b}}\right) \right) \quad (4.13)$$

This form of the Campion equation was used for the theoretical gain calculations using the simplified analytical potential distribution. The potential distribution generated in Maxwell can also be used to calculate gain following a substitution. As the Maxwell potential distribution defines the potential at points,  $(z, r)$ , where  $z$  represents the vertical position along the anode and  $r$  represents the radial distance from the center of the anode, the voltage potential difference between radii  $a$  and  $r$  can be determined as:

$$V_{a \rightarrow r} = V_a - V_r \quad (4.14)$$

By substituting  $V_{a \rightarrow r}$  in place of  $V_{a \rightarrow b}$  the true potential difference between the radii  $a$  and  $r$  may be used instead of the theoretical difference determined using the simplified analytical model. This substitution is made possible by applying the following equality:

$$V_{a \rightarrow b} = V_{a \rightarrow r} * \frac{\ln\left(\frac{b}{a}\right)}{\ln\left(\frac{r}{b}\right)} \quad (4.15)$$

When applied to the second term of Equation 4.13 this produces an alternative equation for calculating gas gain:

$$\ln(G) = \frac{A}{B} \frac{V_{a \rightarrow b}}{\ln\left(\frac{b}{a}\right)} \left( \exp\left(-\frac{Bpa * \ln\left(\frac{b}{a}\right)}{V_{a \rightarrow b}}\right) - \exp\left(-\frac{Bpr * \ln\left(\frac{r}{a}\right)}{V_{a \rightarrow r}}\right) \right) \quad (4.16)$$

This equation was used for calculating the analytical gas gain radial distributions using the data generated using ANSYS Maxwell.

#### 4.2.2 Gas Gain in Spherical Counters

As no equation for the electric field within a spherical counter exists a modified form of the equation for the electric field within the cylindrical counter (4.9) has been shown to work [48]. The modification requires the spherical counter to be modelled as a specific type of cylindrical counter. The cylindrical counter with equivalent gain has a height equal to the diameter of the sphere, and a diameter such that the cylindrical and spherical counters have equivalent volumes [48]. The radius of this equivalent cylindrical counter,  $r_c$ , is then determined as follows:

$$V_{cylinder} = V_{sphere}$$

$$\pi r_c^2(2r_s) = \frac{4}{3}\pi r_s^3$$

$$r_c^2 = \frac{2}{3}r_s^2$$

$$r_c = \sqrt{\frac{2}{3}r_s^2} \quad (4.17)$$

For the case of the spherical counter analyzed here which has a radius,  $r_s = 6.35 \text{ cm}$ , the cylindrical counter with equivalent gain has a radius,  $r_c = 5.19 \text{ cm}$ . This value of  $r_c$  was used as  $b$  in Equation 4.13 along with an appropriate  $r$  value, within the range of  $a \leq r \leq 5.19 \text{ cm}$ , for determining the theoretical gain using the simplified analytical analysis. Following the calculation of gas gain the radii,  $r$ , were converted back to their respective spherical values using:

$$r_s = \sqrt{\frac{3}{2}r_c^2} \quad (4.18)$$

When calculating gain using the analytical data from Maxwell the same  $b$  value of  $5.19 \text{ cm}$  was used. The series of  $r$  values corresponding to the radii at which the potentials  $V_r$  were defined were input as  $r_s$  in Equation 4.17 to determine the appropriate  $r_c$  value use as  $r$  in Equation 4.16. When plotting results the original  $r_s$  values were used to define the spherical counters gas gain distribution.

### 4.2.3 Gas Gain in Hemispherical Counters

As the electric field within the hemispherical counter varies proportional to  $1/r^2$  instead of the  $1/r$  relationship of the cylindrical and spherical geometries a different equation must be applied. Similar to the model used for the cylindrical and spherical counters, a simplified version

of the hemispherical counters true geometry is used. In this case the counter is modelled using the electric field equation for two concentric hemispheres:

$$E(r) = \frac{V_{a \rightarrow b} ba}{(b-a)r^2} \quad (4.19)$$

Using this electric field equation the appropriate Townsend coefficient (Equation 4.8) can be determined for substitution in Equation 4.7 to produce the simplified analytical equation for gas gain in a hemispherical counter:

$$\begin{aligned} \ln(G) &= \int_a^r pA * \exp\left(-\frac{Bp(b-a)r^2}{V_{a \rightarrow b} ba}\right) dr \\ \ln(G) &= \frac{\sqrt{\pi} pA}{2\sqrt{\left(\frac{Bp(b-a)}{V_{a \rightarrow b} ba}\right)}} \left[ -\operatorname{erf}\left(\sqrt{\frac{Bp(b-a)}{V_{a \rightarrow b} ba}} a\right) + \operatorname{erf}\left(\sqrt{\frac{Bp(b-a)}{V_{a \rightarrow b} ba}} r\right) \right] \end{aligned} \quad (4.20)$$

Where *erf* represents the so called “error function” which ranges from -1 to 1 and is defined as the integral of the following normal distribution [65]:

$$\operatorname{erf}(z) \equiv \frac{2}{\sqrt{\pi}} \int_0^z e^{-t^2} dt \quad (4.21)$$

In order to apply the analytical data from Maxwell,  $V_{a \rightarrow r}$  must again be substituted for  $V_{a \rightarrow b}$ . This is made possible with the use of the following equality:

$$V_{a \rightarrow b} = V_{a \rightarrow r} * \frac{r(b-a)}{b(r-a)} \quad (4.22)$$

When this is substituted in the third term of Equation 4.20 an alternative gas gain equation is obtained which can employ the analytical results from the equipotential distribution generated in Maxwell:

$$\ln(G) = \frac{\sqrt{\pi}pA}{2\sqrt{\left(\frac{Bp(b-a)}{V_{a \rightarrow b}ba}\right)}} \left[ -\operatorname{erf}\left(\sqrt{\frac{Bp(b-a)}{V_{a \rightarrow b}ba}} a\right) + \operatorname{erf}\left(\sqrt{\frac{Bp(r-a)}{V_{a \rightarrow r}ba}} r\right) \right] \quad (4.23)$$

## 4.3 Results and Discussion

### 4.3.1 Cylindrical Counter

The equipotential distribution shown in Figure 4.1 was produced using ANSYS Maxwell; with the lower half of the counter omitted both from this figure and the gas gain analysis as the counter is symmetric. The horizontal black lines in Figure 4.1 illustrate the six positions along the anode wire where gas gain was analyzed. The total gain was calculated between the anode and a series of equipotential lines along the top of each of these lines illustrated and labelled in Figure 4.1.

The results produced from this analysis are presented in Figure 4.2 along with the theoretical gain generated by the simplified analytically method. As the results produced using both data sets align this validates the simplified theoretical solution as an accurate representation of the true potential distribution within this cylindrical counter, and may or may not extend to all cylindrical counters. This also demonstrates that this cylindrical METEPC element has ideal electrostatic characteristics as both the potential and gas gain distributions are completely uniform along the anode wire. This follows from qualitative analysis of Figure 4.1 where the equipotential lines are seen to be parallel in all regions except the upper 0.05 cm of the 5 cm long anode wire where the anode extension is present.

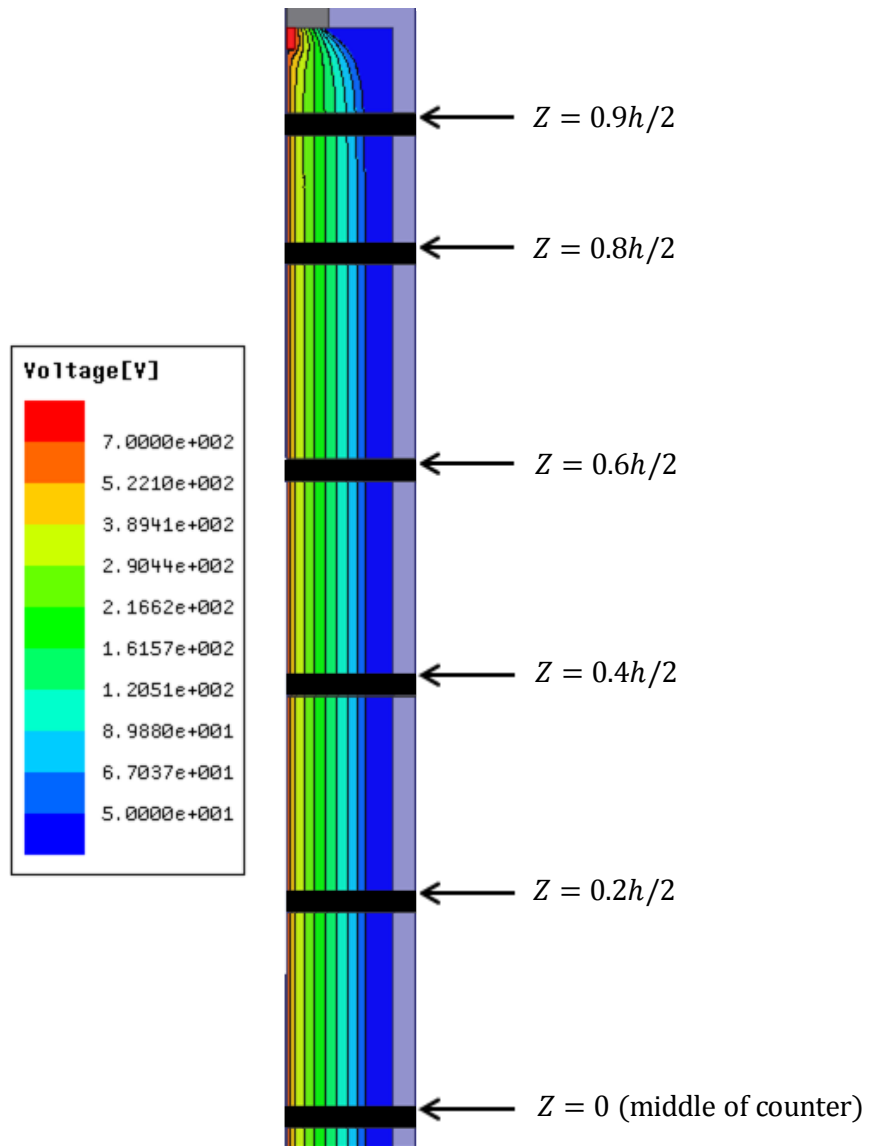


Figure 4.1 – Equipotential lines in 5 cm x 0.5 cm cylindrical counter ranging from 700 V to 50 V, with the 6 labelled lines showing where radial patterns in gas gain were analyzed

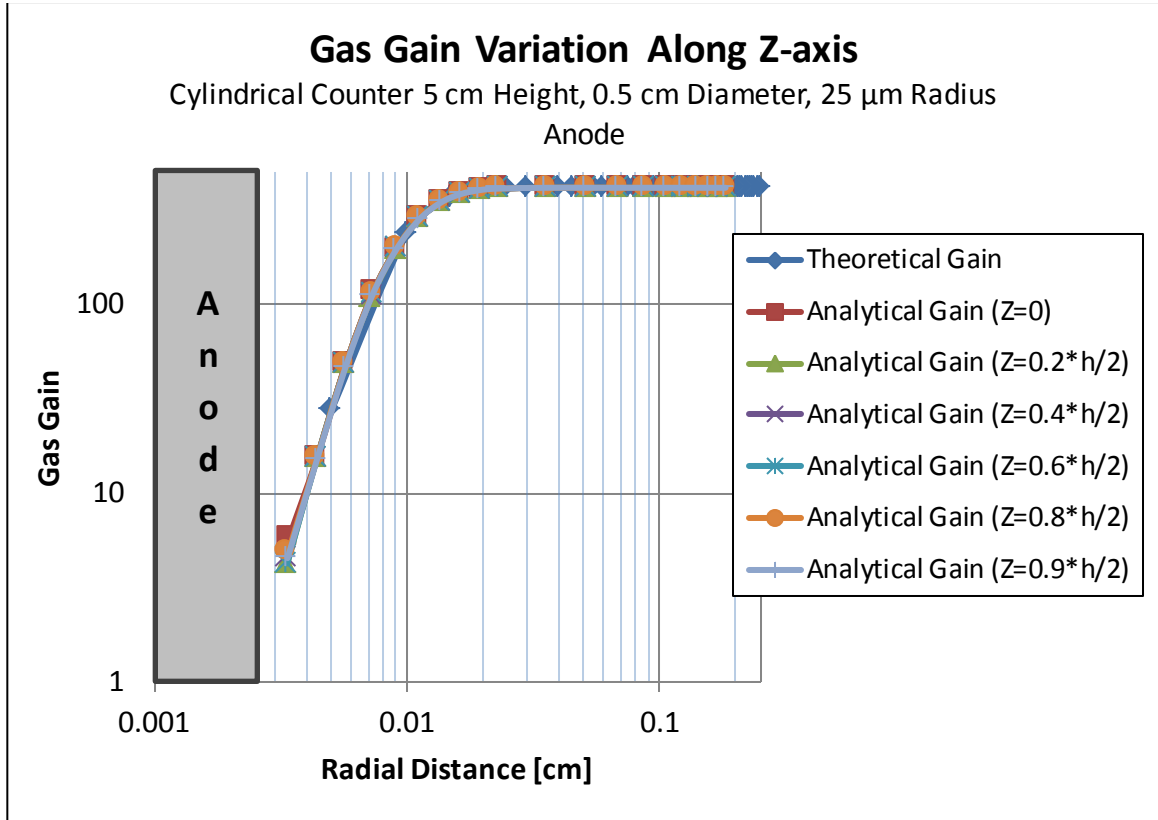


Figure 4.2 – Absolute gain as a function of radial distance within the cylindrical counter,  $Z$  represents the distance from the center of the anode wire as shown in Figure 4.1

The avalanche is defined as the region where 97% of all electron multiplication occurs [66], which occurs within a radius of 0.0195  $cm$  throughout the cavity of this counter. This avalanche radius can then be used to calculate the avalanche volume,  $v_{avalanche}$  as a percentage of the gas cavities total volume,  $v_{detector}$ :

$$\% \text{ of volume occupied by avalanche} = \frac{(v_{avalanche} - v_{anode})}{(v_{detector} - v_{anode})}$$

With the volume for each region calculated using:

$$v_{anode} = \pi * r_{anode}^2 * h$$

$$v_{avalanche} = \pi * r_{avalanche}^2 * h$$

$$v_{detector} = \pi * r_{cathode}^2 * h$$

where  $h = 5 \text{ cm}$ ,  $r_{anode} = 0.0025 \text{ cm}$ ,  $r_{avalanche} = 0.0195 \text{ cm}$  and  $r_{cathode} = 0.25 \text{ cm}$ . The avalanche occupies 0.60% of the cavities volume, leaving 99.4% of the cavity for electron drift. Nearly all of the primary electrons will originate within the drift region where they undergo full gas gain. As the maximum gain is uniform along the anode wires Z-axis, gas gain is uniform for nearly all primary electrons.

These analytical results appear to be reasonable when compared to the experimental analysis of gas gain variations along this counters anode wire. Shown in Figure 4.3 are the experimental results, which found that gas gain was relatively uniform along most of the wire, except for the ends of the anode wire where it decreased by approximately 6% [53].

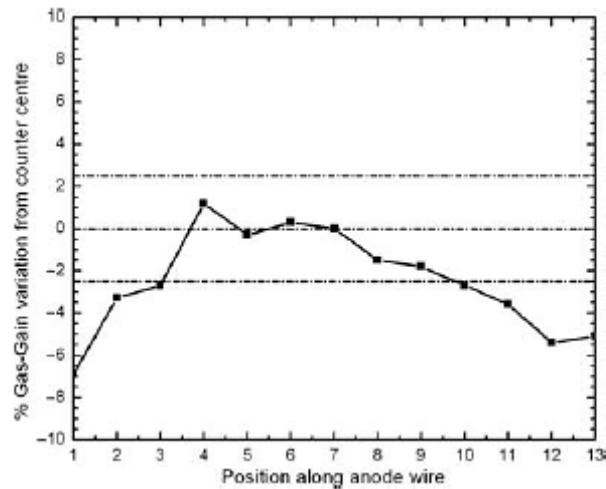


Figure 4.3 – Experimentally measured gas gain variation along the length of the anode wire [53]

Although the exact reason for the decrease in gain at the ends is unknown, it is possibly due to an experimental factor not accounted for in this analysis, such as charges collecting on the insulator surface and altering the electric field.

### 4.3.2 Spherical Counter

The equipotential distribution shown in Figure 4.4 was produced using ANSYS Maxwell. In discussing regions of the spherical counter's anode wire the upper half of the wire is referred to as  $Z = 0$  to  $r$ , the mid-point is  $Z = 0$ , and the lower half is  $Z = 0$  to  $-r$ . As with the cylindrical counter, the horizontal black lines in Figure 4.4 illustrate the positions along the anode wire where gas gain was analyzed.

The results of the Maxwell analysis are presented on Figure 4.5 along with the theoretical results generated using the simplified analytical method. Significant variations can be seen between the magnitudes of gain produced by the simplified method relative to the gain near ends of the wire. From Figure 4.6 it can be seen that the specific regions of the anode wire where these variations are seen are the ranges of  $r$  to  $0.6r$  and  $-r$  to  $-0.6r$ . In Figure 4.5 it can qualitatively be seen that for these regions greater than  $\pm 0.6r$  from the center of the anode the equipotential lines cease to be straight lines, especially near the anode where most of the gain occurs.

This was anticipated as towards the ends of the wire the distance between the anode and cathode is much less than at the center of the counter. Also, since the field shaping electrodes are for the most part outside of the spherical sensitive volume they are unable to completely correct the non-uniformities that occur a considerable distance within the counter. That being said, for the region surrounding the middle of the anode, within  $\pm 0.4r$ , the magnitude and radial distribution of gain determined using Maxwell align precisely with the theoretical gain calculated using the simplified analytical method (using Equations 4.13 and 4.17).

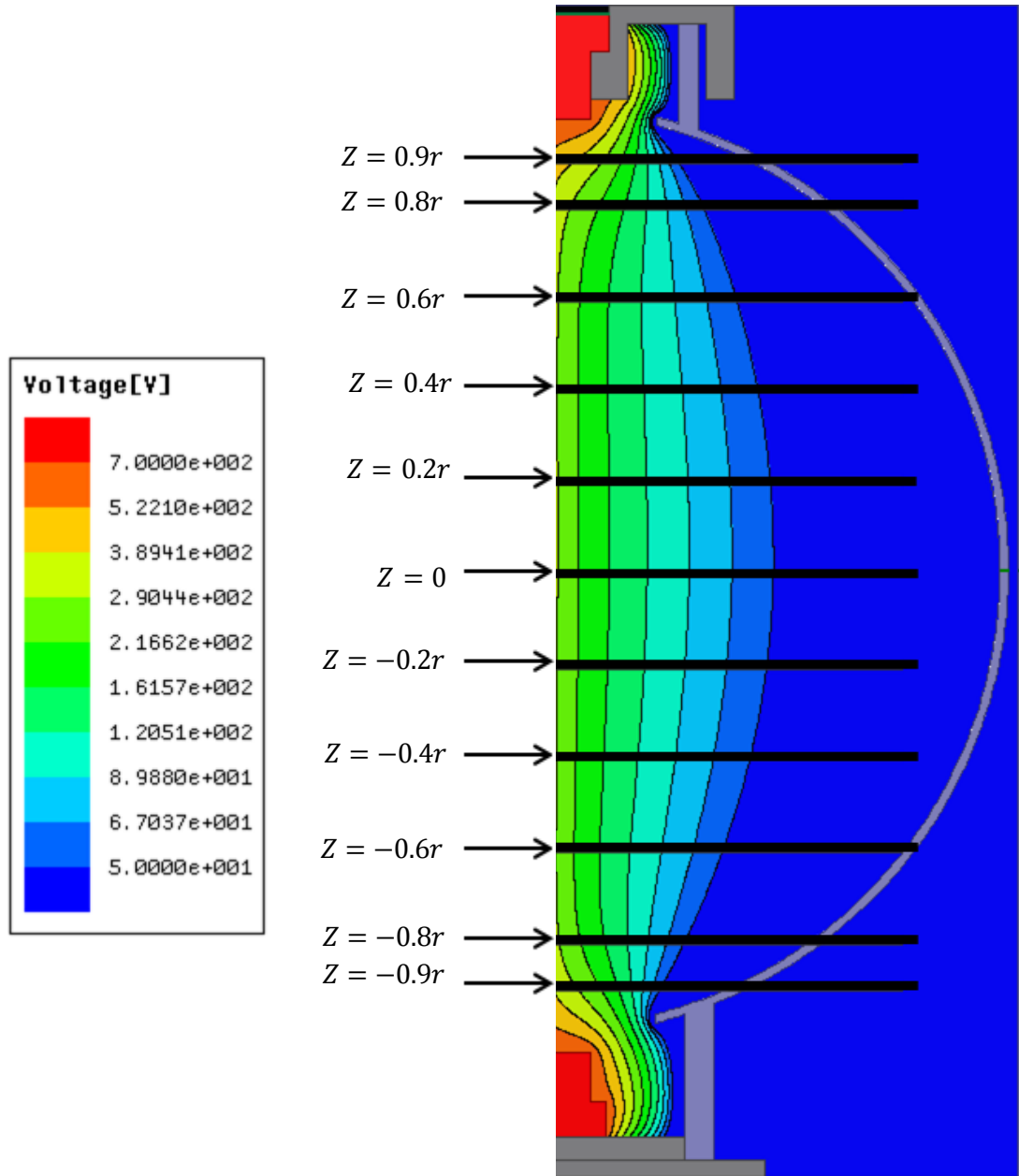


Figure 4.4 – Equipotential lines in the 12.7 cm spherical counter ranging from 700 V to 50 V, with the 11 labelled lines showing where radial patterns of gas gain were analyzed

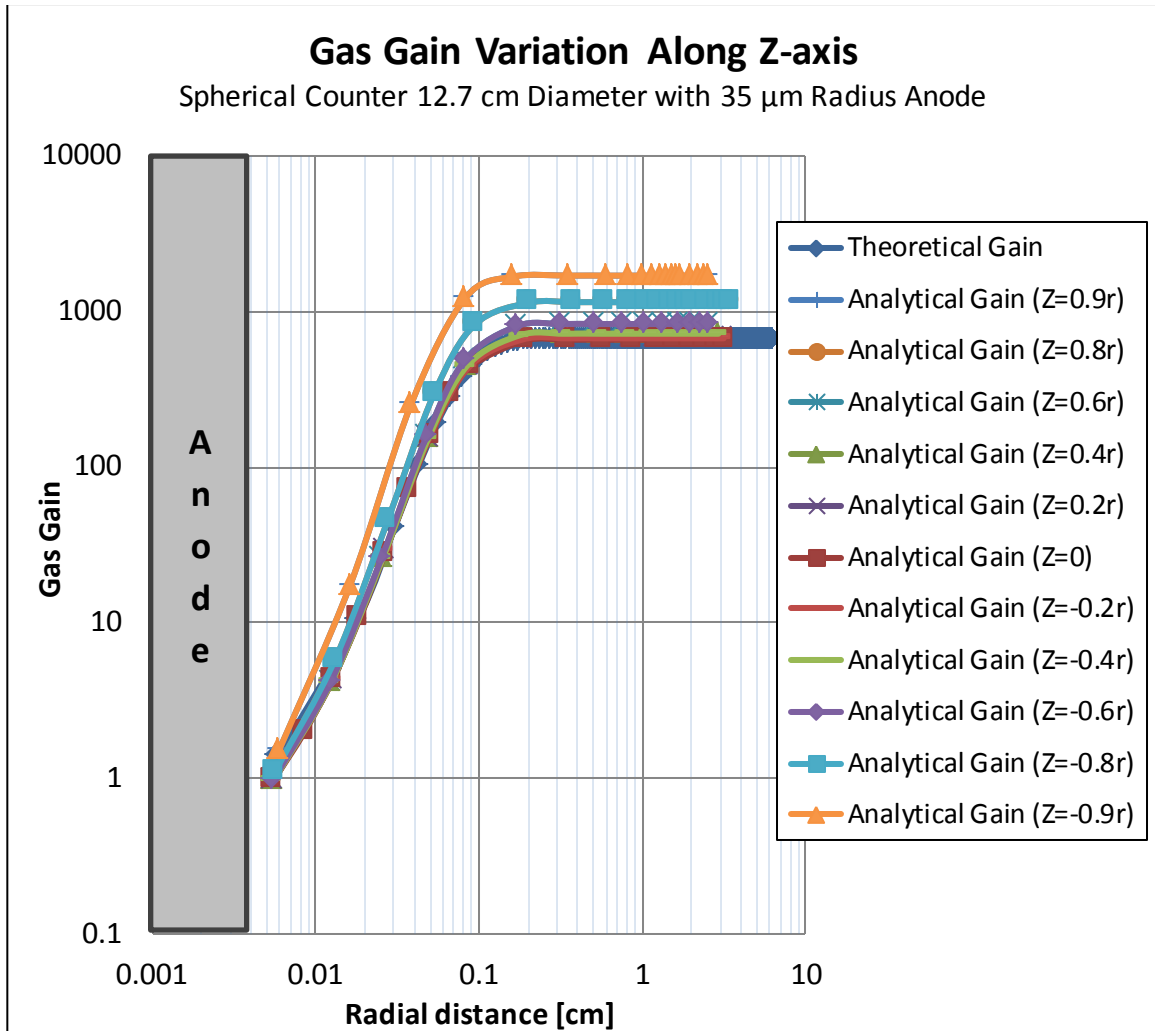


Figure 4.5 – Absolute gain as a function of radial distance within the spherical counter,  $Z$  represents the distance from the center of the anode wire as shown in Figure 4.4

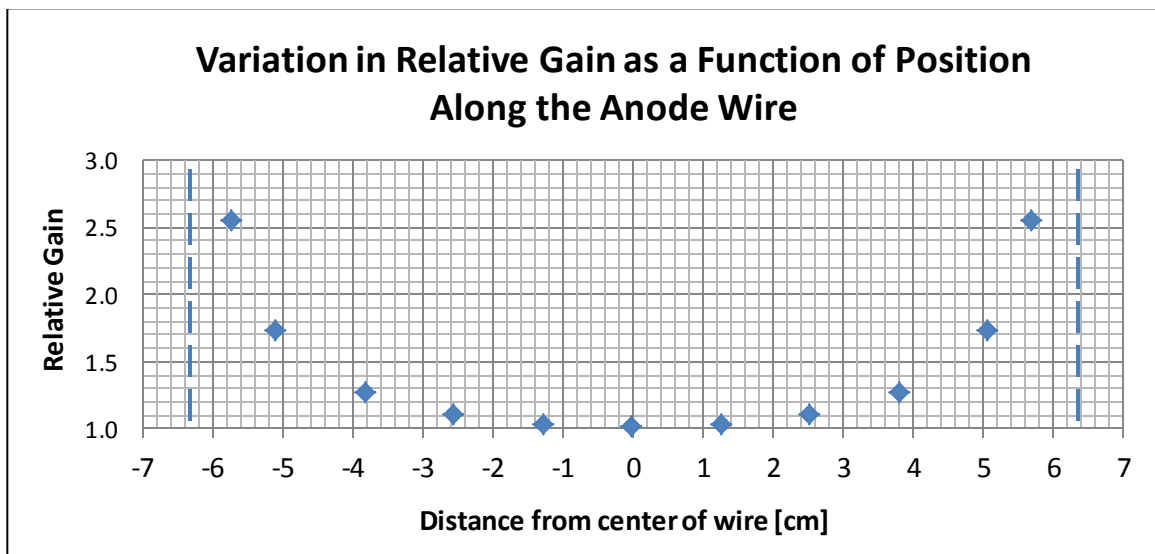


Figure 4.6 – Maximum gas gain along the anode wire relative to the center of the anode wire

As the Campion method of calculating gas gain is accurate within 10% [28], the region covering  $Z = -0.4r$  to  $0.4$  where the maximum gain varies 9% can be considered as having reasonably uniform gain. The avalanche radius along the anode wire does exhibit slight variations, ranging from  $0.13 \text{ cm}$  to  $0.20 \text{ cm}$ , however the avalanche volume can be modelled as a cylindrical volume with the avalanches average dimensions of  $0.18 \text{ cm}$  radius and  $12.7 \text{ cm}$  height. The percent of the total gas volume that the avalanche accounts for can then be determined as:

$$v_{anode} = \pi * r_{anode}^2 * d_{sphere} = 4.89 \times 10^{-4} \text{ cm}^3$$

$$v_{avalanche} = \pi * r_{avalanche}^2 * d_{sphere} = 1.29 \text{ cm}^3$$

$$v_{sphere} = \frac{4}{3}\pi * \left(\frac{d_{sphere}}{2}\right)^3 = 1072.53 \text{ cm}^3$$

$$\text{where } d_{sphere} = 12.7 \text{ cm}, r_{anode} = 3.5 \times 10^{-3} \text{ cm}, r_{avalanche} = 0.18 \text{ cm}$$

$$\% \text{ of sphere occupied by avalanche} = \frac{v_{avalanche} - v_{anode}}{v_{sphere} - v_{anode}} = 0.12\%$$

This shows that only 0.12% of the gas cavity volume is occupied by the avalanche for this spherical counter design. As gas gain characteristics are dependent on the ratio of anode to cathode radii and the specific design of the field shaping electrodes employed this could be different for alternative spherical counter designs. For this spherical counter design virtually all of the energy deposited will then be in the electron drift region, where it can undergo the full gas gain. However, as the magnitude of the gas gain increases slightly in the regions outside of  $\pm 0.4r$  the signal amplification does have a slight dependence upon the location of the initial ionization within the gas cavity of this spherical counter.

### 4.3.3 Hemispherical Counter

As the hemispherical counter uses a ball anode in place of a wire the gas gain analysis was for electrons approaching the anode from various directions, ranging from directly above the ball at  $90^\circ$  down to nearly parallel to the cathode base a  $5.625^\circ$ , as shown in Figure 4.7.

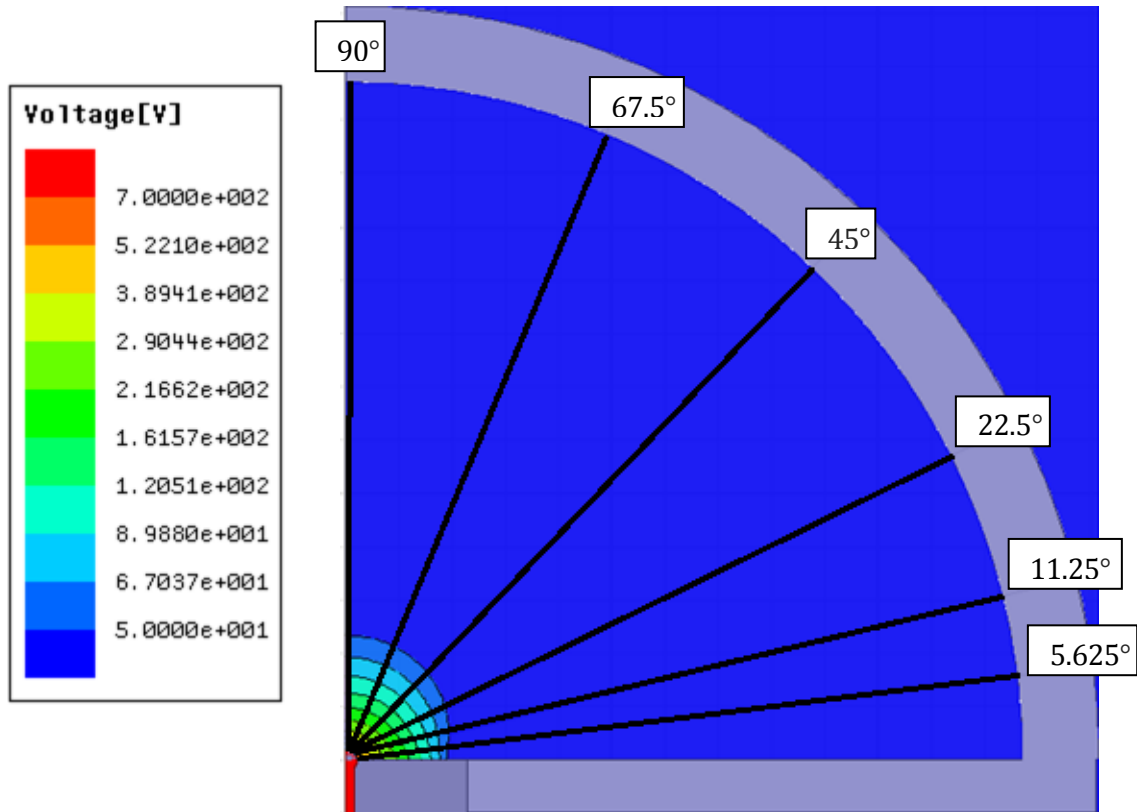


Figure 4.7 – Equipotential lines in the 2.54 cm hemispherical counter ranging from 700 V to 50 V, with the labelled lines highlighting the 6 angles of approach where radial patterns of gas gain were analyzed ( $90^\circ$ ,  $67.5^\circ$ ,  $45^\circ$ ,  $22.5^\circ$ ,  $11.25^\circ$  and  $5.625^\circ$ )

The gain distribution in Figure 4.8 demonstrates that throughout the hemispherical counter the maximum gas gain is uniform and follows the theoretical gain very well. The slight variations in the distribution seen in close proximity to the anode occur only in a very small volume and do not appear to significantly affect the avalanche. The radius of the avalanche ranges from 0.05 cm at  $90^\circ$  to 0.03 cm at  $5.625^\circ$ , with radii generally decreasing slightly as the

angle is reduced. This follows from Figure 4.7 where qualitatively the distances between equipotential lines appear to slightly decrease as the angle decreases.

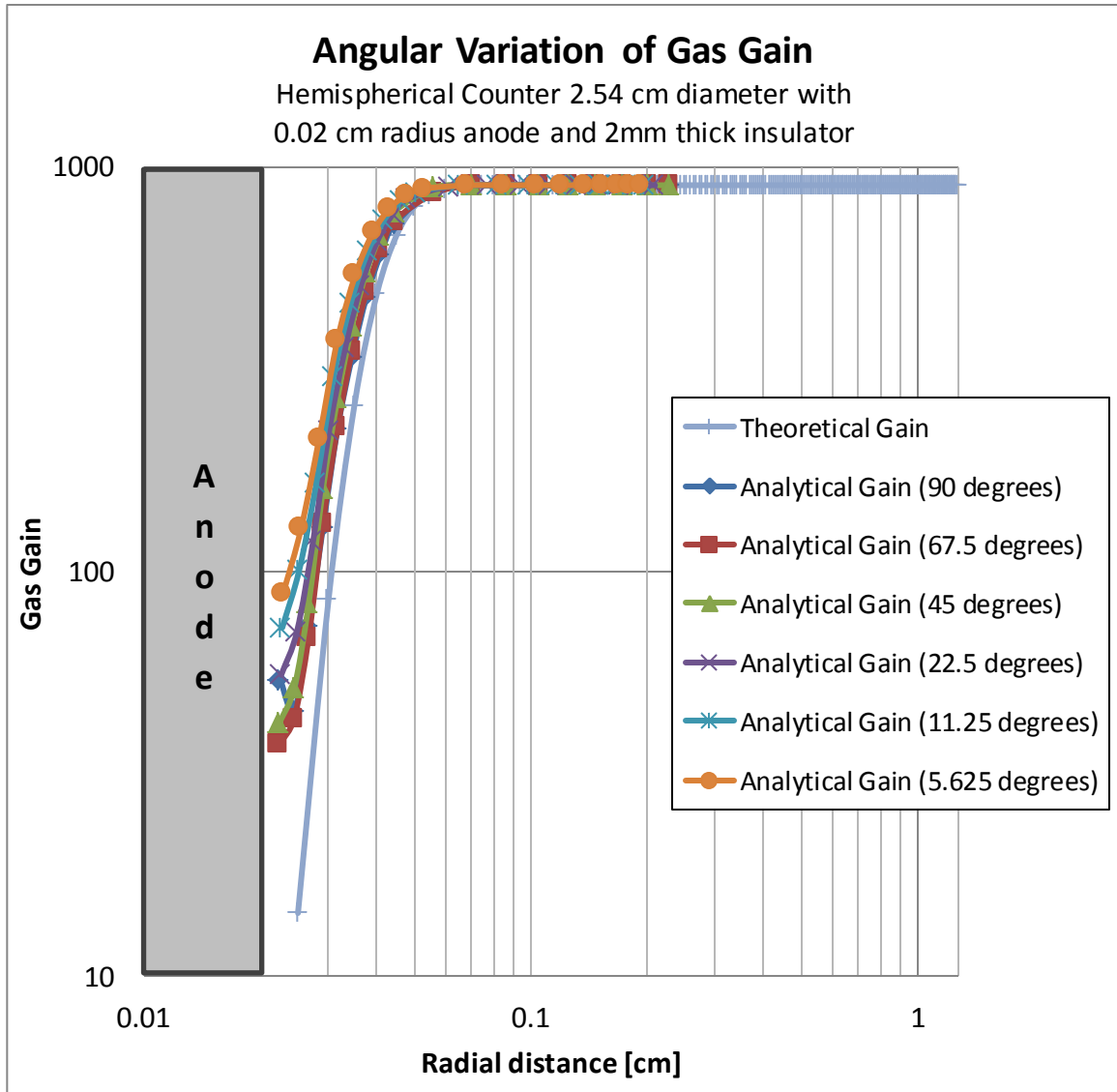


Figure 4.8–Absolute gain as a function of radial distance within the hemispherical counter, angle represents the angle of approaching electrons as shown in Figure 4.7

The mean avalanche radius for the data shown in Figure 4.8 is 0.043 cm, which can be converted to a percentage of the total cavity volume:

$$\text{Percent of cavity occupied by avalanche} = \frac{v_{\text{avalanche}} - v_{\text{anode}}}{v_{\text{hemisphere}} - v_{\text{anode}}} = 0.0035\%$$

$$v_{hemisphere} = \left(\frac{1}{2}\right) \left(\frac{4}{3}\right) \pi r_{hemisphere}^3 = 4.29 \text{ cm}^3$$

$$v_{avalanche} = \left(\frac{1}{2}\right) \left(\frac{4}{3}\right) \pi r_{avalanche}^3 = 1.67 \times 10^{-4} \text{ cm}^3$$

$$v_{anode} = \left(\frac{1}{2}\right) \left(\frac{4}{3}\right) \pi r_{anode}^3 = 1.68 \times 10^{-5} \text{ cm}^3$$

where  $r_{hemisphere} = 1.27 \text{ cm}$ ,  $r_{avalanche} = 0.043 \text{ cm}$ ,  $r_{anode} = 0.02 \text{ cm}$

With the avalanche occupying only  $3.5 \times 10^{-3}\%$  this shows that virtually all of the initial electrons will originate within the electron drift region as it accounts for 99.9965% of the gas cavity. With the small avalanche volume and uniform maximum gain this demonstrates that the electrostatics of the hemispherical counter produce ideal gas gain characteristics.

#### 4.3.4 Comparing Gas Gain in Different Counters

When comparing the analytical gain results it is found that the hemispherical and cylindrical counters closely resemble one another, with both having uniform maximum gain values throughout the counter. The spherical counter however displays significantly increased gain at the ends of the wires, shown in Figure 4.9. However, as it has long been established experimentally that spherical and cylindrical TEPCs do perform very well, this suggests that the deviations from uniformity in maximum gain are acceptable in terms of TEPC performance. This also suggested that the energy deposition patterns which are explored in Chapter 5 must also be a significant factor when evaluating detector performance.

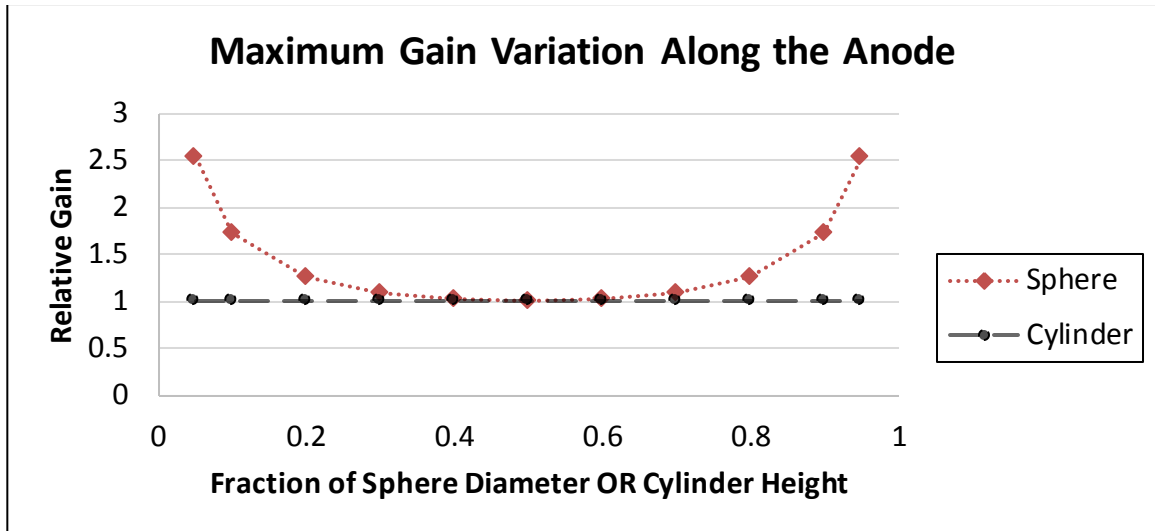


Figure 4.9 – Variation in gas gain along the anode wires of the spherical and cylindrical counters, relative to the gain at the center of the wire

When comparing the fraction of the gas cavity volume occupied by the avalanche within each of the counters in Table 4.1 the spherical and cylindrical counters are of a similar magnitude, while in the hemispherical counter the avalanche occupies a significantly smaller fraction of the cavity. This follows from the fact that the electric field in the spherical and cylindrical counters is proportional to  $1/r$ , whereas the electric field within the hemispherical counter is proportional to  $1/r^2$ . This increases the rate at which the electric field changes within the hemispherical counter, reducing the magnitude of the critical radius. The critical radius is the radius at which the electric field is at the minimum value for producing electron multiplication. For the spherical and cylindrical counters the relative values of this critical radius are within the same magnitude as their electric fields follow the same radial distributions.

Counter Geometry	Volume Occupied by Avalanche	Volume Around Region of Anode with Uniform Gain
Cylinder	0.6%	100%
Sphere	0.12%	-0.4r to 0.4r: 57%
Hemisphere	0.004%	100%

Table 4.1 – Summary of the quantities measuring uniformity of gas gain

In terms of the performance of the hemispherical counter, the small avalanche size and uniform gain magnitude should result in very good energy resolution. These results appear promising; however, as the experimental gas gain analysis along the anode of the 5 *cm* x 0.5 *cm* cylindrical counter, shown in Figure 4.3, found variations up to 6% from this theoretical analysis [53], it would not be implausible for an actual hemispherical counter to also exhibit minor deviations in gain uniformity.

## Chapter 5: Simulating Microdosimetric Experiments

### 5.1 Introduction

As no adequate analytical particle transport solution for microdosimetric interactions exists [67], Monte Carlo simulations are required to simulate neutron interactions within the proposed hemispherical counter as well as the existing cylindrical and spherical TEPCs. These simulations were conducted for two incident neutron fields; monoenergetic 2.5 MeV neutrons and the neutron energy spectrum of  $^{252}\text{Cf}-\text{D}_2\text{O}$  moderated, shown in Figure 5.1 [16]. By including neutrons of very different energy distributions the comparisons between detector responses can also include the effects due to the neutron energy spectrum.

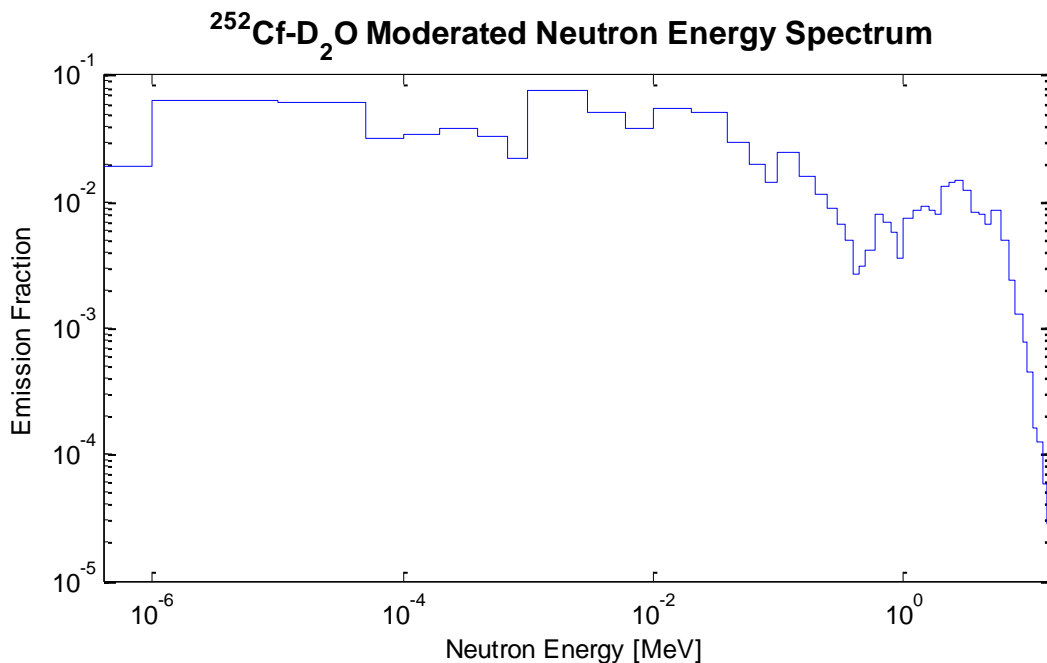


Figure 5.1 – Neutron energy spectrum for a heavy water moderated Californium-252 source, mean neutron energy 0.54 MeV (data from ISO 2000 [16])

The 2.5 MeV neutrons were used to approximate the mean energy of  $^{252}\text{Cf}$ , which is 2.13 MeV and resembles an unmoderated reactor spectrum. The  $^{252}\text{Cf}-\text{D}_2\text{O}$  moderated neutron spectrum ranges from  $4.14 \times 10^{-7}$  MeV to 14 MeV and is regularly used as a surrogate reactor

neutron spectrum during the development of detectors for neutron spectrometry [68]. The benefit of simulating these sources is that they could eventually be used to experimentally validate the simulations as Canadian Nuclear Laboratory (Chalk River, ON) has a  $^{252}\text{Cf-D}_2\text{O}$  moderated source and the D-D neutron generator (P 385, Thermo Scientific™, Waltham, Mass, USA) at UOIT produces quasi-monoenergetic 2.5 MeV neutrons.

The simulations of neutron transport and energy deposition events were conducted using the 3D Particle and Heavy Ion Transport Code System (PHITS) (V.2.24). PHITS was selected to simulate these microdosimetric experiments as it has been benchmarked and demonstrated to be an excellent Monte Carlo transport code for neutron microdosimetry [69]. This was established by Ali [69] with a comparison of experimental data to the results of microdosimetric simulations using three state of the art Monte Carlo transport codes: Monte Carlo N-Particle eXtended (MCNPX) (V. 2.7.E), FLUKA (V. 2011.2), and PHITS (V. 2.24). Although performance was relatively consistent with all simulations matching experimental data reasonably well, PHITS was the only code to adequately produce and transport alpha particles [69]. This is an important factor for this study as the  $^{252}\text{Cf-D}_2\text{O}$  moderated field contains neutrons with energies in excess of 10 MeV which produce alpha particles through inelastic scatter reactions including  $^{16}\text{O}(n,\alpha)^{13}\text{C}$ ,  $^{14}\text{N}(n,\alpha)^{11}\text{B}$ , and  $^{12}\text{C}(n,\alpha)^9\text{Be}$  [23, 30].

When conducting simulations in *event generator mode* PHITS applies the established particle tracking Monte Carlo method. This involves tracking the path and interactions of each source particle, as well as the secondary particles produced during their interactions. In this study all source neutrons were emitted at 90° from plane sources and were transported without interacting in the volume outside of the counter, as this was defined as vacuum. When a neutron reached the detector, the atomic compositions of the TE materials were used to retrieve the appropriate tabulated material and energy based interaction cross sections. These cross sections

were used for determining the probability density functions that were sampled by random numbers to determine the neutron ranges, interaction types, and the scattering angles for neutrons and recoil nuclei, as required. The position and interactions of each neutron were tracked until the neutron was either absorbed by an atom, crossed the defined boundary of the simulated universe, or fell below the defined cut off energy of  $10^{-10}$  MeV.

The secondary charged particles or photons produced by neutron interactions were tracked using the same procedure described for neutrons. The energy deposited by these secondary charged particles as they ionized atoms in the gas cavity was recorded by using the *T-Deposit* tally, which produces a normalized energy deposition distribution in the units of *MeV/source particle*. In Appendix II the full PHITS code and each of the source/detector definitions shown in Figure 5.2 are presented. The PHITS simulation codes used in this work were modified from two sample code provided by Ali, which were for the simulation of the 12.7 cm diameter spherical TEPC being exposed in monoenergetic 14 MeV and unmoderated  $^{252}\text{Cf}$  neutron fields [51]. Following the simulations data analysis was conducted using the MATLAB (V. R2014a) code presented in Appendix III. The MATLAB code in Appendix III contains the reference  $Q^*(10)$  and  $H^*(10)$  values for the poly-energetic  $^{252}\text{Cf}$ -D<sub>2</sub>O moderated field which were determined using a MATLAB code presented in Appendix H of the dissertation by Ali [51].

### 5.1.1 Simulated Experimental Setup

The simulated detectors were introduced in Section 3.4.3.1, and use A-150 used for the walls and propane-based TE gas used to fill the detectors. The detector specifics including wall thickness and gas density were presented in Table 3.2, and the source detector setup is illustrated in Figure 5.2. A 2.54 cm diameter spherical TEPC was included to verify size scaling effects and compare dosimetric performance of the hemisphere to a sphere of equal diameter.

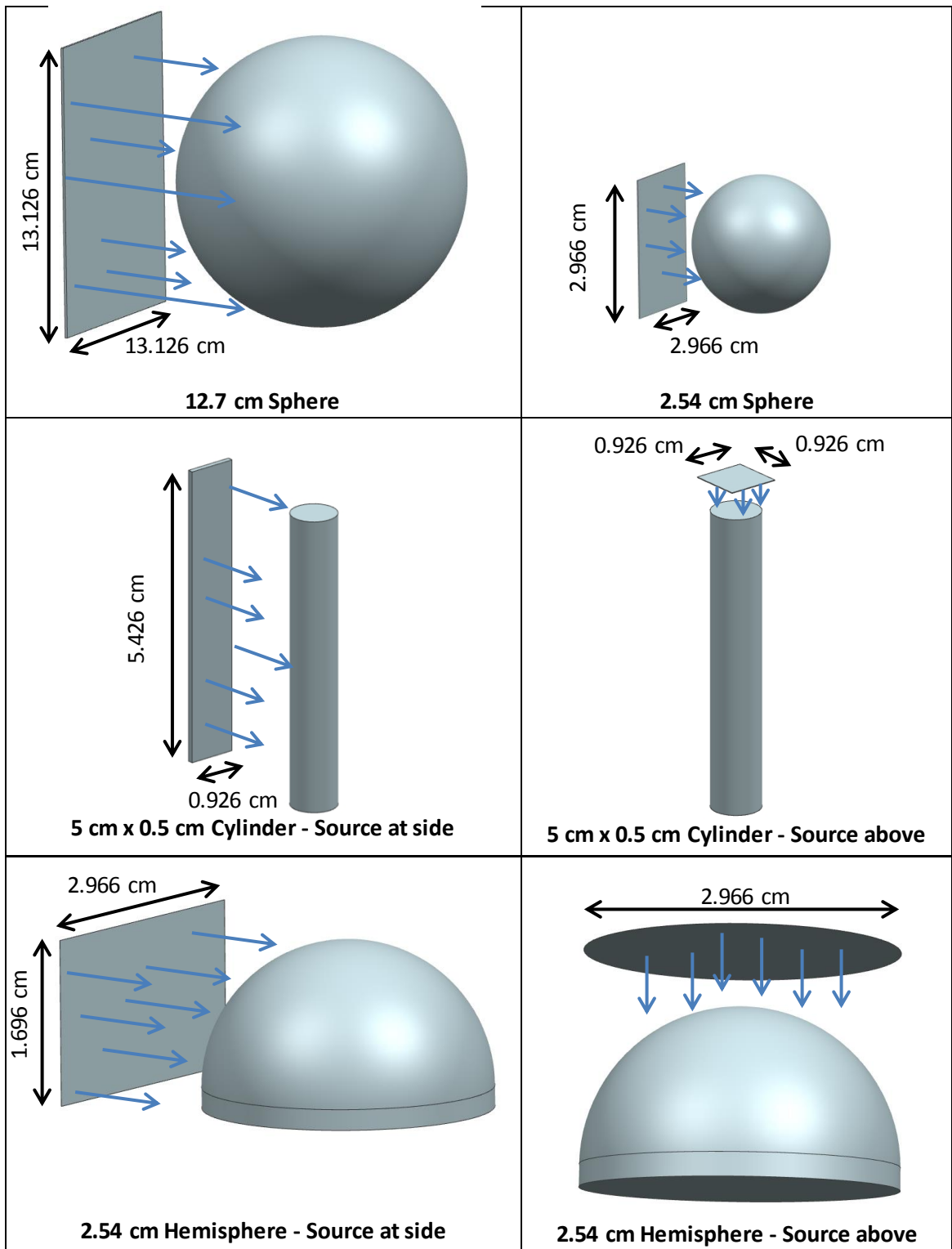


Figure 5.2 – Illustrations of the six source-detector geometries employed for the Monte Carlo simulations in PHITS

### 5.1.2 Analyzed Distributions and Quantities

For each simulated exposure detector performance was evaluated in terms of the microdosimetric distributions and quantities, as well as the response to the operational quantities. As no standard reference values for the microdosimetric results exists, simulated results for the conventionally used 12.7 cm diameter spherical TEPC were used as the standard when evaluating the results from the other counters. As the operational quantities of quality factor,  $Q^*(10)$ , and ambient dose equivalent,  $H^*(10)$ , are reported as a function of neutron energy in ICRP Reports 60 [5] and 74 [10], respectively, this allowed evaluation of the simulated  $\bar{Q}$  and  $H$  values in terms of detector response. The main benefit of analyzing the microdosimetric distributions and quantities in addition to the operational quantities in this study is that microdosimetry provides insight into the causes of variations in detector response. Table 5.1 summarizes the notation used when referring to the dose distribution and the various quantities evaluated in the following sections.

Term	Definition
$y_d(y)$	Lineal energy dose distribution
$\bar{y}_F$	Frequency mean lineal energy [ $keV/\mu m$ ]
$\bar{y}_D$	Dose mean lineal energy [ $keV/\mu m$ ]
$\bar{Q}$	Mean quality factor (determined using ICRP 60 [5] definition)
Q Response	Mean quality factor relative to the ICRP 60 [5] $Q^*(10)$ value
$D/\phi$	Dose per unit neutron fluence [ $Gy \times cm^2/n$ ]
Dose Response	Dose per unit neutron fluence relative to the $D^*(10)$ per unit fluence determined using ICRP 60 [5] and 74 [10] reference $Q^*(10)$ and $H^*(10)$ per unit fluence values
$H/\phi$	Dose equivalent per unit fluence [ $Sv \times cm^2/n$ ]
H Response	Dose equivalent per unit fluence relative to the ICRP 74 [10] reported ambient dose equivalent per unit fluence values
Sensitivity	Number of events or counts per unit of dose equivalent [ $counts/Sv$ ]

Table 5.1 – Definitions for terms used throughout results and discussion of PHITS simulations

The definitions for the dose distribution as well as for the frequency and dose mean lineal energies were presented earlier in Section 2.4. The calculation of the mean quality factor was introduced in Section 2.5 along with the absorbed dose and dose equivalent. When evaluating the mean quality factor, it is compared relative to the ambient quality factor,  $Q^*(10)$ , which is the quality factor in a microscopic volume at a depth of 10 mm within the ICRU sphere exposed in an aligned and expanded plane field [9]. The  $Q^*(10)$  was used to determine the Q Response as:

$$Q \text{ Response} = \frac{\bar{Q}}{Q^*(10)}$$

When evaluating the simulated dose, results were normalized per unit fluence following the convention which allows for comparisons as it makes results independent of intensity. As the ICRP reports the ambient dose equivalent per unit fluence and the ambient quality factor the quotient of these values can be used to define the reference dose,  $D^*(10)$  per unit fluence as:

$$\frac{D^*(10)}{\varphi} = \frac{H^*(10)}{Q^*(10)}$$

This was used to determine the Dose Response as:

$$Dose \text{ Response} = \frac{\frac{D}{\varphi}}{\frac{D^*(10)}{\varphi}}$$

Similarly, the H Response evaluates the simulated dose equivalent per unit fluence relative to the reference ambient dose equivalent per unit fluence, which is determined as:

$$H \text{ Response} = \frac{\frac{H}{\varphi}}{\frac{H^*(10)}{\varphi}}$$

## 5.2 Results and Discussion

### 5.2.1 Comparing Microdosimetric Dose Distributions

The dose distributions in 2.5 MeV neutron fields presented in Figures 5.3 (a) and (b) compare the results of the cylindrical and hemispherical simulations to the reference spherical counter. In this fast neutron field both the cylindrical and hemispherical counters show very prominent directional dependence. The dose distribution of the cylindrical counter in Figure 5.3 (a) shifts towards lower lineal energy values when exposed from the side and higher values when exposed from above. The upwards shift is due to the increased probability of recoil protons having longer path lengths through the gas cavity when the cylinder is exposed from above. These longer mean path lengths cause a higher mean energy deposition per event relative to the shorter track lengths that dominate when the cylindrical counter is exposed from the side. This distribution shift is also visible for the hemisphere in Figure 5.3 (b) as there is a greater probability of longer track lengths in the gas cavity when the hemisphere is exposed from the side. The difference between the two exposures is smaller for the hemisphere, resulting from the reduced directional variation in track lengths for the hemisphere relative to the elongated cylinder.

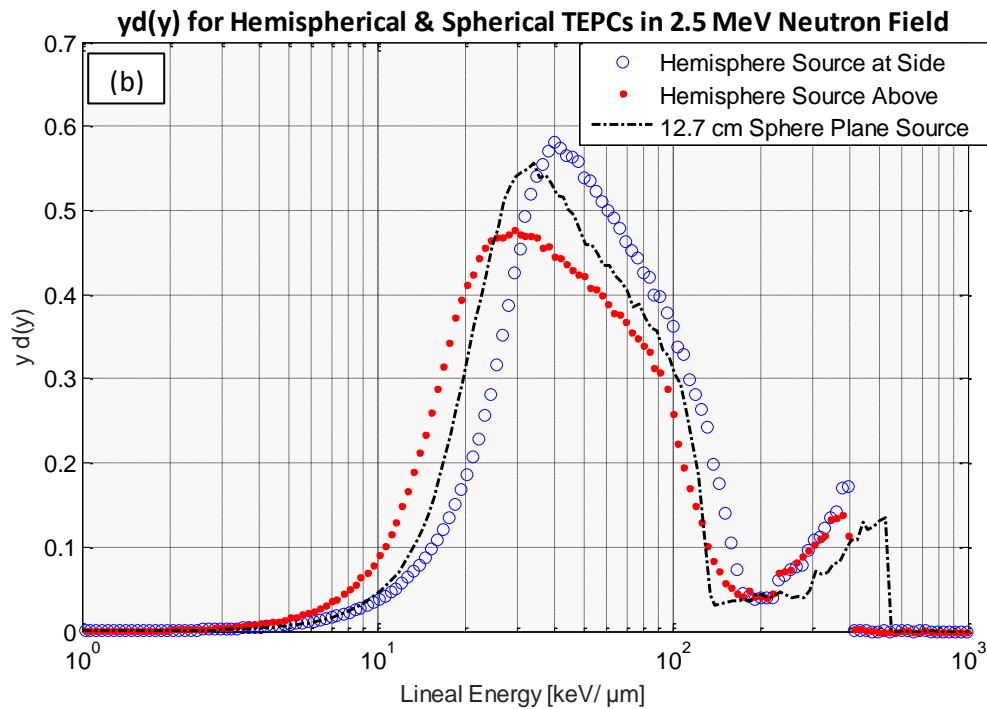
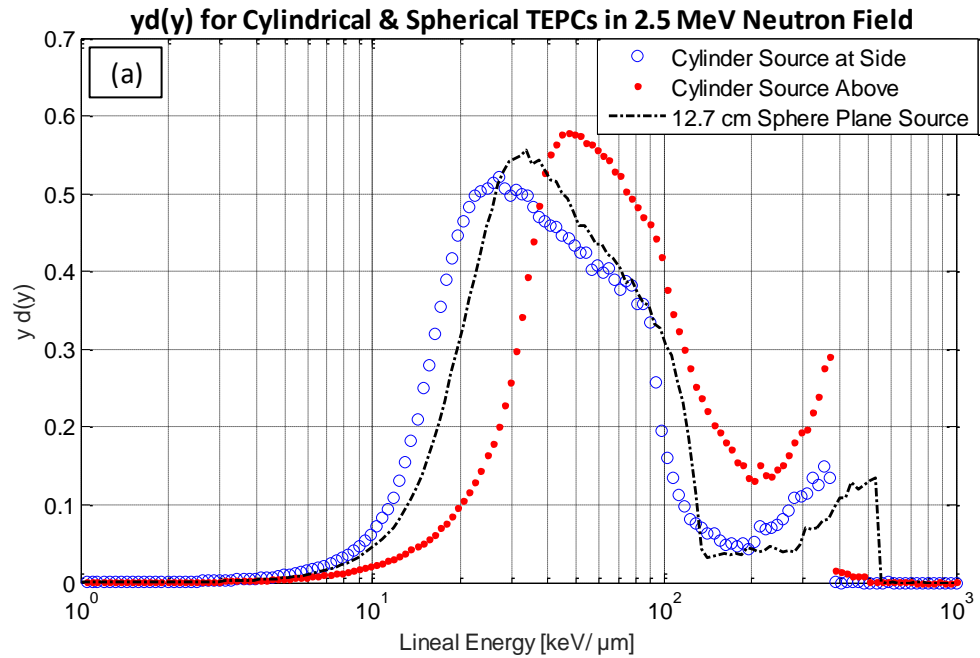


Figure 5.3 – Comparison of dose distributions for 2.5 MeV neutron field (representative of D-D neutron generator) simulated in PHITS with  $2 \times 10^9$  incident neutrons for: (a) Cylindrical and Spherical TEPCs; (b) Hemispherical and Spherical TEPCs

Relative to the simulations above in the 2.5 MeV neutron field, the dose distributions in a  $^{252}\text{Cf}$ -D<sub>2</sub>O moderated neutron field presented in Figures 5.4 (a) and (b) exhibit considerably less directional dependence. The moderated  $^{252}\text{Cf}$  field has a broad neutron energy spectrum and a

much lower mean energy of 0.54 MeV, which leads to much higher neutron cross sections in tissue. At 0.5 MeV the hydrogen elastic scatter cross section is approximately twice that of 2.5 MeV neutrons and at lower energies it is higher still [70]. Similar trends occur for all of the elastic scattering interactions as well as the neutron capture reactions, which are unlikely to occur at all for 2.5 MeV neutrons. One source of isotropically emitted protons is the neutron capture reaction  $^{14}_7\text{N}(n,p)^{14}_6\text{C}$ , however, as this only accounts for about 10% of all capture reactions [30] it is unlikely to dramatically reduce directional dependence. It is more probable that the low energy  $^{252}\text{Cf-D}_2\text{O}$  neutrons do not transfer sufficient energy for recoil protons to have a range greater than  $2\ \mu\text{m}$ ; therefore, even if they are travelling in a direction along the long  $5\ \text{cm}$  Z-axis of the cylindrical counter they cannot deposit more energy than if they were cross along the shorter  $0.5\ \text{cm}$  X or Y-axes from the side. This explanation is supported by considering the energy of recoil protons having a projected range in tissue equal to the cylinders simulated diameter of  $2\ \mu\text{m}$  relative to the energies of the recoil protons produced for exposures in the  $^{252}\text{Cf-D}_2\text{O}$  moderated source. A  $0.175\ \text{MeV}$  proton has a range of  $2.057\ \mu\text{m}$  in unit density tissue (A-150) [71], and while 76% of the neutrons emitted from a  $^{252}\text{Cf-D}_2\text{O}$  moderated source have energies of  $0.15\ \text{MeV}$  or less, on average a neutron will transfer only half of its energy to hydrogen nuclei during elastic scatter. It is therefore very likely that many of the recoil protons have energies well under  $0.175\ \text{MeV}$  and as some of these low energy recoil protons will have ranges less than the mean chord length; making the assumption that they cross the entire gas cavity no longer entirely true. These shorter path lengths through the gas cavity also correspond to a shift in the lineal energy spectrum towards smaller event sizes. The benefit of this is that directional dependence is reduced as many of the recoil protons do not have sufficient energy to have path lengths in excess of  $2\ \mu\text{m}$  which could otherwise occur within the hemispherical and cylindrical counters.

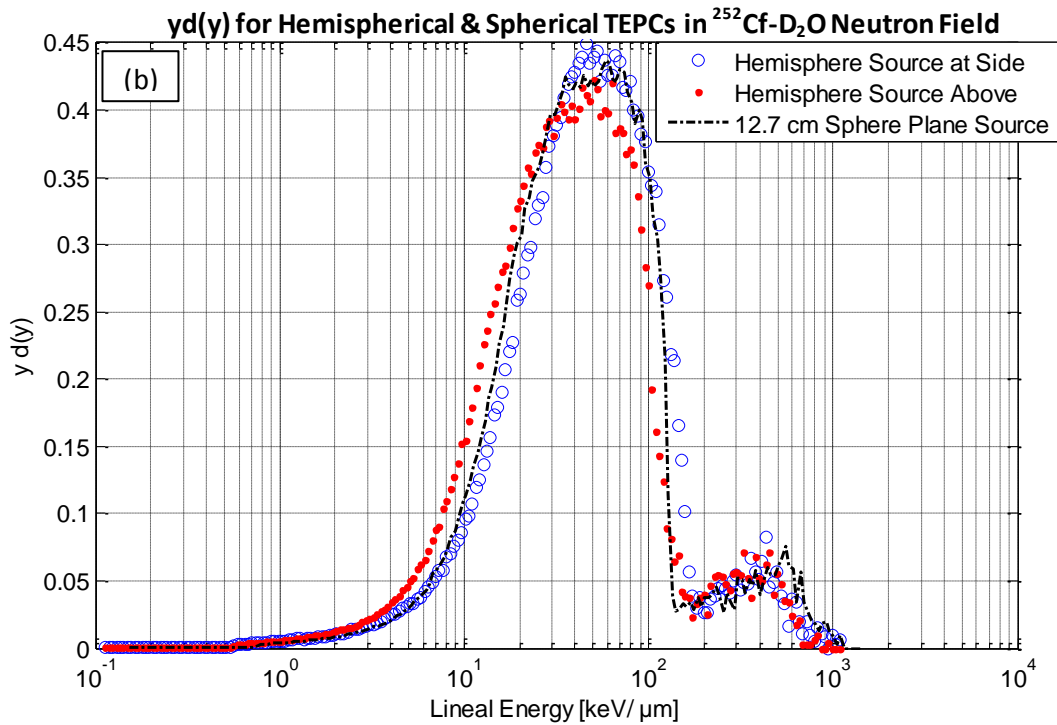
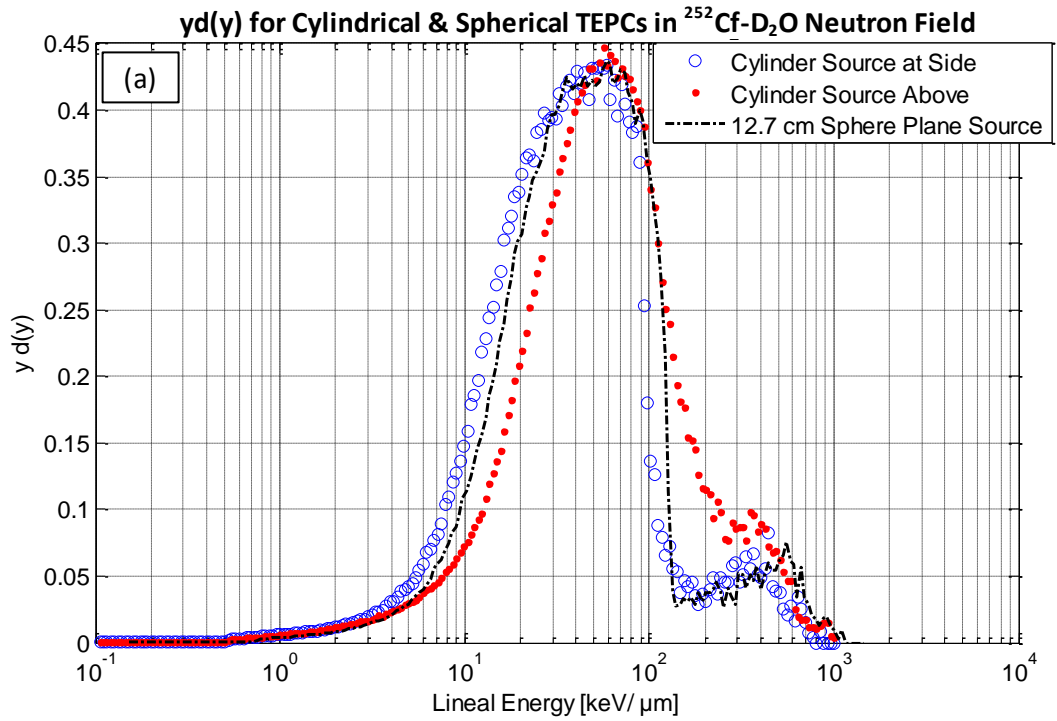


Figure 5.4 – Comparison of dose distributions for  $^{252}\text{Cf-D}_2\text{O}$  moderated neutron field simulated in PHITS with  $2 \times 10^9$  incident neutrons for: (a) Cylindrical and Spherical TEPCs; (b) Hemispherical and Spherical TEPCs

Overall, the dose distributions of the hemispherical counter more closely resemble those of the spherical counter, while the elongation of the cylindrical counter consistently produces a much more prominent shift in the dose distribution to higher lineal energies when it is exposed from above. The upwards shift in the event size washes out the proton edge, which is not ideal as a well-defined proton edge can be used for detector calibration. The qualitative agreement of the hemispherical and spherical counters is encouraging; however, the microdosimetric moments and more importantly the response to the operational quantities determines whether a detector is appropriate for applications in operational health physics.

### 5.2.2 Overall Energy Deposition Patterns and Instrument Response

Since each of the simulated dose distributions has similar features, with two main peaks that represent the proton and heavy recoil nuclei the mean values of the microdosimetric spectra should accurately represent the overall results. The directional dependence and variations due to detector geometry can also be evaluated by comparing the relative responses to the radiation protection quantities. These calculated moments and the detector responses are presented with their associated uncertainties in Tables 5.2 and 5.3 for the 2.5 MeV and  $^{252}\text{Cf}$ - $\text{D}_2\text{O}$  moderated neutron fields, respectively.

Following the trend observed in the dose distributions, directional dependence was much more prominent in the  $\bar{y}_F$  values for the 2.5 MeV neutrons than for the  $^{252}\text{Cf}$ - $\text{D}_2\text{O}$  moderated neutron fields. When the cylindrical counter was exposed from above in the 2.5 MeV field the  $\bar{y}_F$  value was 34% greater than that of the spherical counter, while in the  $^{252}\text{Cf}$ - $\text{D}_2\text{O}$  moderated neutron field the cylinder was only 4% greater. As discussed in Section 5.2.1 the increase when the cylindrical counter is irradiated from above is likely due to recoil proton tracks being more probable along the elongated Z-axis, leading to a greater imparted energy and hence event size  $y$ . This effect is much smaller in the  $^{252}\text{Cf}$ - $\text{D}_2\text{O}$  field as the mean energy of recoil

protons is lower, resulting in most of them having a path length that is equal or less than the mean chord length. The  $\overline{y_F}$  values for the hemispherical counter also agree with this notion as when exposed from the side it overestimated the value of the spherical counter by 11% in 2.5 MeV field and underestimated the sphere by 2% in the  $^{252}\text{Cf-D}_2\text{O}$  moderated neutron field.

The  $\overline{y_D}$  values of the hemispherical and cylindrical counters displayed much more consistent variations from the spherical counter between the two neutron fields. The cylindrical counter's  $\overline{y_D}$  values exhibited the largest over and under-responses relative to the spherical counter, with average differences ranging from +19% to -22% in both fields when exposed from above and the side, respectively. Comparing the hemispherical versus the spherical counter, the mean  $\overline{y_D}$  differences in both fields ranged from -19% to +2% when exposed from above and the side, respectively. Comparing the variation of both counters relative to the spherical counter, the hemispherical counter displayed about half the amount of variation of the cylindrical counter.

The mean quality factor values were evaluated in terms of Q responses, which are relative to the ICRP 60 [5] reference  $Q^*(10)$  values of 12.27 and 9.62 for the 2.5 MeV and  $^{252}\text{Cf-D}_2\text{O}$  moderated neutron fields, respectively. The Q response values for each of the simulated exposures are shown graphically in Figure 5.5.

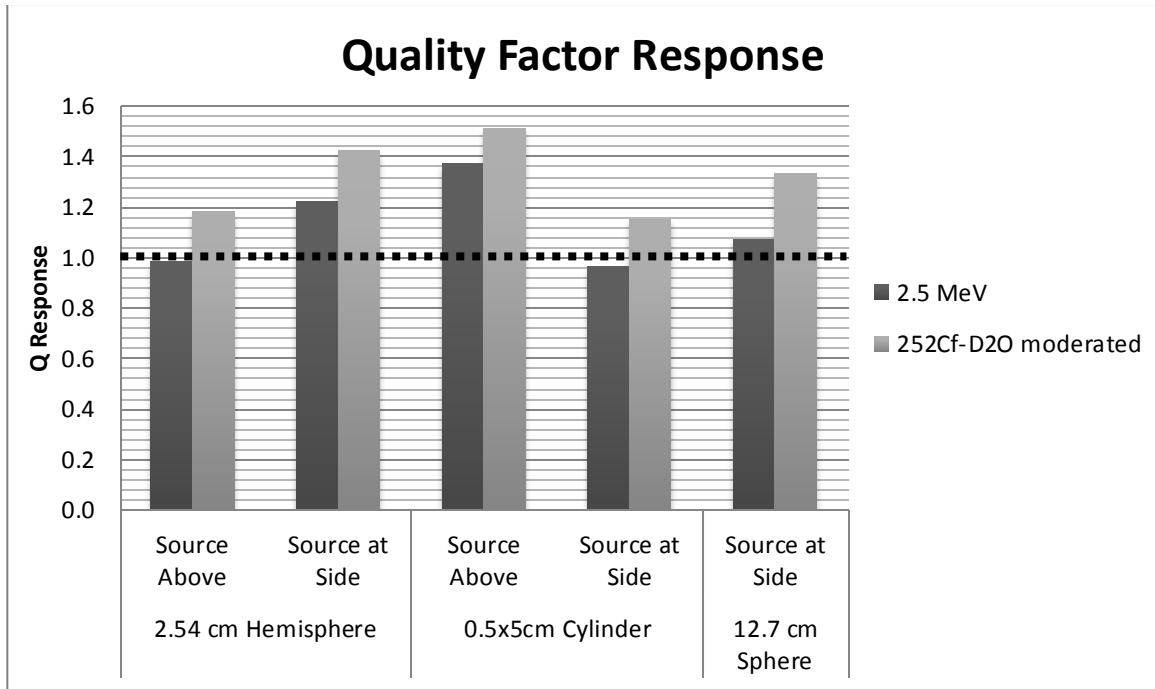


Figure 5.5 – Simulated Q Response values relative to the ICRP 60 [5]  $Q^*(10)$  values of 12.27 and 9.62 for 2.5 MeV and heavy water moderated Californium neutron fields, respectively

Overall the quality factor responses for all the simulated TEPCs were good at not underestimating the quality factor. In some cases, considerable over-responses were found, with the greatest over-response being 1.51 for the cylindrical counter when exposed to the  $^{252}\text{Cf-D}_2\text{O}$  moderated neutron field from above. Although the spherical counter appeared to have the best overall quality factor response, the response of 1.33 in the  $^{252}\text{Cf-D}_2\text{O}$  moderated neutron field shows that it is not perfect. Quality factor response was generally better in the 2.5 MeV neutron field, where the response values for the hemispherical counter exposed from above and the cylindrical counter exposed from the side were 0.98 and 0.96, respectively.

For many exposures an over-response to the quality factor appeared to be associated with an under-response to the absorbed dose. This is seen in the Dose Response presented in Figure 5.6 somewhat for 2.5 MeV neutrons, but mainly for the heavy water moderated Californium fields.

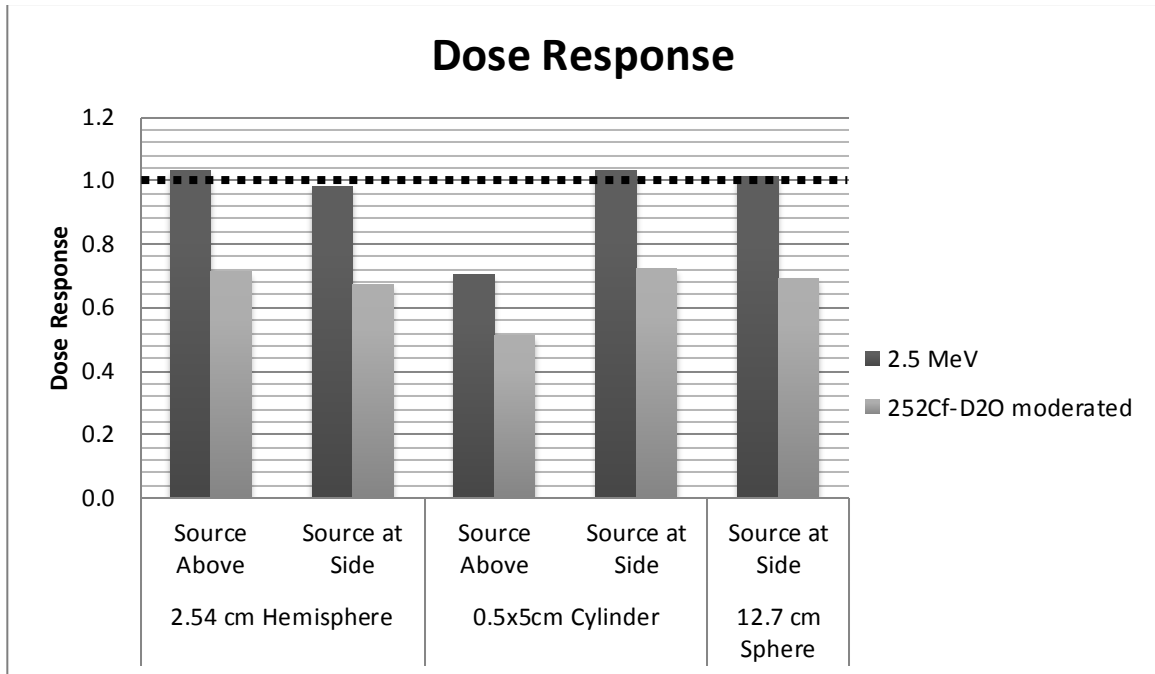


Figure 5.6 – Simulated Dose Response values relative to the ICRP 60/74 [5, 10]  $D^*(10)$  values of  $3.39 \times 10^{-11} \text{ Gy} * \text{cm}^2 / \text{n}$  and  $1.12 \times 10^{-11} \text{ Gy} * \text{cm}^2 / \text{n}$  for 2.5 MeV and heavy water moderated Californium neutron fields, respectively

All of the simulated counters under-respond to the dose in the  $^{252}\text{Cf-D}_2\text{O}$  moderated neutron field. The most apparent case was for the cylindrical counter exposed from above, where in the 2.5 MeV and  $^{252}\text{Cf-D}_2\text{O}$  moderated neutron fields the quality factors responses were 1.37 and 1.51 and dose responses were 0.70 and 0.51, respectively. The dose responses for all of the other exposures in the 2.5 MeV fields were very good, all within the range of 0.98 to 1.03.

As explained in the Chapter 1 with Figure 1.4 the  $H^*(10)$  response of TEPCs varies significantly as a function of neutron energy. In the higher energy range of the 2.5 MeV neutron field the  $H^*(10)$  response was reported as being within 10% using spherical TEPCs [1]. The  $^{252}\text{Cf-D}_2\text{O}$  moderated neutron spectrum contains the neutrons with energies around  $5 \times 10^{-4} \text{ MeV}$  where TEPC response is at its lowest at  $2 \times 10^{-2}$  [1]. Despite this, all of the simulated  $H^*(10)$  responses shown in Figure 5.7 were within the range of 0.77 to 0.95 and 0.97 to 1.19 in the  $^{252}\text{Cf-D}_2\text{O}$  moderated and 2.5 MeV neutron fields, respectively. It was unexpected that despite the

large deviations in the responses to the quality factor and dose when the cylindrical counter was exposed from above in the 2.5 MeV field it still shows a good overall H\*(10) response.

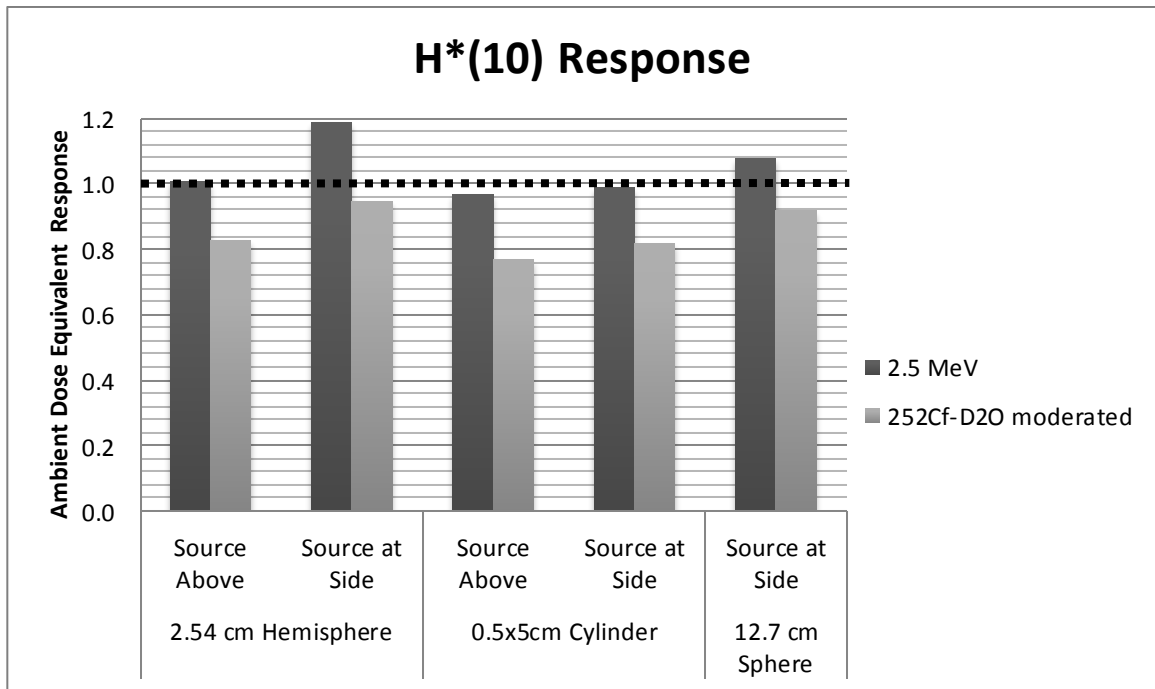


Figure 5.7 – Simulated H\*(10) Response values relative to the ICRP 74 [10] H\*(10) values of  $4.16 \times 10^{-10} Sv * cm^2/n$  and  $1.08 \times 10^{-10} Sv * cm^2/n$  for 2.5 MeV and heavy water moderated Californium neutron fields, respectively

On the basis of detector sensitivity, the 12.7 cm spherical counter has previously been deemed to have sufficient sensitivity for applications in radiation protection [3]. The smaller counters would be used as elements in an METEPC where total sensitivity would be the sum of the sensitivity of each individual element. This is done in order to increase the sensitivity per unit volume relative to the single element sphere. What was observed from the simulations is that the sensitivity of the hemispherical counter appears to be less directionally dependent relative to the cylindrical counter. The sensitivity of the hemispherical counter exposed from above is also a very close match to the 2.54 cm sphere, despite the use of a gas cavity only half the size. Although this first hemispherical design would likely be scaled down for use in an METEPC, the number of 2.54 cm diameter hemispherical elements required to match the sensitivity of the

12.7 cm diameter spherical counter would be in the range of 30 elements. The scaling of the hemispherical counter is not believed to be an issue as was demonstrated that the spherical counters response was unchanged when scaled down by a factor of 5, from 12.7 cm to 2.54 cm in diameter.

Simulations similar to those conducted in this work have also been conducted by Ali [51] and were presented in his dissertation. The work of Ali included microdosimetric simulations conducted in PHITS using  $^{252}\text{Cf-D}_2\text{O}$  moderated neutron fields for two detectors similar to those used in this study. The work of Ali included the same reference 12.7 cm diameter spherical TEPC and the full 61 element METEPC which uses the single cylindrical element that was analyzed in this study. As anticipated the results of Ali for both the spherical counter and the METEPC are comparable to those of this work, with all microdosimetric and response quantities being very close to one another. Slight differences were observed when comparing the full METEPC to the single cylindrical element as the METEPC has a greater amount of wall material. When exposed from the side (+X and +Z in the notation of Ali) both the dose and  $H^*(10)$  responses of the METEPC were slightly less than that of the single cylindrical counter as neutrons were moderated more by the METEPCs walls. However, when the METEPC was exposed from above (+Y in the notation of Ali), the increased wall material produced a slightly higher dose and  $H^*(10)$  response relative to the single cylindrical counter. These minor differences go away when the response is averaged out over both exposure conditions, demonstrating that the overall responses are very similar for both the single element cylindrical counter and the METEPC. This shows that although the increased amount wall material when scaling from a single element up to an METEPC can slightly affect directional dependence, it did not significantly alter the overall response performance of the counter.

TEPC Type	2.54 cm Hemisphere		0.5 cm x 5 cm Cylinder		12.7 cm Sphere	2.54 cm Sphere
Location of Plane Source	Above	Side	Above	Side	Side	Side
$\bar{y}_F$ [keV/ $\mu$ m]	28.59 $\pm$ 0.6	39.26 $\pm$ 0.08	49.55 $\pm$ 0.07	29.91 $\pm$ 0.07	35.13 $\pm$ 0.07	35.04 $\pm$ 0.07
$\bar{y}_D$ [keV/ $\mu$ m]	63.48 $\pm$ 0.34	76.54 $\pm$ 0.33	95.57 $\pm$ 0.27	60.78 $\pm$ 0.35	75.90 $\pm$ 0.44	76.52 $\pm$ 0.50
$\bar{Q}$	12.05 $\pm$ 0.04	14.94 $\pm$ 0.04	16.82 $\pm$ 0.03	11.79 $\pm$ 0.04	13.14 $\pm$ 0.04	13.11 $\pm$ 0.04
Q Response ( $\bar{Q}/Q^*(10)$ )	0.98 $\pm$ 0.003	1.22 $\pm$ 0.003	1.37 $\pm$ 0.003	0.96 $\pm$ 0.003	1.07 $\pm$ 0.003	1.07 $\pm$ 0.003
Dose per unit fluence [Gy*cm <sup>2</sup> /n]	3.49 x 10 <sup>-11</sup> $\pm$ 1 x 10 <sup>-14</sup>	3.32 x 10 <sup>-11</sup> $\pm$ 8 x 10 <sup>-15</sup>	2.39 x 10 <sup>-11</sup> $\pm$ 4 x 10 <sup>-15</sup>	3.5 x 10 <sup>-11</sup> $\pm$ 1 x 10 <sup>-14</sup>	3.4 x 10 <sup>-11</sup> $\pm$ 9 x 10 <sup>-15</sup>	3.47 x 10 <sup>-11</sup> $\pm$ 1 x 10 <sup>-14</sup>
Dose Response	1.03 $\pm$ 3 x 10 <sup>-4</sup>	0.98 $\pm$ 2 x 10 <sup>-4</sup>	0.70 $\pm$ 1 x 10 <sup>-4</sup>	1.03 $\pm$ 3 x 10 <sup>-4</sup>	1.01 $\pm$ 3 x 10 <sup>-4</sup>	1.02 $\pm$ 3 x 10 <sup>-4</sup>
Dose equivalent per unit fluence [Sv*cm <sup>2</sup> /n]	4.20 x 10 <sup>-10</sup> $\pm$ 1 x 10 <sup>-12</sup>	4.97 x 10 <sup>-10</sup> $\pm$ 1 x 10 <sup>-12</sup>	4.02 x 10 <sup>-10</sup> $\pm$ 7 x 10 <sup>-13</sup>	4.13 x 10 <sup>-10</sup> $\pm$ 1 x 10 <sup>-12</sup>	4.51 x 10 <sup>-10</sup> $\pm$ 1 x 10 <sup>-12</sup>	4.55 x 10 <sup>-10</sup> $\pm$ 1 x 10 <sup>-12</sup>
H*(10) Response	1.01 $\pm$ 0.003	1.19 $\pm$ 0.003	0.97 $\pm$ 0.002	0.990 $\pm$ 0.003	1.08 $\pm$ 0.003	1.09 $\pm$ 0.003
Sensitivity [counts/ $\mu$ Sv]	6.88 $\pm$ 0.39	4.04 $\pm$ 0.22	1.54 $\pm$ 0.07	3.64 $\pm$ 0.22	172.28 $\pm$ 9.19	6.91 $\pm$ 0.39

Table 5.2 – Microdosimetric moments and operational response values from Monte Carlo microdosimetric simulations conducted with PHITS using 2.5 MeV neutrons

TEPC Type	2.54 cm Hemisphere		0.5 cm x 5 cm Cylinder		12.7 cm Sphere	2.54 cm Sphere
Location of Plane Source	Above	Side	Above	Side	Side	Side
$\bar{y}_F$ [keV/ $\mu$ m]	19.49 $\pm$ 0.08	23.96 $\pm$ 0.09	25.48 $\pm$ 0.07	19.54 $\pm$ 0.09	24.48 $\pm$ 0.09	24.48 $\pm$ 0.10
$\bar{y}_D$ [keV/ $\mu$ m]	62.96 $\pm$ 0.96	74.74 $\pm$ 1.02	89.64 $\pm$ 0.74	61.38 $\pm$ 1.10	76.77 $\pm$ 1.27	76.36 $\pm$ 1.42
$\bar{Q}$	11.34 $\pm$ 0.07	13.65 $\pm$ 0.08	14.54 $\pm$ 0.06	11.06 $\pm$ 0.08	12.75 $\pm$ 0.07	12.69 $\pm$ 0.08
Q Response ( $\bar{Q}/Q^*(10)$ )	1.18 $\pm$ 0.008	1.42 $\pm$ 0.008	1.51 $\pm$ 0.006	1.15 $\pm$ 0.008	1.33 $\pm$ 0.008	1.32 $\pm$ 0.008
Dose per unit fluence [Gy*cm <sup>2</sup> /n]	7.91 $\times 10^{-12}$ $\pm 9 \times 10^{-15}$	7.52 $\times 10^{-12}$ $\pm 7 \times 10^{-15}$	5.68 $\times 10^{-12}$ $\pm 3 \times 10^{-15}$	8.02 $\times 10^{-12}$ $\pm 1 \times 10^{-14}$	7.76 $\times 10^{-12}$ $\pm 8 \times 10^{-15}$	7.81 $\times 10^{-12}$ $\pm 1 \times 10^{-14}$
Dose Response	0.71 $\pm 8 \times 10^{-4}$	0.67 $\pm 7 \times 10^{-4}$	0.51 $\pm 3 \times 10^{-4}$	0.72 $\pm 9 \times 10^{-4}$	0.69 $\pm 7 \times 10^{-4}$	0.67 $\pm 9 \times 10^{-4}$
Dose equivalent per unit fluence [Sv*cm <sup>2</sup> /n]	8.97 $\times 10^{-11}$ $\pm 6 \times 10^{-13}$	1.03 $\times 10^{-10}$ $\pm 6 \times 10^{-13}$	8.26 $\times 10^{-11}$ $\pm 3 \times 10^{-13}$	8.87 $\times 10^{-11}$ $\pm 7 \times 10^{-13}$	9.90 $\times 10^{-11}$ $\pm 6 \times 10^{-13}$	9.92 $\times 10^{-11}$ $\pm 6 \times 10^{-13}$
H*(10) Response	0.83 $\pm$ 0.005	0.95 $\pm$ 0.005	0.77 $\pm$ 0.003	0.82 $\pm$ 0.006	0.92 $\pm$ 0.005	0.92 $\pm$ 0.006
Sensitivity [counts/ $\mu$ Sv]	10.72 $\pm$ 0.88	7.25 $\pm$ 0.56	3.47 $\pm$ 0.22	5.94 $\pm$ 0.52	254.76 $\pm$ 19.80	10.21 $\pm$ 0.84

Table 5.3 – Microdosimetric moments and operational response values from Monte Carlo microdosimetric simulations conducted with PHITS using <sup>252</sup>Cf-D<sub>2</sub>O moderated neutron fields

The overall ranking of the TEPC designs on the basis of the tabulated results is difficult as performance is both directional and field dependent in different ways for different counters. Table 5.4 summarizes the results of Tables 5.2 and 5.3 by using the overall mean responses averaged over both source-detector geometries, except for the spherical counter where only the results of the reference 12.7 cm diameter sphere exposed from the side were used. The mean response was used for this analysis as an attempt at better estimating the true detector responses as actual reactor neutron fields are generally not aligned and incident upon the detector from a single direction. These exposure conditions were used during simulations in order to increase simulation efficiency for events of relatively low probability. The simulated exposure conditions also do match the ICRU 51 [9] description of the aligned and expanded neutron field to be used for  $H^*(10)$  measurements.

Neutron Field	Response Quantity	Detector Rank	Over/Under Response
2.5 MeV	$\bar{Q}$	(1) Sphere (2) Hemisphere (3) Cylinder	+7% +10% +17%
	$H^*(10)$	(1) Cylinder (2) Sphere (3) Hemisphere	-2% +8% +10%
$^{252}\text{Cf-D}_2\text{O}$ moderated	$\bar{Q}$	(1) Hemisphere (2) Cylinder (3) Sphere	+30% +33% +33%
	$H^*(10)$	(1) Sphere (2) Hemisphere (3) Cylinder	-8% -11% -21%

Table 5.4 – Ranked overall mean detector response values with percent over (+) and under (-) response

Table 5.4 demonstrates that in fast neutron fields the spherical TEPC is the better quality factor monitor, likely due to its lower relative variance in chord length relative to the other geometries. In the lower energy  $^{252}\text{Cf-D}_2\text{O}$  moderated field the spherical counter response accuracy decreases and aligns with the response of the other counters. This suggests that at low energies variations of the field

dominate, with some of the recoil nuclei not having sufficient energy to cross the gas cavity. It is possible that use of simulated sites of a smaller size, such as  $1\ \mu\text{m}$ , may improve counter response for low energy neutrons. In terms of their overall Q response the hemispherical counter performs marginally better than the cylindrical counter, as anticipated from the reduced variance in the distributions of the chord length of the hemisphere relative to this elongated cylinder.

The overall mean  $H^*(10)$  responses for the spherical and hemispherical counters in both fields are within the range of 0.89 to 1.1, which is approximately  $\pm 10\%$ . While the cylindrical counter's  $H^*(10)$  responses also ranges approximately 20%, ranging from 0.98 to 0.795, all of the simulated response values are  $<1$  for the cylindrical counter. For radiation protection applications the over-response of the hemisphere in higher energy fields is more acceptable than the under-response of the cylinder in lower energy neutron fields. For an unknown neutron field there appears to be a greater likelihood of  $H^*(10)$  underestimation using the cylinder, making either the spherical or hemispherical geometries the better choices of design. In addition to this, the mean overall response of the hemispherical counter appears to be within  $\pm 4\%$  of the reference spherical counter for all the overall mean Q and  $H^*(10)$  responses as well as for each individual dose response value. Based on this, the hemisphere appears to be a reasonable substitute for the current reference spherical geometry in terms of neutron monitoring. These dosimetric response results from the Monte Carlo simulations coupled with the conclusions drawn from the gas gain analysis demonstrate that the hemispherical counter has definite potential as the detecting element of a neutron monitoring device.

## Chapter 6: Conclusion and Recommendations for Further Work

Chapter 1 of this thesis began by demonstrating that TEPCs have the potential to increase the accuracy of neutron dosimetry in reactor fields, while also decreasing the size and weight of instrumentation. This was established by analyzing the  $H^*(10)$  responses of TEPCs and flux monitors along with experimentally measured neutron energy spectra and their corresponding  $H^*(10)$  distributions in reactor fields. The  $H^*(10)$  response for TEPCs was shown to be comparable to the bulky moderator-based flux monitors currently used in the neutron energy ranges that deposit an average of 91% of the  $H^*(10)$  [4]. Although flux monitors have better overall responses their accuracy is dependent on how well the calibration neutron field resembles the actual reactor field. This is a challenge for two reasons: reactor neutron fields vary depending on the specific location within the reactor building, and the neutron energy distributions in these fields are difficult to replicate. In practice this can result in a TEPC with equal or inferior response to a flux monitor producing more accurate workplace results as an improperly calibrated flux monitor can significantly over or under-respond in the determination of the  $H^*(10)$ .

Subsequently, Chapter 2 provided the experimental microdosimetry background relevant to the application of TEPCs for neutron monitoring. This included TEPC basics such as the concepts of cavity theory, tissue equivalence, scaling of microscopic sites, radiation interactions with tissue. This chapter concluded with an introduction to the microdosimetric distributions and quantities and their use for calculating the operational quantities.

Chapter 3 began with a historical review of the various TEPC designs used for neutron monitoring and dosimetry. This included issues that have been encountered with current TEPC and especially METEPC designs. The focus was on METEPCs as they would be an ideal portable instrument for neutron monitoring if the current issues limiting their practicality could be resolved. This thesis

attempted to address these issues which are largely due to the anode wires. The installation of an anode wire is very challenging, requiring a great deal of skill and precision. Once installed the wires produce end effects requiring the use of additional electrodes, and also produce microphonic noise when the counter is moved or when there is audible noise in the vicinity of the counter. A novel wire-less anode METEPC element design was proposed as a potential solution to these issues. This design consists of a hemispherical cathode shell and a concentric ball anode. The basic design concept was optimized through electrostatic analysis in ANSYS Maxwell (V. 14.0) with the objective of finding anode, cathode and insulator dimensions that produce a uniform electric field distribution and a high magnitude reduced electric field. Chapter 3 concluded by presenting the specifications and geometric sources of variance for the proposed hemispherical counter as well as current spherical and cylindrical counter designs.

Gas gain distributions within each of the three counters were characterized in Chapter 4 by first analyzing the potential distributions within each of the counters in ANSYS Maxwell, and then solving the Townsend gas gain equation throughout each gas cavity using the potential values obtained from the numerical analysis conducted using Maxwell. This analysis found that the magnitude of the gas gain varied by a factor of 2.5 along the anode wire of the spherical counter. This was not the case for either the hemispherical or cylindrical counters, which exhibited completely uniform gas gain regardless of an electron's initial position within their respective gas cavities. The avalanche region of the hemispherical counter occupies only 0.0004% of the entire gas cavity volume, whereas in the cylindrical and spherical counters the avalanche occupies 0.6% and 0.12% of the total gas cavity volume, respectively. Through this analysis it was demonstrated that, in terms of gas gain, hemispherical counters have ideal characteristics as they possess uniform gas gain which is contained within a very small avalanche volume.

Since the performance of a TEPC is dependent not only upon electron multiplication, but also on the patterns in energy deposition, in Chapter 5 the results from the microdosimetry simulations conducted using the 3D Monte Carlo tool PHITS (V. 2.24) were presented. These simulations used both mono-energetic 2.5 MeV neutrons and the  $^{252}\text{Cf-D}_2\text{O}$  moderated neutron spectrum as source terms to enable relative detector responses to be evaluated for low and high neutron energies within the range of those found in reactor fields. Through this analysis it was found that the microdosimetric response of the hemispherical counter better matched the reference spherical TEPC than the results of the elongated cylindrical counter. Although the hemispherical counter did exhibit some directional dependence, it was significantly reduced in comparison to the cylindrical counter. Similar trends were seen when evaluating the detectors for the response to the operation quantities of quality factor and ambient dose equivalent. As detector responses were found to be dependent on the neutron field caution in drawing conclusions is required, but for the analyzed fields the hemispherical counter appears to be a better choice of detector geometry as the cylindrical counter tends to under-respond to  $\text{H}^*(10)$  in the predominately lower neutron energies of the  $^{252}\text{Cf-D}_2\text{O}$  moderated neutron field. As the performance of the hemispherical counter more closely resembles the spherical TEPC in the two simulated fields it is likely that it would continue to do so in other fields; this could be confirmed by conducting additional simulations for neutron fields covering a wider range of energy distributions.

When gas gain and energy deposition are considered together the hemispherical counter fulfills the defined technical objectives for a new design of a TEPC having:

- A wire-less anode
- $\text{H}^*(10)$  response and microdosimetric distributions comparable to the current standard spherical TEPC design
- Significantly reduced directional dependence relative to the elongated cylindrical TEPC
- Gas multiplication independent of initial ionization location

The main recommendation for future work would be to validate the simulated results by the construction and experimental testing of a hemispherical counter alongside the commercial Far West 5SW-LET counter which the analyzed 12.7 *cm* spherical counter was modelled after. The specific details regarding recommendations for the design of the prototype hemispherical counter were presented in Section 3.4.3.2. A hemispherical counter with the dimensions of this prototype design was also simulated in PHITS; results are included in Appendix IV, demonstrating that this design should also perform similarly to the simulated hemispherical counter in Chapter 5. As such it is suggested that this design is used for the manufacturing of a prototype hemispherical counter. If the experimental performance of the prototype hemispherical counter agrees with the simulations and analysis this should be followed by the use of hemispherical elements in a METEPC. For this, the hemispherical elements could be reduced in size to increase the ratio of sensitivity to volume as the Monte Carlo simulations of both 12.7 *cm* and 2.54 *cm* diameter spherical counters given in Chapter 5 demonstrated that the response of a detector is independent of size scaling. The process of designing an METEPC with hemispherical elements would require further Monte Carlo simulations to test and optimize the design, determining the appropriate hemisphere size, number of elements and minimizing the influence of the METEPCs increased wall material on directional dependence.

## Appendix I: Determining Gas Constants for Gas Gain Calculations

When calculating the gas gain the appropriate gas constants  $A$  and  $B$  must be employed. These were defined in Section 4.2 and were determined for this work using the experimental data of Waker [28], which was conducted with propane based TE gas similar to this study. As the experimental data from Waker [28] presents the gas constants as a function of reduced electric field, the reduced electric field must be determined within each of the counters. The reduced electric field is calculated for a cylindrical counter using [72]:

$$S(r) = \frac{E(r)}{p} = \frac{V_{a \rightarrow b}}{pr * \ln\left(\frac{b}{a}\right)} \quad (\text{A.1})$$

where  $E(r)$  is the electric field at radius  $r$ ,  $p$  is the gas pressure,  $V_{a \rightarrow b}$  the voltage difference between radii  $a$  and  $b$  which represent the anode and cathode, respectively. When determining  $A$  and  $B$  the reduced electric field on the surface of the anode is used, where  $r = a$ . The determination of the gas constants  $A$  and  $B$  was as follows:

In the case of the  $0.5 \text{ cm} \times 5 \text{ cm}$  cylindrical counter where  $V = 750 \text{ V}$ ,  $p = 169.31 \text{ torr}$ ,  $a = 0.0025 \text{ cm}$  and  $b = 0.25 \text{ cm}$ , using Equation A.1 the reduced electric field at the surface of the anode was found to be  $384.77 \text{ V} * \text{torr}^{-1} * \text{cm}^{-1}$ . This corresponds to the values  $25.1 \text{ torr}^{-1} * \text{cm}^{-1}$  and  $306 \text{ V} * \text{torr}^{-1} * \text{cm}^{-1}$  for  $A$  and  $B$  respectively [28].

For the  $12.7 \text{ cm}$  diameter spherical counter where  $V = 700 \text{ V}$ ,  $p = 6.67 \text{ torr}$ ,  $a = 0.0035 \text{ cm}$  and  $b = 5.19 \text{ cm}$ . This value of  $b$  is based on Equation 4.17 which transforms a spherical cathode radius to the radius of a cylindrical cathode with equivalent gas gain. Using these values in Equation A.1 the reduced electric field at the surface of the spherical counter's anode was then found to be  $4068.54 \text{ V} * \text{torr}^{-1} * \text{cm}^{-1}$ . This corresponds to  $A$  and  $B$  values of  $44.4 \text{ torr}^{-1} * \text{cm}^{-1}$  and  $571 \text{ V} * \text{torr}^{-1} * \text{cm}^{-1}$  respectively [28].

For the hemispherical detector operating at  $V = 750 \text{ V}$ ,  $p = 66.71 \text{ torr}$ ,  $a = 0.04 \text{ cm}$  and  $b = 1.27 \text{ cm}$  the reduced electric field at the surface of the anode was found to be  $778.30 \text{ V} * \text{torr}^{-1} * \text{cm}^{-1}$ . In the case of the hemispherical counter the electric field value used for determining the reduced electric field was obtained from the Maxwell analysis instead of from the analytical equation (4.19) as the analytical equation gives a slightly lower value as it does not include the base of the hemisphere. The corresponding  $A$  and  $B$  values for the hemisphere are then  $15.7 \text{ torr}^{-1} * \text{cm}^{-1}$  and  $321 \text{ V} * \text{torr}^{-1} * \text{cm}^{-1}$  respectively [28].

## Appendix II: PHITS Input Files

In this appendix the complete input file used for simulating the 12.7 cm diameter spherical counter with a 2.5 MeV neutron source will first be presented. This is followed by all of the various source and detector geometries that were used along with the *Parameters, Material, Importance* and *T-deposit* sections presented for the 12.7 cm diameter spherical counter.

### File Name: FITEPC\_DD\_SPHERE.in

```
[ Title ]
Irradiation of 12.7 cm (5 inch) TEPC with monoenergetic 2.5 MeV Neutron Source

[ Parameters ]
icntl = 0
rseed = -1
maxcas = 2000000000 $Number of source particles
maxbch = 1
file(6) = phits_FITEPC.out
file(7) = c:/phits/data/xsdir.jnd
file(14) = c:/phits/data/trxcd.dat
emin(1) = 1.0E-3 $Minimum PROTON transport kinetic energy
emin(2) = 1.0E-10 $Minimum NEUTRON transport kinetic energy
dmax(2) = 20 $Maximum NEUTRON kinetic energy to use data library
emin(12) = 1.0E-3 $Minimum ELECTRON transport kinetic energy
dmax(12) = 1.0E3 $Maximum ELECTRON kinetic energy to use data library
emin(13) = 1.0E-3 $Minimum POSITRON transport kinetic energy
dmax(13) = 1.0E3 $Maximum POSITRON kinetic energy to use data library
emin(14) = 1.0E-3 $Minimum PHOTON transport energy
dmax(14) = 1.0E3 $Maximum PHOTON energy to use data library
emin(18) = 1.0E-3 $Minimum ALPHA transport kinetic energy
emin(19) = 1.0E-3 $Minimum NUCLEUS transport kinetic energy
nedisp = 1 $Landau Vavilov energy straggling for charged particle transport
e-mode = 1

[ Source ]
s-type = 2 $this is for monoenergetic
proj = neutron
x0 = -7
x1 = -7
y0 = -6.563
y1 = 6.563
z0 = -6.563
z1 = 6.563
dir = 0
phi = 0
```

```
e0 = 2.5 $neutron energy

[Material]
MAT[ 1 ] $Propane-based Tissue Equivalent Gas
1H -10.3
6000 -56.9
14N -3.5
16O -29.3
MAT[ 2 ] $Shonka A-150 Tissue Equivalent Plastic
1H -10.1
6000 -77.6
14N -3.5
16O -5.2
19F -1.7

[Surface]
1 SO 6.35
2 SO 6.563
3 RPP -40 40 -40 40 -40 40

[Cell]
1 1 -1.5748E-5 -1
2 2 -1.127 -2 1
3 0 -3 2
4 -1 3

[Importance]
part = neutron proton alpha nucleus electron positron
reg imp
1 1
2 1
3 1

[T - Deposit]
mesh = reg
reg = 1
part = (proton alpha nucleus electron positron) proton alpha nucleus (electron positron)
e-type = 3
ne = 201
emin = 0.000197
emax = 1.97
output = deposit
unit = 3
axis = eng
file = deposit_FITEPC.dat
[END]
```

When conducting the 2.5 MeV neutron simulations for the other counters the following were used for the Source, Surface and Cell sections. The sources used for both exposures from the side and above are presented, following the illustration in Figure 5.2.

**Input file sections for hemispherical counter exposed to 2.5 MeV source from the side and above:**

```
[ S o u r c e ] $ for exposure from the side:
s-type= 2 $ monoenergetic
proj= neutron
x0= -5
x1= -5
y0= -1.483
y1= 1.483
z0= -0.213
z1= 1.483
dir= 0
phi= 0
e0= 2.5

[ S o u r c e ] $ for exposure from above:
s-type= 1
proj= neutron
x0= 0
y0= 0
z0= 4
z1= 4
r0= 1.483
dir = -1
phi = 0
e0 = 2.5

[ S u r f a c e ]
1 SO 1.27
2 SO 1.483
3 RPP -10.0 10.0 -10.0 10.0 -10.0 10.0
4 RCC 0.0 0.0 0.0 0.0 0.0 -0.213 1.483 $cylinder base
5 RPP -2.0 2.0 -2.0 2.0 0.0 2.0 $this is for limiting the sphere
6 RPP -2.0 2.0 -2.0 2.0 -0.213 2.0

[ C e l l ]
1 1 -1.5748E-4 -1 -5 $inside of 1 where it intersects with 5
2 2 -1.127 (-5 -2 1):-4 $inside intersection of 1, 2, 5 (hemisphere)
3 0 -3 #2 #1 $vacuum outside of the detector (fill void with vacuum)
4 -1 3
```

**Input file sections for cylindrical counter exposed to 2.5 MeV source from the side and above:**

[ S o u r c e ] \$ for exposure from the side:

s-type = 2 \$this is for monoenergetic

proj = neutron

\$ these are for from the side:

x0 = -3

x1 = -3

y0 = -0.463

y1 = 0.463

z0 = -0.213

z1 = 5.213

dir = 0

phi = 0

[ S o u r c e ] \$ for exposure from above:

s-type = 2 \$this is for monoenergetic

proj = neutron

x0 = -0.463

x1 = 0.463

y0 = -0.463

y1 = 0.463

z0 = 6

z1 = 6

dir = -1

phi = 0

e0=2.5

[ S u r f a c e ]

1 RCC 0.0 0.0 0.0 0.0 0.0 5 0.25 \$cylinder(smaller one)

2 RCC 0.0 0.0 -0.213 0.0 0.0 5.426 0.463 \$cylinder(outer one)

3 RPP -10.0 10.0 -10.0 10.0 -10.0 10.0 \$outer limit box

[ C e l l ]

1 1 -4E-4 -1 \$inside of 1

2 2 -1.127 -2 1 \$inside intersection of 1, 2, 5 (hemisphere)

3 0 -3 2 \$vacuum outside of the detector (fill void with vacuum)

4 -1 3

**Input file sections for 2.54 cm diameter spherical counter exposed to 2.5 MeV source from the side:**

```
[ Source ]
s-type = 2 $this is for monoenergetic
proj = neutron
x0 = -7
x1 = -7
y0 = -1.483
y1 = 1.483
z0 = -1.483
z1 = 1.483
dir = 0
phi = 0
e0 = 2.5 $neutron energy
```

```
[ Surface ]
1 SO 1.27
2 SO 1.483
3 RPP -40 40 -40 40 -40 40
```

```
[ Cell ]
1 1 -7.874E-5 -1
2 2 -1.127 -2 1
3 0 -3 2
4 -1 3
```

A change to the Source section was required to conduct simulations for the  $^{252}\text{Cf-D}_2\text{O}$  moderated field; however, the source dimensions (x, y, z, r) and particle directions (dir, phi) were unchanged. The two required changes were from a monoenergetic source, 's-type=2', to a probability distribution, 's-type=5', where the following ISO 2000 [16] defined  $^{252}\text{Cf-D}_2\text{O}$  moderated neutron probability distribution replaced the line 'e0=2.5':

```
e-type = 1
ne = 52
4.14E-07      1.90E-02
1.00E-06      6.31E-02
1.00E-05      6.04E-02
5.00E-05      3.17E-02
1.00E-04      3.41E-02
2.00E-04      3.82E-02
4.00E-04      3.28E-02
7.00E-04      2.24E-02
1.00E-03      7.56E-02
3.00E-03      5.09E-02
```

6.00E-03	3.79E-02
1.00E-02	5.47E-02
2.00E-02	5.12E-02
4.00E-02	2.96E-02
6.00E-02	2.00E-02
8.00E-02	1.45E-02
1.00E-01	2.47E-02
1.50E-01	1.59E-02
2.00E-01	1.14E-02
2.50E-01	8.90E-03
3.00E-01	6.57E-03
3.50E-01	4.89E-03
4.00E-01	2.65E-03
4.50E-01	3.14E-03
5.00E-01	4.20E-03
5.50E-01	4.12E-03
6.00E-01	7.83E-03
7.00E-01	6.78E-03
8.00E-01	5.75E-03
9.00E-01	3.57E-03
1.00E+00	7.48E-03
1.20E+00	8.43E-03
1.40E+00	9.13E-03
1.60E+00	8.55E-03
1.80E+00	8.07E-03
2.00E+00	1.34E-02
2.30E+00	1.45E-02
2.60E+00	1.49E-02
3.00E+00	1.23E-02
3.50E+00	8.19E-03
4.00E+00	8.10E-03
4.50E+00	6.54E-03
5.00E+00	8.70E-03
6.00E+00	4.93E-03
7.00E+00	2.42E-03
8.00E+00	1.30E-03
9.00E+00	7.66E-04
1.00E+01	4.43E-04
1.10E+01	1.62E-04
1.20E+01	1.24E-04
1.30E+01	5.93E-05
1.40E+01	2.83E-05
1.50E+01	

## Appendix III: MATLAB Data Analysis

The data produced by the PHITS simulations was analyzed using a MATLAB (V. R2014a) code based on one provided by Ali [51]. This analysis includes determination of the microdosimetric moments, the  $y_d(y)$  distribution and the radiation protection quantities along with their responses as well as all appropriate error analysis. These calculations are based on the formulae provided in Sections 2.4.2-2.6. The following MATLAB code is for the analysis of the 12.7 cm diameter spherical counter exposed to 2.5 MeV neutrons. All of the appropriate information required in the section labelled *Step (2)* for altering the code for analyzing results of the other detectors and their various exposure conditions is provided in the comments. In order to run the MATLAB analysis the data from PHITS simulation must be in the same folder at the MATLAB file and in a 3 column text file named "Data.txt" where the first two columns contain the lower and upper energy limits of the energy bin in MeV and the third column represents the probability of a count in the given energy bin *normalized per source neutron*.

```
%=====
% Name: David Broughton (modified from a code written by Fawaz Ali)
% Purpose of MATLAB Code:   Process the pulse height tallies produced by
%                           PHITS to calculate response parameters of the
%                           TEPC after being irradiated by an expanded and
%                           aligned neutron source
%=====

%-----
% Step (1) Import PHITS Pulse Height Tally
%-----
%The first and second column of the following matrix will store the energy
%deposition bin endpoints and the third column will store the average bin
%counts
DATA_FROM_PHITS = dlmread('Data.txt','');

%-----
% Step (2) Declare Required Information
%-----

%%%%%%%%%% CHECK THE FOLLOWING SECTION BEFORE RUNNING THE CODE
Source_Neutrons = 2E9; %           %Number of Source Neutrons Incident on TEPC
Source_Surface_Area = (2*6.563)^2; %Surface area of plane source [cm^2]
% SA for each geometry (all in [cm]):
% 12.7 cm sphere: (2*6.563)^2
% 2.54 cm sphere: (2*1.483)^2
% 5 cm x 0.5 cm cylinder from SIDE: (0.926)*(5.426)
%                               cylinder from ABOVE: (0.926)^2
```

```

% 2.54 cm hemisphere SIDE: (1.696)*(2.966)
% hemisphere ABOVE: (pi)*(2.966/2)^2

l_bar = 1.33; %Mean Chord Length of Simulated Site [um]
% l_bar for each detector:
% sphere: 1.33
% cylinder: 1.91
% hemisphere: 1.78

rho = 1.58*10^-5; %TE Gas Density in each Element (unit: g/cc)
% rho for each detector (simulating 2 um diameter sites, 2 um radius for
% hemisphere (all in [g/cm^3]):
% 12.7 cm sphere: 1.58*10^-5
% 2.54 cm sphere: 0.985*10^-5
% 5 cm x 0.5 cm cylinder: 40.1*10^-5
% 2.54 cm hemisphere: 1.97*10^-5

%The next step calculates the total mass of TE gas in all elements (unit:
%kg)
m_gas = (rho/1000)*1072.5;
% rho for each detector (simulating 2 um diameter sites, 2 um radius for
% hemisphere
%calculated in [kg] by multiplying density and volume:
% 12.7 cm sphere: (rho/1000)*1072.5
% 2.54 cm sphere: (rho/1000)*68.64
% 5 cm x 0.5 cm cylinder: (rho/1000)*0.98
% 2.54 cm hemisphere: (rho/1000)*34.32

%The variables are for the ambient dose equivalent and the Q*(10) for the
%radiation field
H_Star = 4.17*10^-10;
%The reference H*(10) [Sv *cm^2/n] values are:
% 4.17*10^-10 for 2.5 MeV neutrons
% 1.077929942*10^-10 for 252-Cf-D20 moderated neutrons

Q_Star = 12.27; %Q*(10) for Radiation Field
%The reference Q*(10) values are:
% 12.27 for 2.5 MeV neutrons
% 9.62225 for 252-Cf-D20 moderated neutrons

%%% DON'T CHANGE ANYTHING BEYOND HERE
%%%%%%%%%%%%%%%%%%%%%%%%%%%%%%%%%%%%%%%%%%%%%%%%%%%%%%%%%%%%%%%%%%%%%%%%

linlog_bin_width = 0.04605; %Logarithmic Lineal Energy Bin Width [keV/um]
Fluence = Source_Neutrons/Source_Surface_Area;
%Fluence of Neutron Source [n/cm^2]

%-----
% Step (3) Populate Lineal Energy vs. Counts Matrix
%-----
%The first column of the matrix below stores the lineal energy midpoint of
%each bin, the second column stores the corresponding counts, and the third
%column stores the associated standard deviation of the counts
DATA = zeros(length(DATA_FROM_PHITS), 3);

```

```

%The loop below populates the first column

for i = 1:1:length(DATA_FROM_PHITS)
    DATA(i,1) = 0.5*(DATA_FROM_PHITS(i,1) +
DATA_FROM_PHITS(i,2))*(1000/l_bar);
%finds midpoint of the energy bin and converts to [keV/um]
end

%The second column will now be populated (this is the frequency of events)
DATA(:,2) = DATA_FROM_PHITS(:,3).*Source_Neutrons;
%number of events in each bin

%The loop below populates the third column

for j = 1:1:length(DATA)
    DATA(j,3) = sqrt(DATA(j,2)); %sqrt of number of events (error)
end

%-----
% Step (4) Calculate the Frequency and Dose Mean Linear Energy and their
% associated Standard Deviations
%-----
%The following two quantities will store the frequency and dose mean linear
%energies and their respective standard deviations respectively
yF = 0;
yD = 0;
yf_SD = 0;
yd_SD = 0;

%The following variables will assist in the calculation of quantities and
%their standard deviations (e and f are used for Q_bar)
a = 0; %sum((y_i)^4*f(y_i))
b = 0; %sum((y_i)^2*f(y_i))
c = 0; %sum(y_i*f(y_i))
d = 0; %sum(f(y_i))
e = 0; %sum((Q(y_i))^2*(y_i)^2*f(y_i))
f = 0; %sum(Q(y_i)*y_i*f(y_i))

%The loop below will calculate the value of yF and yD

for k = 1:1:length(DATA)
    a = a + (DATA(k,1)^4*DATA(k,2));
    b = b + (DATA(k,1)^2*DATA(k,2));
    c = c + (DATA(k,1)*DATA(k,2));
    d = d + (DATA(k,2));
end

yF = c/d; %Value of yF
yD = b/c; %Value of yD

yf_SD = yF*sqrt(((sqrt(b)/c)^2) + ((sqrt(d)/d)^2)); %Standard Deviation of
yF
yd_SD = yD*sqrt(((sqrt(a)/b)^2) + ((sqrt(b)/c)^2)); %Standard Deviation of
yD

```

```

%-----
% Step (5) Calculate the Dose Distribution
%-----
%The first column of the matrix below stores the lineal energy midpoint of
%each bin, the second column stores the value of yd(y) for the bin, and the
%third column stores the associated standard deviation

ydy = zeros(length(DATA),3);

ydy(:,1) = DATA(:,1); %Load in the lineal energy bin midpoints

%The loop below calculates the value of yd(y) for each bin and the
%associated standard deviation

for m = 1:length(DATA)
    ydy(m,2) = (DATA(m,1)*DATA(m,2))/(c*linlog_bin_width);
    ydy(m,3) =
ydy(m,2)*sqrt(((DATA(m,1)*DATA(m,3))/(DATA(m,1)*DATA(m,2)))^2 +
((sqrt(c)/c)^2));
end

%Plot the Total and Partial Dose Distributions
semilogx(ydy(:,1),ydy(:,2),'b*')

%-----
% Step (6) Calculate dose per unit fluence
%-----
%The following variables will store the total absorbed dose and its
%standard deviation
Dose_per_unit_fluence = 0;
Dose_per_unit_fluence_SD = 0;

%The following loop will calculate the value of the above variables

for i3 = 1:length(DATA)
    Dose_per_unit_fluence = Dose_per_unit_fluence +
(DATA(i3,1)*DATA(i3,2)*1_bar/1000);
    Dose_per_unit_fluence_SD = Dose_per_unit_fluence_SD +
(DATA(i3,1)^2*DATA(i3,3));
end
    Dose_per_unit_fluence_SD = 1.60218*10^-
13*sqrt(Dose_per_unit_fluence_SD)*1_bar/1000/(m_gas*Fluence);

    Dose_per_unit_fluence = 1.60218*10^-
13*Dose_per_unit_fluence/(m_gas*Fluence);

    Response_Dose = Dose_per_unit_fluence/(H_Star/Q_Star);
    Response_Dose_SD = Dose_per_unit_fluence_SD/(H_Star/Q_Star);

%-----
% Step (7) Calculate the Mean Quality Factor and associated Standard
%          Deviation as well as the Quality Factor Response and associated
%          Standard Deviation

```

```

%-----
%The following variable will store the value of the numerator of the mean
%quality factor expression and the associated standard deviation
%respectively;

%The following loop will calculate the value of the above variables

for n = 1:1:length(DATA)

    %For y < 10 keV/um
    if (DATA(n,1) < 10)
        f = f + (1*DATA(n,1)*DATA(n,2));
        e = e + (1^2*DATA(n,1)^2*DATA(n,2));

    %For 10 <= y <= 100 keV/um
    elseif ((DATA(n,1) >= 10) && (DATA(n,1) <= 100))
        f = f + (((0.32*DATA(n,1)) - 2.2)*DATA(n,1)*DATA(n,2));
        e = e + (((0.32*DATA(n,1)) - 2.2)^2*DATA(n,1)^2*DATA(n,2));

    %For y > 100 keV/um
    else
        f = f + ((300/sqrt(DATA(n,1)))*DATA(n,1)*DATA(n,2));
        e = e + ((300/sqrt(DATA(n,1)))^2*DATA(n,1)^2*DATA(n,2));

    end
end

Q_bar = f/c;           %Mean Quality Factor
Q_bar_SD = Q_bar*sqrt(((sqrt(e)/f)^2) + ((sqrt(b)/c)^2));
%Standard Deviation of Mean Quality Factor

Response_Q = Q_bar/Q_Star; %Quality Factor Response
Response_Q_SD = Response_Q*Q_bar_SD/Q_bar; %Stdev of Quality Factor Response

%-----
% Step (8) Calculate the Dose Equivalent Response of the TEPC and the
% associated Standard Deviation
%-----

Dose_Equivalent_per_unit_fluence = 0;
Dose_Equivalent_per_unit_fluence_SD = 0;

Dose_Equivalent_per_unit_fluence = Dose_per_unit_fluence*Q_bar;

Dose_Equivalent_per_unit_fluence_SD =
Dose_Equivalent_per_unit_fluence*sqrt((Q_bar_SD/Q_bar)^2+(Dose_per_unit_fluence_SD/Dose_per_unit_fluence)^2);
%The calculation below quantifies the dose equivalent response of the
%counter for the radiation field and the associated standard deviation

Response_H = Dose_Equivalent_per_unit_fluence/H_Star;

```

```

Response_H_SD =
Response_H*sqrt(((Dose_Equivalent_per_unit_fluence_SD/Dose_Equivalent_per_unit_fluence)^2));

%-----
% Step (9) Calculate the TEPCs Sensitivity (counts per unit dose equivalent)
% and associated Standard deviation
%-----
Sensitivity =
sum(DATA(:,2))/(Q_bar*Dose_per_unit_fluence*Fluence);%Sensitivity of TEPC

Sensitivity_SD = Sensitivity*(sqrt((sqrt(sum(DATA(:,2)))/sum(DATA(:,2))^2 +
(Dose_Equivalent_per_unit_fluence_SD/Dose_Equivalent_per_unit_fluence)^2)));
%Standard Deviation of TEPC Sensitivity

```

## Appendix IV: Results of Monte Carlo Energy Deposition Simulations in the Proposed Design for Manufacturing of a Prototype Hemispherical Counter

In order to assess the effects of the modification for the hemispherical counter design proposed in Figure 3.10 (a) to (d) a series of simulations were conducted in PHITS using a hemispherical counter with the thicker 5 mm base. The results from these simulations are shown alongside the hemispherical counter's original results from Tables 5.2 and 5.3 in Tables A.1 and A.2, for 2.5 MeV and  $^{252}\text{Cf-D}_2\text{O}$  moderated neutron fields respectively.

Tables A.1 and A.2 demonstrate that the change of thickness from 2.13 mm to 5 mm for the base of the hemispherical counter does not have a significant effect on energy deposition patterns for either the high energy 2.5 MeV neutrons or the  $^{252}\text{Cf-D}_2\text{O}$  moderated neutron field with a lower mean energy. This suggests that the design proposed here should be an appropriate means for constructing an actual hemispherical TEPC for experimental measurements in neutron fields.

TEPC Type	(a) 2.54 cm Hemisphere with 2.13 mm thick walls		(b) 2.54 cm Hemisphere 5 mm thick base	
	Above	Side	Above	Side
Location of Plane Source	Above	Side	Above	Side
$\bar{y}_F$ [keV/ $\mu\text{m}$ ]	$28.59 \pm 0.06$	$39.26 \pm 0.08$	$28.63 \pm 0.06$	$38.99 \pm 0.08$
$\bar{y}_D$ [keV/ $\mu\text{m}$ ]	$63.48 \pm 0.34$	$76.54 \pm 0.33$	$63.66 \pm 0.34$	$75.79 \pm 0.35$
$\bar{Q}$	$12.05 \pm 0.04$	$14.94 \pm 0.04$	$12.08 \pm 0.04$	$14.92 \pm 0.04$
Q Response ( $\bar{Q}/Q^*(10)$ )	$0.98 \pm 0.003$	$1.22 \pm 0.003$	$0.98 \pm 0.003$	$1.22 \pm 0.003$
Dose per unit fluence [Gy*cm <sup>2</sup> /n]	$3.49 \times 10^{-11} \pm 1 \times 10^{-14}$	$3.32 \times 10^{-11} \pm 8 \times 10^{-15}$	$3.51 \times 10^{-11} \pm 1 \times 10^{-14}$	$3.39 \times 10^{-11} \pm 8 \times 10^{-15}$
Dose Response	$1.03 \pm 3 \times 10^{-4}$	$0.98 \pm 2 \times 10^{-4}$	$1.03 \pm 2.87 \times 10^{-4}$	$0.9972 \pm 3 \times 10^{-4}$
Dose equivalent per unit fluence [Sv*cm <sup>2</sup> /n]	$4.20 \times 10^{-10} \pm 1 \times 10^{-12}$	$4.97 \times 10^{-10} \pm 1 \times 10^{-12}$	$4.24 \times 10^{-10} \pm 1.27 \times 10^{-12}$	$5.06 \times 10^{-10} \pm 1 \times 10^{-12}$
H*(10) Response	$1.01 \pm 0.003$	$1.19 \pm 0.003$	$1.02 \pm 0.003$	$1.21 \pm 0.003$
Sensitivity [counts/ $\mu\text{Sv}$ ]	$6.88 \pm 0.39$	$4.04 \pm 0.22$	$6.86 \pm 0.39$	$4.08 \pm 0.2$

Table A.1 – Results of Monte Carlo simulations in PHITS using 2.5 MeV neutron fields for hemispherical counters with (a) uniform 2.13 mm thick walls; and (b) 2.13 mm thick hemisphere with a 5 mm thick cylindrical base

TEPC Type	(a) 2.54 cm Hemisphere with 2.13 mm thick walls		(b) 2.54 cm Hemisphere 5 mm thick base	
	Above	Side	Above	Side
$\bar{y}_F$ [keV/ $\mu$ m]	19.49 $\pm$ 0.08	23.96 $\pm$ 0.09	19.33 $\pm$ 0.08	23.65 $\pm$ 0.09
$\bar{y}_D$ [keV/ $\mu$ m]	62.96 $\pm$ 0.96	74.74 $\pm$ 1.02	63.98 $\pm$ 1.04	75.25 $\pm$ 1.10
$\bar{Q}$	11.34 $\pm$ 0.07	13.65 $\pm$ 0.08	11.37 $\pm$ 0.07	13.66 $\pm$ 0.08
Q Response ( $\bar{Q}/Q^*(10)$ )	1.18 $\pm$ 0.008	1.42 $\pm$ 0.008	1.18 $\pm$ 0.008	1.42 $\pm$ 0.009
Dose per unit fluence [Gy*cm <sup>2</sup> /n]	7.91 x 10 <sup>-12</sup> $\pm$ 9 x 10 <sup>-15</sup>	7.52 x 10 <sup>-12</sup> $\pm$ 7 x 10 <sup>-15</sup>	7.98 x 10 <sup>-12</sup> $\pm$ 8.94 x 10 <sup>-15</sup>	7.71 x 10 <sup>-12</sup> $\pm$ 8.34 x 10 <sup>-15</sup>
Dose Response	0.71 $\pm$ 8 x 10 <sup>-4</sup>	0.67 $\pm$ 7 x 10 <sup>-4</sup>	0.71 $\pm$ 8 x 10 <sup>-4</sup>	0.69 $\pm$ 7 x 10 <sup>-4</sup>
Dose equivalent per unit fluence [Sv*cm <sup>2</sup> /n]	8.97 x 10 <sup>-11</sup> $\pm$ 6 x 10 <sup>-13</sup>	1.03 x 10 <sup>-10</sup> $\pm$ 6 x 10 <sup>-13</sup>	9.07 x 10 <sup>-11</sup> $\pm$ 6 x 10 <sup>-13</sup>	1.05 x 10 <sup>-10</sup> $\pm$ 6.44 x 10 <sup>-13</sup>
H*(10) Response	0.83 $\pm$ 0.005	0.95 $\pm$ 0.005	0.84 $\pm$ 0.005	0.98 $\pm$ 0.006
Sensitivity [counts/ $\mu$ Sv]	10.72 $\pm$ 0.88	7.25 $\pm$ 0.56	10.79 $\pm$ 0.89	7.34 $\pm$ 0.59

Table A.2 – Results of Monte Carlo simulations in PHITS using <sup>252</sup>Cf-D<sub>2</sub>O moderated neutron fields for hemispherical counters with (a) uniform 2.13 mm thick walls; and (b) 2.13 mm thick hemisphere with a 5 mm thick cylindrical base

## References

- [1] D.J. Thomas, 'The system of radiation protection for neutrons: does it fit the purpose?', *Radiat. Prot. Dosim.*, vol. 161, no. 1-4, pp. 3-10, 2014.
- [2] European Commission Directorate-General for Energy and Transport Directorate H— Nuclear Energy Unit H.4, 'Technical Recommendations for Monitoring Individuals Occupationally Exposed to External Radiation', 2009. Available: <http://ec.europa.eu/energy/nuclear/radiationprotection/doc/publication/160.pdf>
- [3] A.J. Waker, K. Szornel and J.C. Nunes, 'TEPC Performance in the CANDU Workplace', *Radiat. Prot. Dosim.*, vol. 70, no. 1-4, pp. 197-202, 1997.
- [4] J.C. Nunes, A.J. Waker and M. Lieskovsky, 'Neutron Fields Inside Containment of a Candu® 600-PHWR Power Plant', *Health Phys.*, vol. 71, no. 2, pp. 235-247, 1996.
- [5] International Commission on Radiological Protection, 'ICRP Publication 60', Pergamon Press, Oxford, United Kingdom, 1991.
- [6] Government of Canada Justice Laws Website, 'Radiation Protection Regulations', 2015. [Online]. Available: <http://laws-lois.justice.gc.ca/eng/regulations/SOR-2000-203/page-4.html>. [Accessed: 1- Oct-2015].
- [7] International Commission on Radiation Units and Measurements, Rep. 39, 'Determination of Dose Equivalents Resulting from External Radiation Sources', ICRU, Bethesda, MD, 1985.
- [8] International Commission on Radiation Units and Measurements, Rep. 43, 'Determination of Dose Equivalents from External Radiation Sources. Part 2', ICRU, Bethesda, MD, 1988.
- [9] International Commission on Radiation Units and Measurements, Rep. 51, 'Quantities and Units in Radiation Protection Dosimetry', ICRU, Bethesda, MD, 1993.
- [10] International Commission on Radiological Protection, 'ICRP Publication 74', Pergamon Press, Oxford, United Kingdom, 1996.
- [11] D.A. Gollnick, *Basic Radiation Protection Technology by Daniel Gollnick 6th ed.*, 6th ed. Altadena, CA: Pacific Radiation Corporation, 2013.
- [12] T.W. Crane and M.P. Baker, 'Neutron Detection', in *Passive Nondestructive Assay of Nuclear Materials*, 1st ed., D. Reilly, N. Ensslin and H. Smith, Ed. Springfield, VA: National Technical Information Service, 1991, pp. 379-406.
- [13] D.T. Bartlett, J.-L Chartier, M. Matzke, A. Rimpler and D.J. Thomas, 'Concepts and quantities in spectrometry and radiation protection', *Radiat. Prot. Dosim.*, vol. 107, no. 1-3, pp. 23-35, 2003.
- [14] H. Schuhmacher, R. Hollnagel and B.R.L. Siebert, 'Sensitivity study of parameters influencing calculations of fluence-to-ambient dose equivalent conversion coefficients for neutrons', *Radiat. Prot. Dosim.*, vol. 54, no. 3-4, pp. 221-225, 1994.

- [15] US NRC, 'Units of radiation dose', 2015. [Online]. Available: <http://www.nrc.gov/reading-rm/doc-collections/cfr/part020/part020-1004.html>. [Accessed: 9- Oct- 2015].
- [16] International Organization for Standardization. 2000. Reference neutron radiations – Part 1: Characteristics and methods of production. ISO 8529-1:2000(E). ISO, Geneva, Switzerland.
- [17] D.J. Thomas, R. Nolte and V. Gressier, 'What is neutron metrology and why is it needed?', *Metrologia*, vol. 48, no. 6, pp. S225-S238, 2011.
- [18] H.H. Rossi, 'Multi-element dosimeters for radiation protection measurements', *Health Phys.*, vol. 44, no. 4, pp. 403-405, 1983.
- [19] H.H. Rossi and M. Zaider, *Microdosimetry and Its Applications*. Berlin: Springer, 1996.
- [20] A.J. Waker, 'Principals of Experimental Microdosimetry', *Radiat. Prot. Dosim.*, vol. 61, no. 4, pp. 297-308, 1995.
- [21] A.M. Kellerer and H.H. Rossi, 'The theory of dual radiation action', *Curr. Top. Radiat. Res.*, vol. 104, no. 8, pp. 75-158, 1972.
- [22] P. Ségur, P. Olko and P. Colautti, 'Numerical Modelling of Tissue-Equivalent Proportional Counters', *Radiat. Prot. Dosim.*, vol. 61, no. 4, pp. 323-350, 1995.
- [23] D.H. Nutton and S.J. Harris, 'Tissue equivalence in neutron dosimetry', *Phys. in Med. and Bio.*, vol. 25, no. 6, pp. 1173-1180, 1980.
- [24] A.M. Kellerer, 'An Assessment of Wall Effects on Microdosimetric Measurements', *Radiat. Res.*, vol. 47, no. 2, pp. 377-386, 1971.
- [25] U. Fano, 'Note on the Bragg-Gray Cavity Principle for Measuring Energy Dissipation', *Radiat. Res.*, vol. 1, no. 3, pp. 237-240, 1954.
- [26] U. Fano, 'Penetration of Protons, Alpha Particles, and Mesons', *Annu. Review of Nucl. Science*, vol. 13, no. 1, pp. 1-66, 1963.
- [27] International Commission on Radiation Units and Measurements, Rep. 10b, 'National Bureau of Standards Handbook 85: Physical Aspects of Irradiation', ICRU, Bethesda, MD, 1962.
- [28] A.J. Waker, 'Gas Gain Characteristics of Some Walled Proportional Counters in Microdosimetry', *Proc. of the Eighth Symp. of Microdosimetry*, pp. 1017-1030, 1982.
- [29] International Commission on Radiation Units and Measurements, Rep. 26, 'Neutron Dosimetry in Biology and Medicine', ICRU, Bethesda, MD, 1997.
- [30] J.A. Auxier and M.D. Brown, 'Neutron Cross-Sections and Reaction Products for H, C, N, and O for the Energy Range from Thermal to 15 MeV', in *Proc. of the First Int. Congr. of Toxic Agents Protection*, 1966, pp. 853-858.

- [31] F.H. Attix, *Introduction to radiological physics and radiation dosimetry*. New York: Wiley, 1986.
- [32] R. Caswell, 'Deposition of Energy by Neutrons in Spherical Cavities', *Radiat. Res.*, vol. 27, no. 1, pp. 92-107, 1966.
- [33] World Health Organization, 'What is Ionizing Radiation?', 2015. [Online]. Available: [http://www.who.int/ionizing\\_radiation/about/what\\_is\\_ir/en/](http://www.who.int/ionizing_radiation/about/what_is_ir/en/). [Accessed: 6- Oct- 2015].
- [34] J. Turner, 'Interaction of ionizing radiation with matter', *Health Phys.*, vol. 88, no. 6, pp. 520-544, 2005.
- [35] H. Bethe, 'Zur Theorie des Durchgangs schneller Korpuskularstrahlen durch Materie', *Ann. der Phys.*, vol. 397, no. 3, pp. 325-400, 1930.
- [36] H. Bethe and A. Smekal, *Handbuch der Physik*. Berlin: Springer, 1933.
- [37] J.F. Ziegler, *Stopping and Range of Ions in Matter (SRIM)*. 2008. Available: <http://www.srim.org/>
- [38] W. Barkas and D. Evans, *Nuclear research emulsions*. New York: Academic Press, 1963.
- [39] International Commission on Radiation Units and Measurements, Rep. 37, 'Stopping powers for electrons and positrons', ICRU, Bethesda, MD, 1984.
- [40] P. Wooton, *Protocol for neutron beam dosimetry*. New York, N.Y.: Published for the American Association of Physicists in Medicine by the American Institute of Physics, 1980.
- [41] G. Knoll, *Radiation detection and measurement*. New York: Wiley, 1979.
- [42] A. Cauchy, *Memoire sur la rectification des courbes et la quadrature des surface courbe. Oeuvres Completes Vol. 2*. Paris: Gauthier-Villard, 1908.
- [43] R. Pynn, 'Los Alamos Neutron Science Center: A Primer on Neutron Scattering', <https://www.ncnr.nist.gov/summerschool/ss15/pdf/NeutronScatteringPrimer.pdf>, 2015.
- [44] International Commission on Radiation Units and Measurements, Rep. 36, 'Microdosimetry', ICRU, Bethesda, MD, 1983.
- [45] S. Al-Bayati, 'The Application of Experimental Microdosimetry to Mixed-Field Neutron-Gamma Dosimetry', MAsc., University of Ontario Institute of Technology, 2012.
- [46] P. Kliauga, A.J. Waker and J. Barthe, 'Design of Tissue-Equivalent Proportional Counters', *Radiat. Prot. Dosim.*, vol. 61, no. 4, pp. 309-322, 1995.
- [47] H.H. Rossi and W. Rosenzweig, 'A Device for the Measurement of Dose as a Function of Specific Ionization 1', *Radiology*, vol. 64, no. 3, pp. 404-411, 1955.
- [48] P.J. Champion, 'The operation of proportional counters at low pressures for microdosimetry', *Phys. in Medicine and Biology*, vol. 16, no. 4, pp. 611-616, 1971.

- [49] P.W. Benjamin, C.D. Kemshall and J. Redfearn, 'A high resolution spherical proportional counter', *Nucl. Instrum. and Methods*, vol. 59, no. 1, pp. 77-85, 1968.
- [50] Far West Technology, Inc., 'Operation Manual: Model LET-SW5', Goleta, CA, 2001. Available: [www.fwt.com/detector/support/LETSW5\\_manual.PDF](http://www.fwt.com/detector/support/LETSW5_manual.PDF)
- [51] F. Ali, 'Design and Characterization of Next-Generation Tissue Equivalent Proportional Counters for use in Low Energy Neutron Fields', Ph.D, University of Ontario Institute of Technology, 2014.
- [52] L.A. Braby, G.W. Johnson and J. Barthe, 'Practical considerations in the design & construction of TEPCs', *Radiat. Prot. Dosim.*, vol. 61, no. 4, pp. 351-379, 1995.
- [53] A.J. Waker, Aslam and J. Lori, 'Design of a multi-element TEPC for neutron monitoring', *Radiat. Prot. Dosim.*, vol. 143, no. 2-4, pp. 463-466, 2010.
- [54] Aslam and A.J. Waker, 'Performance of a high sensitivity multi-element Tissue Equivalent Proportional Counter for Radiation Protection Neutron Monitoring Measurements', *Health Phys.*, vol. 98, no. 5, pp. 692-703, 2010.
- [55] P. Kliauga, H.H. Rossi and G. Johnson, 'A Multi-element Proportional Counter for Radiation Protection Measurements', *Health Phys.*, vol. 57, no. 4, pp. 631-636, 1989.
- [56] A.M. Kellerer, in *The Dosimetry of Ionizing Radiation*, 1st ed., K. Kase, Ed. Orlando FL: Academic Press, 1985, pp. 78-163.
- [57] P.D. Bradley, 'Development of silicon microdosimeter', Ph.D, University of Wollongong, 2000.
- [58] J.B. Langworthy, 'A General Approach to Chord Length Distributions Applied to a Hemisphere', *Radiat. Res.*, vol. 118, no. 1, pp. 21-36, 1989.
- [59] U. Mäder, 'Chord Length Distributions for Circular Cylinders', *Radiat. Res.*, vol. 82, no. 3, pp. 454-466, 1980.
- [60] A.M. Kellerer, 'Chord-Length Distributions and Related Quantities for Spheroids', *Radiat. Res.*, vol. 98, no. 3, pp. 425-437, 1984.
- [61] A.M. Kellerer, 'Considerations on the Random Traversal of Convex Bodies and Solutions for General Cylinders', *Radiat. Res.*, vol. 47, no. 2, pp. 359-376, 1971.
- [62] A.M. Kellerer, 'Criteria for the Equivalence of Spherical and Cylindrical Proportional Counters in Microdosimetry', *Radiat. Res.*, vol. 86, no. 2, pp. 277-286, 1981.
- [63] 'Lecture 1: Introduction to ANSYS Maxwell (ANSYS Maxwell Training Manual)', [http://ansoft-maxwell.narod.ru/en/Maxwell\\_v16\\_L01\\_Introduction.pdf](http://ansoft-maxwell.narod.ru/en/Maxwell_v16_L01_Introduction.pdf), 2013.

- [64] 'Lecture 4: Static Electric Solvers (ANSYS Maxwell Training Manual)', [http://ansoft-maxwell.narod.ru/en/Maxwell\\_v16\\_L04\\_Static\\_Electric\\_Solvers.pdf](http://ansoft-maxwell.narod.ru/en/Maxwell_v16_L04_Static_Electric_Solvers.pdf), 2013.
- [65] E.W. Weisstein, 'Erf', *MathWorld, Wolfram Web Resource*, 2015. [Online]. Available: <http://mathworld.wolfram.com/Erf.html>. [Accessed: 10- Oct- 2015].
- [66] L. De Nardo, V. Cesari, G. Donà, G. Magrin, P. Colautti, V. Conte and G. Tornielli, 'Mini-TEPCs for radiation therapy', *Radiat. Prot. Dosim.*, vol. 108, no. 4, pp. 345-352, 2004.
- [67] A. Taymaz, M.N Erduran, A. Tutay and Bereich, 'Monte-Carlo and deterministic analysis of microdosimetric parametric for fast neutrons', in *The second regional Mediterranean con. on radiat. protection*, Tel-Aviv, Israel, 1997, pp. 20-25. Available: [https://inis.iaea.org/search/search.aspx?orig\\_q=RN:29045611](https://inis.iaea.org/search/search.aspx?orig_q=RN:29045611)
- [68] B. Janský, Z. Turzík, E. Novák, J. Kyncl, F. Cvachovec and P. Tiller, 'Comparison of measured and calculated neutron transmission through heavy water for <sup>252</sup>Cf source placed in the center of 30 cm diameter sphere', *Ann. of Nucl. Energy*, vol. 24, no. 15, pp. 1189-1212, 1997.
- [69] F. Ali, A.J. Waker and E.J. Waller, 'Intercomparison of Monte Carlo radiation transport codes to model TEPC response in low-energy neutron and gamma-ray fields', *Radiat. Prot. Dosim.*, vol. 161, no. 1-4, pp. 257-260, 2014.
- [70] F.H. Attix, W.C. Roesch and E. Tochilin, *Radiation Dosimetry*. Academic Press, 1968.
- [71] M.J. Berger, J.S. Coursey, M.A. Zucker and J. Chang, 'Stopping-Power and Range Tables for Electrons, Protons, and Helium Ions', *Physics.nist.gov*, 2005. [Online]. Available: <http://www.nist.gov/pml/data/star/index.cfm>. [Accessed: 28- Oct- 2015].
- [72] W. Bambynek, 'On selected problems in the field of proportional counters', *Nucl. Instr. and Methods*, vol. 112, no. 1-2, pp. 103-110, 1973.